Acta Biomaterialia xxx (xxxx) xxx

Contents lists available at ScienceDirect

Acta Biomaterialia

journal homepage: www.elsevier.com/locate/actbio

Review article

Strategies to improve the photothermal capacity of gold-based nanomedicines

Ariana S.C. Gonçalves[a], Carolina F. Rodrigues[a], André F. Moreira[a,*], Ilídio J. Correia[a,b,*]

[a] CICS-UBI – Health Sciences Research Centre, Universidade da Beira Interior, Av. Infante D. Henrique, 6200-506 Covilhã, Portugal
[b] CIEPQF — Departamento de Engenharia Química, Universidade de Coimbra, Rua Sílvio Lima, 3030-790 Coimbra, Portugal

ARTICLE INFO

Article history:
Received 17 July 2020
Revised 27 August 2020
Accepted 2 September 2020
Available online xxx

Keywords:
Gold nanoparticles
Photothermal therapy
Cancer
NIR radiation

ABSTRACT

The plasmonic photothermal properties of gold nanoparticles have been widely explored in the biomedical field to mediate a photothermal effect in response to the irradiation with an external light source. Particularly, in cancer therapy, the physicochemical properties of gold-based nanomaterials allow them to efficiently accumulate in the tumor tissue and then mediate the light-triggered thermal destruction of cancer cells with high spatial-temporal control. Nevertheless, the gold nanomaterials can be produced with different shapes, sizes, and organizations such as nanospheres, nanorods, nanocages, nanoshells, and nanoclusters. These gold nanostructures will present different plasmonic photothermal properties that can impact cancer thermal ablation. This review analyses the application of gold-based nanomaterials in cancer photothermal therapy, emphasizing the main parameters that affect its light-to-heat conversion efficiency and consequently the photothermal potential. The different shapes/organizations (clusters, shells, rods, stars, cages) of gold nanomaterials and the parameters that can be fine-tuned to improve the photothermal capacity are presented. Moreover, the gold nanostructures combination with other materials (*e.g.* silica, graphene, and iron oxide) or small molecules (*e.g.* indocyanine green and IR780) to improve the nanomaterials photothermal capacity is also overviewed.

1. Introduction

Nanoparticle-mediated photothermal therapy (PTT) has been widely explored as a standalone or combinatorial therapy for cancer because it enables to focus of the hyperthermia in the tumor avoiding damages to the healthy tissues [1]. This therapy takes advantage of the nanomaterials' physicochemical properties, which confer to them tumor selectivity [2]. At the tumor site, the nanomaterials will be irradiated with a light source promoting the generation of heat [3]. This tumor localized increments of temperature can sensitize the cells to other therapeutic applications (*e.g.* chemotherapy) or even induce several cellular damages that can ultimately lead to apoptosis or necrosis when reaching temperatures superior to 40°C [4,5]. In this approach, the application of NIR radiation (700-1200 nm) to activate the nanomaterials is crucial since the major components of the human body (*e.g.* water, proteins, collagen, hemoglobin) present an insignificant absorption in this region of the electromagnetic spectrum [6]. Moreover, this optical transparency minimizes the absorption and scattering phenomena, which improve radiation penetration and photothermal efficacy [7].

Several types of nanomaterials can be applied as photothermal agents, such as carbon nanotubes [8], graphene oxide [9], polyaniline [10], and gold [11], or even conjugated with small molecules (*e.g.* IR780 [12], indocyanine green (ICG) [13]) to mediate PTT. Among them, gold-based nanoparticles possess unique physicochemical properties making them one of the most explored nanoplatforms in PTT [14]. Gold is known as one of the least reactive metals, presents a high variability in terms of shape, size and surface chemistry, and high resistance to degradation and oxidation [15]. Moreover, the localized surface plasmon resonance (LSPR) phenomenon observed in gold nanoparticles can be fine-tuned by optimizing the size and shape to render them a strong absorption in the NIR region increasing their efficiency as PTT agents [16–18]. Additionally, the gold nanomaterials can also act as contrast agents in computerized tomography (CT) and magnetic resonance imaging (MRI), mass attenuation of gold is superior to that of the iodinated contrast agents commonly used in the clinic, or even prompt the photoacoustic imaging (PAI) [19–21]. Otherwise, the gold nanoparticles affinity to interact with compounds containing thiol or disulfide groups can be explored for modifying the surface of the nanoparticles with passivating agents that

* Corresponding authors.
E-mail addresses: afmoreira@fcsaude.ubi.pt (A.F. Moreira), icorreia@ubi.pt (I.J. Correia).

https://doi.org/10.1016/j.actbio.2020.09.008
1742-7061/

enhance the biocompatibility and blood circulation time, targeting moieties that improve the selectivity towards the tumor tissue, or even with therapeutic molecules [22,23]. Despite the promising properties of gold nanoparticles, some limitations have been impairing their utilization in biological systems. During blood circulation, the gold-thiol interactions also facilitate the establishment of non-specific interactions with different biomolecules, such as proteins. This event can induce surface charge alterations, particle aggregation, and size increase in the nanoparticles and thus affect their interaction with the human body (*e.g.* nanoparticles uptake, blood circulation time and biocompatibility) [24,25]. Otherwise, a recent analysis revealed that in general, only 0.7% of the administered nanoparticles reach the tumor site, which greatly impacts its therapeutic performance due to the sub-optimal concentrations of therapeutics [26]. Further, the gold nanoparticles exposition to high-energy laser pulses during bioimaging or therapeutic applications can induce the nanoparticle reshaping or degradation and consequently decrease its therapeutic efficiency [27]. To overcome these limitations, researchers have been exploring different approaches for increasing the photothermal conversion efficiency of gold nanoparticles.

In this review, the gold-based nanomaterials application in cancer PTT is discussed, particularly the main strategies explored to improve the photothermal capacity of these nanostructures. Initially, the different shapes/organizations (clusters, shells, rods, stars, cages) of gold nanomaterials and the parameters affecting their photothermal capacity are analyzed. Subsequently, the combination of gold with other materials (*e.g.* silica, graphene, and iron oxide) or small molecules (*e.g.* IR780, ICG) to improve the nanomaterial photothermal capacity is also overviewed.

2. Nanomaterials application in photothermal therapy

The PTT mediated by nanomaterials is highly dependent on several parameters such as the capacity of the nanomaterials to generate heat and its selectivity towards the tumor tissue as well as the laser irradiation parameters. Considering the systemic administration, the nanomaterials must be able to accumulate in the tumor tissue by passive accumulation (enhanced permeability and retention effect or vascular burst events) and/or active targeting (receptor-ligand or antigen-antibody interactions) [28,29]. Therefore, the nanomaterials bioavailability in tumors is closely linked to several physicochemical parameters such as the nanoparticle size, surface charge, corona, and surface moieties, as reviewed in detail by [30–32]. Then, the nanomaterials PTT is triggered by irradiating the tumor zone with a light source, usually a NIR laser. Several laser light parameters affect the heat generation by the nanomaterials, such as wavelength, power density, number of irradiations, laser distance, and duration [33–36]. The biological transparency windows located in the NIR region of spectra (*i.e.* NIR-I; 700–900 nm and NIR-II; 1000–1700 nm) decrease the off-target interaction of the radiation and endow a deeper penetration in the body [37]. Further, the laser wavelength should also match the absorption peak of the nanomaterial to maximize the heat generation (Fig. 1) [38]. Otherwise, the power density (total energy per second delivered into a specific area) of NIR irradiation will influence the penetration depth and the heat generated by the nanomaterials [39]. The utilization of higher power densities is associated with an increased nanoparticle excitation and heat generation [40]. Nevertheless, excessive power densities can also induce side-effects (*e.g.* skin burns) due to off-target interaction [41]. Furthermore, the photothermal effect can also be enhanced by optimizing the duration of the laser irradiation and the application of multiple irradiation sessions [42,43]. Upon the irradiation of the tumor site, the radiation-to-heat conversion efficiency of nanoparticles will be determinant for achieving an effective PTT. In gold-based nanomaterials, the radiation-to-heat conversion efficiency is dependent on the LSPR phenomenon (defined by the nanoparticle size and shape) and can be enhanced through the combination of gold with other materials (*e.g.* silica, iron oxide, and graphene) or small molecules (*e.g.* IR780 and ICG) (reviewed in Section 3.3).

3. Gold nanomaterials

Gold nanoparticles have been widely explored for cancer therapy applications, such as drug delivery and PTT [44]. Particularly, in PTT different design criteria affect the gold nanomaterials performance, such as the LSPR phenomenon, the radiation-to-heat conversion efficiency, and the surface functionalization. The LSPR phenomenon is defined by the light-induced resonant oscillation of the free electrons on the particle's surface, which can result in the light scattering or absorption [45]. Upon light absorption, the free electrons progress to an excited state and can release the absorbed energy in the form of heat during relaxation [46]. In gold nanomaterials, the LSPR wavelength can be adjusted to the NIR region by fine-tuning the particle size and organization (Table 1) [47]. Additionally, the shape also plays an important role in the LSPR phenomenon of gold nanomaterials. In this regard, the sphere, rod, star, and cage-like shapes are the most explored ones for the biological application of gold nanomaterials, namely in cancer PTT. Nevertheless, it is worth to notice that there are less explored shapes such as nanovesicles [48–50], bellflowers [51–53], nanobipyramids [54], and nanoprisms [55–60] that can also be explored to mediate a photothermal effect in response to irradiation with a NIR laser. The optimization of gold nanostructures to match the LSPR wavelength with the NIR laser irradiation results in increased energy absorption and consequently an enhanced heat generation (Fig. 1).

3.1. Optimization of the gold nanomaterials' size and shape

3.1.1. Nanostructures based on gold nanospheres

The gold nanoparticles are usually produced by promoting the nucleation of gold atoms upon the reduction of a gold source in the presence of stabilizing agents [61]. The gold spheres are originated when this reaction occurs under thermodynamically controlled conditions [62]. Nevertheless, the optimization of the gold nanospheres size only leads to slight changes in the LSPR absorption band, in the 500 to 600 nm region [63]. Alternatively, the organization of gold nanospheres as clusters or shells has demonstrated the ability to imprint in the nanosystem a PTT capacity [64,65]. This change in the physical properties of the gold nanostructures is attributed to the interactions of the near-field of one particle with the adjacent ones in close proximity promoting the coupling of the plasmon oscillations [66]. This phenomenon is more pronounced when the interparticle gaps are decreased, using smaller nanospheres or reduce the space between them [67].

3.1.1.1. Gold nanoclusters. The gold nanoclusters are formed by promoting the aggregation/coupling of gold nanospheres. Different strategies have been explored to mediate this process, such as the use of polymeric spacer-arms linking different particles, dendrimers/polymeric matrices encapsulating the gold nanospheres, large templates based on proteins, polymers or DNA, and the utilization of organic solvents or small molecules to promote the aggregation of gold nanospheres [68–70]. Chegel *et al* demonstrated that the organic compounds containing amine and thiol groups such as cysteamine, ethanolamine, and thiourea can promote the aggregation of citrate coated gold nanoparticles originating nanoclusters [71]. The produced single gold nanospheres presented a diameter of 10-15 nm and a single absorption peak at ≈520

Please cite this article as: A.S.C. Gonçalves, C.F. Rodrigues and A.F. Moreira et al., Strategies to improve the photothermal capacity of gold-based nanomedicines, Acta Biomaterialia, https://doi.org/10.1016/j.actbio.2020.09.008

Table 1
Overview of the shape and organization-dependent application of gold nanoparticles in photothermal therapy (N.D. – non disclosed, N.A. – not applicable).

Shape	Size of gold nanostructure	Surface Modification	LSPR peak	Loading	Photothermal Effect		Type of Study	Test Model	Main Results	Ref.
					Laser Parameters	Temperature				
NCL	88 nm clusters comprised of 4.5 nm GNSP	Bovine Serum Albumin	Broad absorbance from 600 to 900 nm	N.A.	808 nm, 1.5 W. cm^{-2}, 10 min	≈70°C	*In vitro/In vivo*	HCT 116 cells/HCT 116 tumor-bearing mice	Reduction of the HCT 116 tumors' volume from 150 to 17.8 mm^3.	[72]
	100 nm clusters comprised of 6 nm GNSP	PLGA, L-α-Phosphatidyl-DL-Glycerol, and 1,2-Distearoyl-sn-Glycero-3-Phosphoethanolamine-N-Carboxy (PEI)-2000	600 nm	N.A.	800 nm, fluence: 20 $J.cm^{-2}$, pulse width: 400 ms, pulse frequency: 1 Hz, 1 min	≈60°C	*In vitro*	SUM-159 and U87MG tumor spheroids	Ablation of SUM-159 cancer cells. Almost complete elimination of tumor cells in U87MG tumor spheroids.	[73]
	53 nm clusters comprised of 4 nm GNSP	CRQAGFSL-5-ALA, CRQAGFSL-Cy5.5, and PEG-U11	544 nm	5-ALA	750 nm, 2 $W.cm^{-2}$, 5 min	≈51°C	*In vitro/In vivo*	PANC1 cells/PANC1 tumor-bearing mice	Inhibition of tumor growth by PTT. The combination of PTT and 5-ALA reduced the tumor volume for 15 days.	[74]
	24 nm clusters comprised of 4.6 nm GNSP	Sodium alginate	660 nm	N.A.	660 nm, 2 $W.cm^{-2}$, 8 min	≈50°C	*In vitro/In vivo*	KB and 293T cells/KB tumor-bearing mice	Elevation of the tumor temperature above 50°C leading to the thermal ablation of KB tumors.	[147]
	150 nm clusters	Hyaluronan-polycaprolactone co-polymer	780 nm	Verteporfin	808 nm, 1.5 $W.cm^{-2}$, 10 min	≈74.1°C	*In vitro/In vivo*	MDA-MB-231 cells/MDA-MB-231 tumor bearing mice	The PTT therapy induced the increase of the tumor temperature to 60°C suppressing its growth for 21 days. The combination of PTT and Verteporfin induced the complete elimination of MDA-MB-231 tumors.	[148]
	139.3 nm NPs comprised of 2 nm GNSP	poly(2-methoxy-5-(2-ethylhexyloxy)-1,4-phenylenevinylene) (MEH-PPV) and PEI	660 nm	N.A.	660 nm, 1.6 $W.cm^{-2}$, 15 min	ΔT=10°C	*In vitro*	A549 cells	The PTT mediated by the NCL induced the death of 87.4±1.0% of cancer cells at 20 μg/mL and 100±0.2% at 30 μg/mL.	[149]
NSH	150 nm NPs comprised of a 50 nm gold core, a 30 nm organosilica layer, and a 20 nm GNSH	N.A.	590 and 780 nm	N.A.	808 nm, 2 $W.cm^{-2}$, 15 min	≈55°C	*In vitro/In vivo*	MDA-MB-231 cells/MDA-MB-231 tumor-bearing mice	The PTT mediated by the NSH induced the death of 90% of the MDA-MB-231 cells and promoted the temperature increase of the MDA-MB-231 tumors to ≈58°C.	[76]
	10 nm GNSH coated 60 nm silica cores	Anti-HER2 modified PEG	815 nm	N.A.	820 nm, ≈35 $W.cm^{-2}$, 7 min	N.D.	*In vitro*	SKBR3 cells	The PTT mediated by the NSH induced irreversible damages in the cells' membrane leading to the thermal ablation of SKBR3 cancer cells.	[75]
	Hollow GNSH with 50 nm in diameter	PEG	740 nm	HSP70 siRNA	765 nm, 4 $W.cm^{-2}$, 10 min	≈48°C	*In vitro/In vivo*	U87MG cells/U87MG tumor-bearing mice	The PTT therapy induced the increase of the tumor temperature to 46°C, which combined with the siRNA delivery decreased the U87MG tumors' growth.	[150]
	14 nm GNSH coated 120 nm chitosan modified soya phosphatidyl choline (SPC)/cholesterol liposomes	N.A.	Broad absorbance from 550 to 800 nm	Resveratrol	808 nm, 2 $W.cm^{-2}$, 10 min	≈66°C	*In vitro*	HeLa cells	The PTT mediated by the GNSH induced the decrease in the cell viability to 57.3%, which was enhanced by the simultaneous delivery of resveratrol reducing the cell viability to 20%.	[151]
	5 nm GNSH coated 121 nm poly[2-(N, N-dimethylamino)- ethyl methacrylate]–poly(ε-caprolactone) micelles	PEG	Broad absorbance from 500 to 800 nm	SN-38	808 nm, 2 $W.cm^{-2}$, 10 min	≈53°C	*In vitro/In vivo*	HCT116 cells/HCT116 tumor bearing mice	The PTT mediated by the GNSH induced the increase of the tumor temperature to 53°C, which combined with the SN-38 action decreased the growth of HCT116 tumors.	[152]
	GNSH coated 100 nm PEI-b-poly(2-diisopropylamino/2-mercaptoethylamine) ethyl aspartate vesicles	N.A.	800 nm	DOX	808 nm, 1.5 $W.cm^{-2}$, 10 min	ΔT≈20°C	*In vitro/In vivo*	Bel-7402 cells/Bel-7402 tumor bearing mice	The PTT mediated by the GNSH slowed the tumor growth. The combinatorial chemo-PTT resulted in a decrease of the tumor volume until day 6, followed by a slow tumor growth until day 20.	[153]

(*continued on next page*)

Table 1 (*continued*)

Shape	Size of gold nanostructure	Surface Modification	LSPR peak	Loading	Photothermal Effect		Type of Study	Test Model	Main Results	Ref.
					Laser Parameters	Temperature				
NR	L: 28 nm W: 7.5 nm A.R: 3.7	PEG-modified with phosphorylcholine and sulfobetaine	510 and 785 nm	N.A.	808 nm, 1.56 $W.cm^{-2}$, 5 min	ΔT=30.7°C	*In vitro*/*In vivo*	HepG2 cells/KB tumor-bearing mice	The PTT mediated by GNR induced the complete ablation of KB tumors, without being observed tumor reoccurrence in the following 40 days.	[154]
	L: 30 nm, W: 10 nm, A.R: 3	Human serum albumin	542 and 780 nm	truncated Evans Blue	808 nm, 0.5 $W.cm^{-2}$, 10 min	≈55°C	*In vitro*/*In vivo*	SCC7 cells/SCC7 tumor-bearing mice	The PTT mediated by the GNSH induced a 25°C increase in the tumors' temperature, which combined with the truncated Evans Blue action promoted the complete elimination of SCC7 tumors.	[155]
	L: 38 nm, W: 11 nm, A.R: 3.45	N.A.	510 and 740 nm	N.A.	808 nm, 1.5 $W.cm^{-2}$, 2 min	ΔT≈35°C	*In vitro*	HSC-3	The PTT effect mediated by the different GNR significantly reduced the HSC-3 cell viability, reaching a minimum of 17% for the GNR with L: 28 nm.	[83]
	L: 28 nm, W: 8 nm, A.R: 3.5	N.A.	510 and 770 nm	N.A.		ΔT≈52°C				
	L: 17 nm, W: 5 nm, A.R: 3.4	N.A.	510 and 755 nm	N.A.		ΔT≈55°C				
	L: 55 nm, W: 11 nm, A.R: 5	Anti-HER2 antibody-modified HA -containing hydrazide and thiol groups	512 and 800 nm	5-ALA	808 nm, 2 $W.cm^{-2}$, 10 min	≈55°C	*In vitro*/*In vivo*	MCF-7 cells and MCF-7 tumor-bearing mice	The PTT mediated by the GNR induced the increase of the tumor temperature to 46°C slowing the tumor growth. The combination of the NR PTT and 5-ALA action resulted in the complete elimination of the MCF-7 tumors without recurrence until day 20.	[86]
	L: 28 nm, W: 7.5 nm, A.R: 3.7	Polysarcosine	510 and 808 nm	N.A.	808 nm, 1.6 $W.cm^{-2}$, 3 min	≈90°C	*In vitro*/*In vivo*	A549 cells/A549 tumor-bearing mice	The PTT mediated by the GNR promoted the increase of the tumor temperature to 63.6°C inducing the complete ablation of A549 tumors without recurrence until day 10.	[156]
	L: 8 nm, W: 2 nm, A.R: 4	PEG and PLGA	60 nm vesicles: 560 and 830 nm	N.A.	808 nm, 0.8 $W.cm^{-2}$, 5 min	≈75°C	*In vitro*/*In vivo*	U87MG cells/U87MG tumor-bearing mice	The PTT mediated by the GNR promoted the increase of the tumor temperature to 60°C inducing the complete ablation of U87MG tumors without recurrence until day 16.	[157]
	L: ≈60 W: ≈17, A.R.: ≈3.5	Platinum	≈830 nm	N.A.	808 nm, 1 $W.cm^{-2}$, 5 min	≈65°C	*In vitro*	4T1 cells	The PTT mediated by the GNRs induced the decrease of the viability of 4T1 cells to ≈30%, which was enhanced by the introduction of Platinum reducing the cell viability to 5%.	[158]
	L: 42, W:10	Polyamidoamine dendrimer and RGD	824 nm	N.A.	808 nm, 24 $W.cm^{-2}$, 5 min	N.D.	*In vitro*/*In vivo*	A375 cells/ A375 tumor-bearing mice	The PTT mediated by the GNRs induced the blockage of the blood flow in the tumor tissue 3 hours after NIR laser irradiation and reduced the tumor growth for 28 days	[159]

(*continued on next page*)

Table 1 (*continued*)

Shape	Size of gold nanostructure	Surface Modification	LSPR peak	Loading	Photothermal Effect		Type of Study	Test Model	Main Results	Ref.
					Laser Parameters	Temperature				
NC	50 nm	HA	796 nm	DOX	808 nm, 1 W.cm^{-2}, 10 min	≈42°C	*In vitro/In vivo*	MDA-MB-231 cells/MDA-MB-231 tumor-bearing mice	The PTT mediated by the GNC promoted the increase of the tumor temperature to ≈44°C reducing tumor growth. The combination with the DOX action resulted in the complete elimination of MDA-MB-231 tumors in 9 days.	[160]
	47.4 nm	Poly (acrylic acid) and p(NIPAM-co-AM)	810 nm	DOX and Erlotinib	808 nm, 0.5 W.cm^{-2}, 10 min	≈46°C	*In vitro/In vivo*	MCF-7 and A431 cells/MCF-7 and A431 tumor-bearing mice	The PTT mediated by the GNC promoted the increase of the tumor temperature to ≈46.7°C reducing tumor growth. The combination with the DOX and Erlotinib action was able to suppress the growth of MCF-7 tumors for 9 days and promote the complete elimination of A431 tumors in 6 days.	[161]
	50.4 nm	PEG and HA	785 nm	N.A.	808 nm, 250 mW.cm^{-2}, 10 min	≈53°C	*In vitro/In vivo*	4T1 cells/4T1 tumor-bearing mice	The PTT mediated by the GNC promoted the increase of the tumor temperature to ≈43.5°C reducing tumor growth. The combination of PTT with X-ray treatment induced the regression of 4T1 tumors for 21 days.	[162]
	50 nm	FA modified PEG, lipoic acid, and PEI	790 nm	anti-miR-181b	808 nm, 1.25 W.cm^{-2}, 5 min	≈53°C	*In vitro/In vivo*	SMMC-7721 cells/SMMC-7721 tumor bearing mice	The PTT mediated by the GNC promoted the increase of the tumor temperature to ≈53.6°C reducing tumor growth. The combination with the anti-miR-181b action prevented the tumor growth for 15 days.	[163]
	40 nm	4T1 cell membrane vesicles	760 nm	DOX	808 nm, 2.5 W.cm^{-2}, 8 min	≈48°C	*In vitro/In vivo*	4t1 cells/4T1 tumor-bearing mice	The PTT mediated by the GNC promoted the increase of the tumor temperature to ≈57°C reducing tumor growth. The combination with the DOX action suppressed the tumor growth for 10 days.	[164]
	40 nm	Anti-EpCam modified erythrocytes membrane vesicles	750 nm	Paclitaxel	808 nm, 2.5 W.cm^{-2}, 5 min	≈49°C	*In vitro*	4T1 cells	The PTT effect mediated by the GNC significantly reduced the viability of the 4T1 cells to 40%, which reached 25% when combined with the Paclitaxel.	[165]
NS	27 nm in diameter with sharp branches	N.A.	550 and 700 nm	N.A.	808 nm, 1 W.cm^{-2}, 10 min	ΔT≈20°C	*In vitro/In vivo*	PC-3 cells/PC-3 tumor-bearing mice	The tumors' irradiation promoted an 8, 14, and 10°C increase in the tumors treated with the 27, 86, and 151 nm GNS.	[96]
	53 nm in diameter with sharp branches		790 nm			ΔT≈45°C				
	86 nm in diameter with sharp branches		800 nm			ΔT≈42°C				
	122 nm in diameter with sharp branches		900 nm			ΔT≈40°C				
	151 nm in diameter with sharp branches		950 nm			ΔT≈31°C				
	60 nm in diameter with sharp branches	PEG	730 nm	N.A.	808 nm, 2 W.cm^{-2}, 3 min	N.D.	*In vitro/In vivo*	MCF-7 cells/MCF-7 tumor bearing mice	The PTT mediated by the GNS promoted a 20°C increase of the tumor' temperature which mediated the decrease of the MCF-7 tumors' volume during 15 days.	[166]
	100 nm mean size tip-to-tip	FA–bovine serum albumin conjugate	763 nm	N.A.	808 nm, 1.6 W.cm^{-2}, 10 min	≈69°C	*In vitro*	HeLa cells	The photothermal effect mediated by the targeted GNS promoted the death of 71% of the HeLa cells.	[167]
	86 nm in diameter with sharp branches	PEG and TAT peptide	795 nm	N.A.	808 nm, 1.5 W.cm^{-2}, 10 min	ΔT≈40°C	*In vitro/In vivo*	B16-F10 cells/B16-F10 tumor-bearing mice	The PTT mediated by the GNS prevented the tumor growth for 7 days followed by a small increase in the tumor volume until day 14.	[168]

Abbreviations: NSH-Nanoshell; NCL-Nanocluster; NR-Nanorod; NC-Nanocage; NS-Nanostar; GNSH-Gold nanoshell; GNCL-Gold nanocluster; GNR-Gold nanorod; GNC-Gold nanocage; GNS-Gold Nanostar; NPs-nanoparticles and GNPs-Gold nanoparticles.

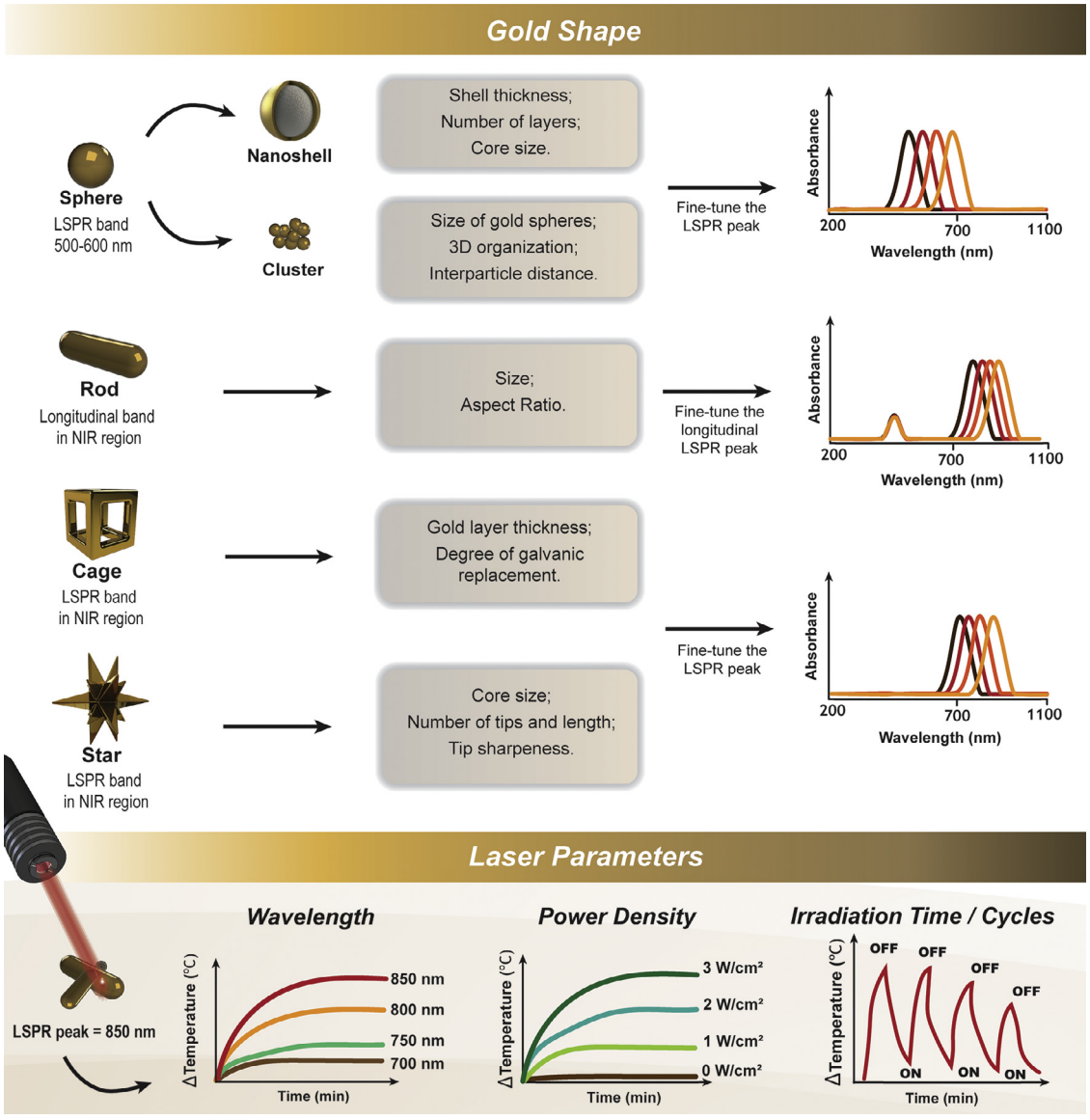

Fig. 1. Representation of the main factors that affect the gold nanoparticles PTT performance. The light-to-heat conversion efficiency and consequently the thermal ablation is directly affected by the shape and size of gold nanoparticles as well as the laser irradiation parameters, such as power laser wavelength, power density and irradiation time.

nm. The authors observed that the increase of the thiourea concentration from 1 μM to 5 μM induced a decrease in the absorption peak at 520 nm with a concurrent appearance of a second broad absorption peak in the 660-800 nm region. The authors also recorded a similar behavior when cysteamine (5 μM) was added to the gold nanospheres, however, the shift in the absorption peak occurred only in 623-640 nm. Otherwise, only ethanolamine concentrations in the millimolar ranges induced alterations in the gold nanospheres absorption spectra, with the appearance of low intensity and a very broad shoulder in the range of 550-800 nm. Park and colleagues explored albumin to produce gold nanoclusters for the photothermal treatment of colon cancer [72]. The gold nanoclusters were produced through a desolvation process, incubating gold nanospheres (≈5 nm of diameter) with albumin, followed by glutaraldehyde-mediated crosslinking. The resulting gold nanocluster-loaded albumin nanoparticles (size 105-182 nm) showed a greater absorbance over the 600–900 nm region, contrasting with the single absorption peak at 520 nm of the gold nanospheres. Additionally, the authors observed the gold nanocluster-loaded albumin nanoparticles (200 μg.mL^{-1}) irradiation (808 nm, 1.5 W.cm^{-2}, for 10 min) could induce a temperature increase up to ≈70°C. This photothermal capacity rendered to the nanosystem the capacity to increase the tumor tissue temperature to values superior to 50°C (808 nm, 1.5 W.cm^{-2}, for 5 min), 6h after the nanoparticles injection via tail vein of HCT116 tumor-bearing mice. Further, the authors also reported that gold nanocluster-loaded albumin nanoparticles mediated the suppression of the tumor growth and the decrease of the tumor volume to 17.8 mm^3 on day 20, contrasting with the ≈1850 mm^3 registered in the control group (treated with PBS), without eliciting any significant damages on major organs. Similarly, Iodice and coworkers used PLGA-based nanoparticle for promoting the clustering of gold nanospheres with 6 nm in diameter [73]. With that in mind, the gold nanospheres were resuspended in a chloroform solution containing PLGA and allowed to dry. Then, the resulting film was dissolved in acetonitrile and added to an ethanol solution containing L-α-Phosphatidyl-DL-Glycerol and 1,2-Distearoyl-sn-Glycero-3-Phosphoethanolamine-N-Carboxy(Polyethylene glycol

(PEI))-2000. These authors observed that the increase in the initial amount of gold nanospheres (25-150 μg) resulted in bigger nanoparticles (100-170 nm). Accordingly, the authors reported an overall enhancement of the nanoparticles absorbance along the spectra and higher initial concentrations of gold nanospheres resulted in a larger shift in the absorption peak of the nanoparticles, from 520 to 580 and 600 nm for the initial gold nanospheres amount of 100 and 150 μg, respectively. Moreover, upon irradiation with an 800 nm laser (fluence: 20 J.cm^{-2}, pulse width: 400 ms, pulse frequency: 1 Hz, during 1 min), the nanoparticles formed with 150 μg of gold nanospheres mediated an increase in the temperature of 20°C. Further, these authors also demonstrated that this photothermal capacity induced the death of breast cancer cells (SUM-159) as well as the almost complete ablation of tumor spheroids composed of glioblastoma multiforme cells (U87MG cells). Alternatively, Li *et al.* produced gold nanoclusters using 1,9-nonanedithiol to promote the crosslinking of gold spheres (10 nm in diameter) previously modified with Cys-Arg-Gln-Ala-Gly-Phe-Ser-Leu-5-ALA (CRQAGFSL-5-ALA) and Cys-Arg-Gln-Ala-Gly-Phe-Ser-Leu-Cy5.5 (CRQAGFSL-Cy5.5) [74]. Then, PEGylated U11 targeting peptides were immobilized on the surface of the gold nanoclusters (≈53 nm in diameter). The authors reported that the 1,9-nonanedithiol-mediated aggregation of gold nanospheres provoked an increase in the absorbance in the NIR region (*i.e.* 700-800 nm) and a red-shift in the absorption peak from the 532 to 544 nm. Further, the gold nanoclusters irradiation with a NIR laser (750 nm, 2 W.cm^{-2}, for 5 min) induced a 30°C increase in the medium temperature, reaching a maximum of 50°C. Such photothermal capacity inhibited the growth of orthotopic pancreatic tumors (intravenous administration of nanoclusters at a dose of 2 pmol per mouse). Further, the authors observed the almost complete tumor eradication after 15 days when the PTT effect was combined with the 5-ALA action (photodynamic agent).

3.1.1.2. Gold nanoshells. The gold nanoshells, likewise the nanocluster, can present absorption in the NIR region of the spectra when different gold nanospheres are immobilized in proximity. Loo and coworkers demonstrated that the gold nanoshells absorption spectra, in a predetermined inner core radius, is dependent on the shell thickness [75]. The authors produced gold nanoshells by grafting small gold seeds (1-3 nm) on the surface of amine-modified silica nanoparticles (60 nm in diameter). Then, the gold modified silica nanoparticles were incubated with a gold source ($HAuCl_4$) allowing the growth of the seeds and the formation of the gold nanoshell. The authors observed that the decrease in the gold nanoshell thickness from 20 to 10, 7, and 5 nm induced a red-shift in the absorption peak of the nanoparticles from ≈730 nm to ≈820, ≈910, and ≈1020 nm, respectively. Similarly, Gao and colleagues reported the development of multilayered gold nanoshells by promoting the growth of small gold seeds (2 nm) attached on the surface of gold-core organosilica shell nanospheres via gold-thiol interactions [76]. The multilayered gold nanoshells were composed of a spherical gold core with 50 nm in diameter, an organosilica layer with 30 nm, and an outer gold nanoshell with 20 nm. The authors reported that the formation of the gold nanoshells resulted in two absorption bands located in the 590 and 780 nm region, contrasting with the single absorption peak at 555 nm of the gold-core organosilica shell nanospheres. Moreover, the authors observed that the size increase of the spherical gold core from 30 to 50, and 70 nm in diameter induces a red-shift on both absorption peaks, respectively to 560 and 760 nm, 590 and 790 nm, and 615 and 815 nm. Further, the photothermal experiments revealed that upon NIR laser irradiation (808 nm, 2 W.cm^{-2}, for 15 min), the multilayered gold nanoshells mediated the temperature increase up to 55°C. The assays performed in MDA-MB-231 breast cancer cells demonstrated that the PTT capacity of this multilayered gold nanoshells could promote the death of 90% of the cells and the increase in the tumor tissue temperature to ≈58°C upon intravenous administration (100 µL, 4 mg.mL^{-1}) in MDA-MB-231 tumor-bearing mice and NIR laser irradiation for 5 min. In turn, Luo *et al* produced a gold nanoshell on the surface of chitosan-coated oleanolic acid liposomes for mediating chemo-photothermal antitumor therapy [77]. For that purpose, small gold seeds were produced via $NaBH_4$ reduction of gold salt and incubated with the previously formed chitosan-coated oleanolic acid liposomes. The attachment of the gold seeds occurred through the formation of Au-N bonds due to the amine groups available in the chitosan backbone. Then, the gold seeds modified liposomes were reacted with a growth solution containing $AuCl_3$ originating the gold nanoshell. The authors observed that the formation of the gold nanoshell rendered to the liposomes a broad absorption band between 600 and 850 nm, contrasting with the single absorption peak at 520 nm observed in the gold seeds modified liposomes. The authors explored this absorption capacity in the NIR region of the spectra to trigger the drug release, drug release of 92% and 69% at pH 5.5 and 7.4 after NIR laser irradiation (808 nm, 1 W.cm^{-2}, for 4 min) whereas in the absence of NIR laser these values decreased to 80% and ≈55%, respectively. Moreover, the combined action of the photothermal effect and faster drug release resulted in an increased antitumoral effect. The authors reported that the size of U14 tumors in the groups treated with the gold nanoshells presented a slower growth, with 79.65% and 50% inhibition rate for the irradiated (daily NIR laser irradiation 808 nm, 1 W.cm^{-2}, for 4 min) and non-irradiated groups, respectively. Rastinehad and colleagues reported the clinical results of the application of silica core gold nanoshells (AuroShells®, 15 nm thickness gold shell) in the PTT of prostate tumors [78]. The authors observed that the AuroShells administration at a dose of 7.5 mL.kg^{-1} (AuroShells concentration 4.8 mg.mL^{-1}) followed by the NIR laser irradiation (810 nm for 3 min) mediated the tumor ablation in 15 of 16 patients at 3 months, with 14 of 16 patients presenting the ablation zones negative for tumor after 12 months.

3.1.2. Gold nanorods

The rod-like shape of gold nanoparticles has been the standard for the application of the gold-based nanomaterials in photothermal therapy. This gold shape is usually produced using a seed-mediated growth methodology in the presence of a structure-directing agent [79]. In this process, small spherical gold spheres (*i.e.* seeds) are produced by using a strong reducing agent to promote the nucleation of gold atoms [80]. Subsequently, the gold seeds are added to a "growth solution", which is composed of gold salt (*e.g.* chloroauric acid), silver nitrate, and a stabilizing agent (*e.g.* cetyltrimethylammonium bromide- CTAB) inducing the rod-shaped growth [81]. The shape of gold nanorods renders to them two absorption bands in the electromagnetic field due to the specific LSPR phenomenon occurring in the two different dimensions of the nanorods (*i.e.* longitudinal and transversal axis) [82]. The LSPR phenomena of the nanorod's short axis correspond to the transverse plasmon resonance band, which leads to an absorption peak with lower intensity at 500-600 nm region. Otherwise, the longitudinal plasmon band that occurs along the major axis can be tuned to the NIR region of the spectra by optimizing the nanorods aspect ratio (*i.e.* rod length/width coefficient) [83]. Wang and colleagues demonstrated that increasing the gold nanorods aspect ratio mediated a red-shift in the longitudinal absorption peak [84]. The authors observed that the longitudinal absorption peaks occurred at 650, 760, 840, 920, 1000 nm for gold nanorods with an aspect ratio of 2.2, 3.5, 4.1, 5.1, and 6.3, respectively. Further, apart from the aspect ratio, the actual dimensions of gold nanorods also impact its absorption spectra and photothermal capacity [83]. The authors observed that by maintaining the aspect ratio (3.4-3.5) changes on the size of the nanorods (length and

width) 38 × 11, 28 × 8, and 17 × 5 nm provoked shifts on the longitudinal absorption peak 740, 770, and 755 nm, respectively. Further, the authors also registered alterations on the nanorods photothermal capacity upon irradiation with a NIR laser (808 nm, 5.8 W.cm^{-2}, for 2 min), when compared to the 38 × 11 and 17 × 5 nm nanorods, the photothermal-to-heat conversion efficiency of 28 × 8 nm gold nanorods was 2.05 and 1.40 times superior. Accordingly, the photothermal effect on HSC-3 cells was also superior in the 28 × 8 gold nanorods group, with a cell viability of 17% contrasting with the 100% and 29% recorded for the cells treated with 38 × 11 and 17 × 5 nm gold nanorods. Maestro *et al.* studied the light-to-heat conversion efficiency of gold nanorods with the longitudinal absorption peaks in the first (700-950 nm) and second NIR biological window (1000-1400 nm) [85]. The authors produced gold nanorods with 28 × 7 and 77 × 16 nm with longitudinal absorption peaks at 808 nm and 1000 nm. The authors observed that the heating efficiency of gold nanorods with 28 × 7 nm was ≈40% superior to that of 77 × 16 nm gold nanorods. Further, the subcutaneous injection (5 µl, 1.0 × 10^{11} nanoparticles per mL) of gold nanorods in chicken breast tissues demonstrated the upon irradiation with NIR laser (808 or 1090 nm, 1 W.cm^{-2}), the heating generated by the 28 × 7 nm gold nanorods (808 nm laser) is limited to the injected area, whereas the heating of 77 × 16 nm gold nanorods (1090 nm laser) spread to adjacent tissues. Xu and co-workers functionalized gold nanorods with Anti-HER2 antibody-modified hyaluronic acid (HA)-containing hydrazide and thiol groups for the targeted PTT and photodynamic therapy of breast cancer [86]. For this purpose, gold nanorods with 55 × 11 nm were prepared via the seed-mediated growth method and reacted with Anti-HER2 antibody-modified HA-containing hydrazide and thiol groups, exploring the gold-thiol affinity. Additionally, the authors incorporated 5-Aminolevulinic acid and Cy7.5 into the coated nanorods via hydrazone and amide linkages, respectively. The produced gold nanorod-based system presented a longitudinal absorption peak at 800 nm and upon irradiation with a NIR laser (20 μg.mL^{-1}, 808 nm, 2 W.cm^{-2}, for 10 min) mediated a temperature increase up to 55°C. Moreover, the authors reported that the intravenous administration of the gold nanorod-based system (0.2 mL at 1 mg.mL^{-1}) in MCF-7 tumor-bearing mice mediated the increase in the tumor tissue temperature up to 60°C upon NIR laser irradiation (808 nm, 1 W.cm^{-2}, for 5 min). This photothermal effect slowed the tumor growth and when combined with the photodynamic therapy, the tumors were eliminated without reoccurrence for 20 days.

3.1.3. Gold nanocages

Gold nanocages have a hollow quasi-cubic structure with porous walls and emerged as a novel plasmonic nanoparticle with excellent tunable optical properties [47,87]. These gold-based nanoparticles are produced through the use of a galvanic replacement reaction between a silver nanocube template and a gold salt [88]. During this process, due to the different electrochemical potentials between these two metals, silver ions will dissolve into the solution while simultaneously a thin layer of gold is being formed at the silver nanocube outer surface [89]. The thickness of the gold layer is adjusted according to the amount of gold source (*e.g.* $HAuCl_4$) added to the solution. With the extension of this reaction, the silver from the interior of the nanocube and the gold-silver alloy walls will be removed, forming the porous gold cage-like nanostructures. The LSPR peaks of gold nanocages can be adjusted to the NIR region by optimizing the thickness of the gold layer, *i.e.* adjusting the amount of gold source and the Ag/Au ratio. Panfilova *et al* observed a red-shift in the gold nanocubes absorption peak with the increase of $HAuCl_4$ added to the silver nanocubes [90]. The addition of 0.1, 0.2, and 0.5 mL of $HAuCl_4$ (1 mmol.L^{-1}) provoked a shift in the absorption peak from 448 to 480, 500, and 700 nm, respectively. The authors also described changes in the structure of the nanocube, the addition of 0.1 mL of the $HAuCl_4$ solution resulted in the production of Au/Ag "alloy islands" and the increase to 0.2 mL promoted the transition of this nanostructures to nanoboxes, which progressed to hollow gold nanocages with the increase of $HAuCl_4$ solution to 0.5 mL. Similarly, Yang and colleagues also demonstrated that the addition of increasing volumes of $HAuCl_4$ solution (0.2, 0.4, 0.6, 0.8, 1.6, 1.8, 2.2, 4.0 and 6.0 mL at 0.5 mM) to silver nanocubes induce a gradual red-shift on the LSPR peak from 495 to 1250 nm [91]. Moreover, the authors also observed that excessive amounts of $HAuCl_4$ (volumes superior to 6 mL) had a negative impact on the gold nanocubes absorption, registering a blueshift in the LSPR peak to 530 nm (Fig. 2).

Chen and co-workers developed gold nanocages combined with lauric acid (a phase-change material) for delivering selenous acid (precursor of selenite) in the combinatorial therapy of lung cancer [92]. For that purpose, the gold nanocages with 49 nm of edge length and 5.4 nm of wall thickness were produced using the conventional galvanic replacement process. Then, the hollow cavity of gold nanocages was loaded with lauric acid/selenous acid mixture. The gold nanocages presented the LSPR peak at 810 nm and induced a temperature increase to ≈75°C and ≈50°C upon irradiation with a NIR laser (808 nm, 4 min) at a power density of 0.8 W.cm^{-2} and 0.4 W.cm^{-2}. The authors also demonstrated that this heat generation could prompt the release of selenous acid, the drug concentration increased from 7.5 µg.mL^{-1} when incubated at 37°C to 27 and 72 µg.mL^{-1} upon NIR laser irradiation at a power density of 0.4 W.cm^{-2} and 0.8 W.cm^{-2}. Moreover, the photothermal effect mediated by the gold nanocubes upon NIR laser irradiation (808 nm, 0.8 W.cm^{-2}, for 10 min) mediated the decrease in the A549 tumor cells viability to values close to 58%, and when combined with the simultaneous selenous acid action the viability of A549 cells decreased to 31%.

3.1.4. Gold nanostars

The nanostars are another anisotropic gold nanostructure that is comprised of a small gold core and several gold tips. The gold nanostars are commonly produced using a seed-mediated method. This approach explores the reduction of a gold source (*e.g.* $HAuCl_4$) on small gold spheres in the presence of surfactant agents (*e.g.* CTAB and poly(N-vinylpyrrolidone)). The surfactant agents will direct the anisotropic growth of the tips of gold nanostars, additionally, silver nitrate can be added to the reaction increasing the control over the particle morphology [93,94]. The LSPR phenomenon in gold nanostars is dependent on the core size as well as the tips dimension, number, and shape. In general, the gold nanostars LSPR peak red-shifts with the increase in the core size, number of tips, tip length, and sharpness [95]. Yuan and co-workers demonstrated that the increase of Ag^+ concentrations (5 µM, 10 µM, 20 µM, 30 µM) led to gold nanostars with an increased number of tips (4 to 10) as well as longer and sharper tips [93]. Accordingly, these morphological changes also impacted the gold nanostars LSPR absorption peak from 600 to 1000 nm. Further, the authors showed that the shift in the LSPR absorption peak is related to the changes in the ratio between the length and base width of the tips, increased ratios result in the tuning of LSPR peaks to the NIR region. Additionally, the increase in the number of tips and its length as well as core size resulted in absorption peaks with higher intensity. Espinosa *et al* also observed that an increase in the gold nanostars diameter (25, 55, 85, 120, and 150 nm) led to a red-shift on the LSPR absorption peak from 700 nm (25 nm gold nanostars) to 790, 800, 900, and 950 nm for the nanostars with 55, 85, 120, and 150 nm in diameter, respectively [96]. Further, the gold nanostars irradiation (808 nm, 1 W.cm^{-2}, for 10 min) induced a temperature increase of ≈18°C, ≈45°C, and ≈36°C for the 25, 85, and 150 nm nanoparticles. Li and colleagues produced polydopamine (PDA) coated gold

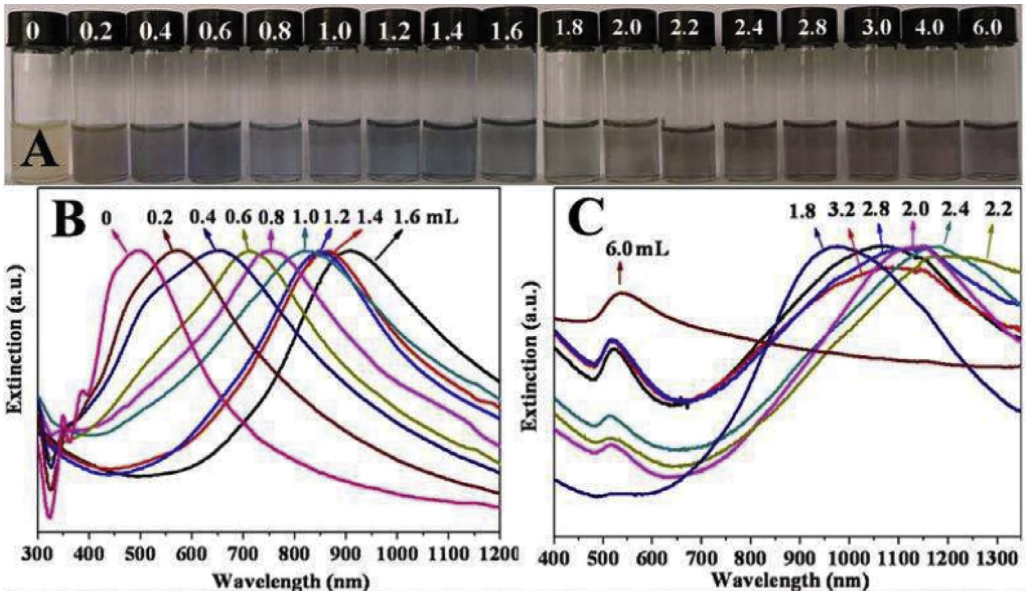

Fig. 2. Characterization of the gold nanocubes absorption spectra. Photographs (A) and UV-vis absorbance spectra (B) of the gold nanocubes solutions with increasing amounts (0.2- 6.0 mL) of 0.5 Mm $HAuCl_4$. Reprinted with permission from Chemistry of Materials, Vol 25, Yang, J., Shen, D., Zhou, L., Li, W., Li, X., Yao, C., Wang, R., El-Toni, A.M., Zhang, F., and Zhao, D., Spatially confined fabrication of core-shell gold nanocages@ mesoporous silica for near-infrared controlled photothermal drug release, Pages No.3030-3037. Copyright (2013) American Chemical Society.

nanostars for mediating the PTT of cervical cancer [97]. For that purpose, the gold nanostars were produced using the conventional seed-mediated method and then modified with thiolated PEI, gold-thiol affinity, and coated with PDA. The produced gold nanostars presented a mean diameter of 74 nm and the LSPR peak at 726 nm. The authors demonstrated that the gold nanostars (Au concentration 0.35 mM) upon NIR laser irradiation (808 nm, 1.3 $W.cm^{-2}$, for 5 min) could mediate a temperature increase up to 40.2°C with a light-to-heat conversion efficiency of 40%. Moreover, the intratumoral injection of the PDA coated gold nanostars (Au concentration 5.6 mM) mediated the increase of HeLa tumors to 58.7°C upon irradiation with NIR laser (808 nm, 1.3 $W.cm^{-2}$, for 10 min) promoting the complete ablation at 20 days posttreatment. Wang and coworkers developed Chlorin e6-PEG-functionalized gold nanostars to mediate the photodynamic and PTT treatment of breast cancer [98]. In this approach, the gold nanostars were initially modified with a thiol-terminated PEG, which was subsequently modified with Chlorin e6 via carbodiimide chemistry. The resulting gold nanostars presented a mean size of 54 nm and a LSPR absorption band at 670 nm. The authors observed that the irradiation of Chlorin e6-PEG-functionalized gold nanostars with a laser (671 nm, 2 $W.cm^{-2}$, for 10 min) could mediate a temperature increase up to 65°C as well as induce the generation of reactive oxygen species. Further, the authors also demonstrated that the intratumoral injection of gold nanostars in MDA-MB-435 tumor-bearing mice could be explored to induce a 23°C increase in the tumor tissue temperature upon laser irradiation (671 nm, 1 $W.cm^{-2}$, for 6 min), which decreased the tumor growth during 14 days. Otherwise, the combinatorial treatment mediated by the Chlorin e6-PEG-functionalized gold nanostars significantly reduced the volume of MDA-MB-435 tumors being observed extensive cancer necrosis and a decreased oxygen saturation.

3.2. Gold-based nanohybrid materials

Apart from the optimization of the gold nanoparticles' size, morphology, and organization, these nanostructures can be combined with other materials to improve their therapeutic potential (Table 2). Various multifunctional gold-based nanohybrid materials have been prepared to improve both the gold nanostructures PTT capacity as well as its stability and resistance to photodegradation (Fig. 3).

3.2.1. Gold-silica nanohybrids

The silica is a chemically inert and biocompatible material that can improve the colloidal stability of gold nanostructures [99]. The inclusion of silica derivatives, such as mesoporous silica, can also increase the drug loading capacity of gold nanoparticles [100]. Further, the silica NIR light transparency does not impact the excitation of gold cores during the PTT [101]. The modification of gold nanomaterials with silica can be performed using the conventional Stöber method or its derivations [102]. During this procedure, a silica shell is formed in the surface of the gold nanostructures by promoting the condensation of a silica precursor (*e.g.* tetraethyl orthosilicate) under alkaline conditions [11,44,62,103]. The silica shell on gold nanostructures can be fine-tuned to optimize the LSPR peak wavelength and intensity of gold-silica nanohybrids. Fernandez-López and colleagues observed that the introduction of a silica shell in gold nanospheres results in a red-shift in the LSPR absorption peak [104]. The authors observed that the red-shift in the LSPR absorption peak was dependent on the size of the gold nanosphere. The deposition of silica shells with 24 nm in thickness resulted in a ≈33 nm shift in the absorption peak, from ≈680 to ≈713 nm, for gold nanospheres with 142.8 nm in diameter, whereas in gold nanospheres with 98.5 nm and 60.4 nm the red-shift in the absorption peak was 10 and 8 nm, respectively. Similarly, Zhang and co-workers reported a red-shift on the longitudinal LSPR peak of gold nanorods with the formation of a silica shell [105]. The authors observed that the growth of a silica shell on the surface of gold nanorods induced a ≈10 nm red-shift in the longitudinal LSPR peak (from 799 to 813 nm) when the silica thickness reached the 7 nm. The further growth of the silica shell to 14 nm provoked an additional 10 nm shift in the longitudinal LSPR peak to 823 nm (Fig. 4).

Furthermore, Khlebtsov *et al* reported that the increase in the shell thickness of silica-coated gold nanocages from 10 to 120 nm impacts both the LSPR peak wavelength and magnitude [106]. The authors observed the red-shift in the LSPR peak with the increase

Table 2
Overview of the main gold nanohybrids explored to mediate a photothermal effect (N.D. – non disclosed, N.A. – not applicable).

Nanohybrid	Gold Shape	Size	Surface Modification	LSPR peak	Loading	Photothermal Effect		Type of Study	Test Model	Main Results	Ref.
						Laser Parameters	Temperature				
G/S	NSP	15.5, 60.5, 98.5, and 142.8 nm GNSP coated with 6.1,21.0, 20.9 and 24.2 nm silica shell	mPEG-SH	Broad absorption from 550 to 900 nm	N.A.	N.A.	N.A.	N.A.	N.A.	The LSPR absorption peak was dependent on the size and shape GNP, and silica.	[104]
	NR	GNR (L: 67.4, W: 14.3) coated with 3.7, 9.1, 18.9 and 30.7 nm silica shell		≈800 nm							
	NC	Silica coated (12-127nm) GNC (60 nm) with 3, 4, and 5 nm of gold thickness	N.A.	775-817 nm	N.A.	N.A.	N.A.	N.A.	N.A.	The increase of silica shell thickness led to an increase in the LSPR absorption peak maxima of GNC.	[106]
	NR	GNR (L: 84 nm, W: 24 nm) coated with 7 and 14 nm silica shell	PEG-SH	7 nm silica shell: 813 nm; 4 nm silica shell: 823 nm	ICG	808 nm, 230 $W.cm^{-2}$, 10 min	≈50°C	*In vitro*	HepG2 cells	The PTT effect mediated by the G/S nanohybrid provoked the reduction of the HepG2 cell viability to ≈40%.	[105]
	NR	GNR (L: 34 nm, D: 9 nm) coated with 6-20 nm silica thickness	PEG	Broad absorption from 600 to 900 nm	N.A.	808 nm, 300 pulses of 7 ns at fluences of 4 $mJ.cm^{-2}$ to 20 $mJ.cm^{-2}$	N.A.	N.A.	N.A.	The non-coated GNR irradiation at fluences superior to 4 $mJ.cm^{-2}$ resulted in absorption losses in the NIR region of the spectra. Otherwise, the silica shell increased the photostability of GNR, avoiding significant changes in the UV-vis spectra after NIR laser irradiation.	[107]
	NR	GNR (L: 51.6 nm, W: 13.2 nm, A.R: ≈ 3.9) coated with a 25 nm silica shell	RGD and PEG	840 nm	DOX	808 nm, 3 $W.cm^{-2}$, 30 s	55°C	*In vitro/In vivo*	A549 cells/A549 tumor bearing mice	The G/S nanohybrids mediated the increase of A549 tumors' temperature up to 65.9°C presenting a final tumor weight ≈0.4 g, contrasting with the ≈0.9 g of the control group. The combinatorial chemo-PTT treatment presented an enhanced antitumoral effect de (final tumor weight ≈0.2 g).	[169]
	NR	GNR (L: 40 nm, W: 10 nm) coated with a 10-13 nm silica shell	PEG	840 nm	DOX	N.D.	ΔT=9°C	In vitro/In vivo	MCF-7 cells/ Ehrlich ascites cells Balb/c mice	The G/S nanohybrids mediated a 14°C increase of Ehrlich tumors' temperature, which resulted in the reduction of the tumor volume for 3 days followed by the tumor regrowth until day 18.	[170]
	NR	GNR (A:3.4) coated with a 35 nm silica shell	1-tetradecanol and FA	850 nm	DOX	802 nm, 1 $W.cm^{-2}$, 10 min	≈60°C	*In vitro*	KB cells	The PTT effect mediated by the G/S nanohybrid provoked the reduction of KB cell viability to ≈50%, which was improved when combined with the Dox action, KB cells viability ≈30%.	[171]

(*continued on next page*)

Table 2 (*continued*)

Nanohybrid	Gold Shape	Size	Surface Modification	LSPR peak	Loading	Photothermal Effect		Type of Study	Test Model	Main Results	Ref.
						Laser Parameters	Temperature				
G/GO	NS	400 nm nanostructure comprised of 40 nm GNS	PEG	Peak at 660 nm and broad absorbance from 600 to 900 nm	Ce6	660 nm; 2 $W.cm^{-2}$, 10 min	≈60°C	*In vitro/In vivo*	EMT6, HeLa cells/EMT6 tumor-bearing mice	The PTT mediated by the G/GO nanohybrid mediated the ablation of EMT6 tumors in 14 days.	[112]
	NSP	Nanostructure with 230 nm diameter comprised of GO coated with 15 nm GNSP	Matrix metalloproteinase-14 (MMP14)	Peak at ≈700 nm and broad absorbance from 700 to 1000 nm	Cy5.5	808 nm, 0.5 $W.cm^{-2}$, 10 min	ΔT≈25°C	*In vitro/In vivo*	SCC7 cells/SCC7 tumor-bearing mice	The nanohybrid mediated a 16°C increase in the tumor temperature under NIR laser irradiation, which induced the complete ablation of SCC7 tumors without recurrence for 14 days	[172]
	NSP	Reduced GO (rGO) (lateral size of 150 nm) coated with gold superparticles (aggregates of 15 nm gold particles)	PEG	Broad absorbance from 600 to 900 nm	N.A.	808 nm, 0.3 and 0.8 $W.cm^{-2}$, 5 min	0.8 Wcm^{-2}: ΔT≈65°C	*In vitro/In vivo*	U87MG cells/U87MG bearing mice	U87MG tumors treated with the rGO-gold nanohybrids registered a temperature increase to 58°C resulting in the tumor eradication in 2 days, without recurrence for 14 days.	[173]
	NR	GNR with 31 nm × 8 nm coated with a 1.3 nm GO layer	Polystyrene sulfonate modified	≈750 nm	N.A.	808 nm, 0.8 $W.cm^{-2,}$ 10 min	49.9°C	*In vitro/In vivo*	SW1990 cells/SW1990 tumor-bearing mice	The PTT mediated by the nanohybrids induced the death of 80% of the SW1190 cells *in vitro* as well as provoked the volume reduction of SW1190 tumors.	[174]
	NR	GNR (L: 53.1 nm, W: 13.8 nm, AR:3.8) coated with a 2.6 nm nanographene oxide (NO) shell	HA	≈760 nm	DOX	808 nm, 1 $W.cm^{-2}$, 5 min	N.D.	*In vitro*	Huh-7 cells	The PTT and chemotherapy combination induced the death of 82% of Huh-7 cancer cells, which corresponds to a 1.5-fold and 4-fold increase when compared to the stand-alone approaches, 53% and 22% of cell death in chemotherapy and PTT, respectively.	[110]
	NR	GNR (AR: 3.8) coated with a 6 nm rGO shell	PEG, Tat protein vector, and Cy7	814 nm	N.A.	808 nm, 1 $W.cm^{-2}$, 10 min	N.D.	*In vitro/In vivo*	U87MG cells/U87MG tumor-bearing mice	The G/GO nanohybrids promoted the increase of U87MG tumors temperature to 52.5°C, which induced the reduction of the tumor size from 500 mm^3 at day 18 to less than 100 mm^3 at day 33.	[111]
	NS	Nanostructure comprised of 60 nm GNS coated with GO	PDA and PEG	Broad absorbance from 600 to 800 nm	DOX	655 nm, 8.0 $W.cm^{-2}$, 2 min	≈55°C	*In vitro/In vivo*	4T1 cells/4T1 tumor-bearing mice	The PTT effect mediated by the G/GO nanohybrids induced a 30°C increase in the tumor's temperature, which reduced the growth of 4T1 tumors. The PTT combination with the Dox action resulted in the elimination of the 4T1 primary tumors as well reduced the number of metastasis nodules found in lung sections	[175]

(*continued on next page*)

Table 2 (*continued*)

Nanohybrid	Gold Shape	Size	Surface Modification	LSPR peak	Loading	Photothermal Effect		Type of Study	Test Model	Main Results	Ref.
						Laser Parameters	Temperature				
	NR	GNR/rGO 30 s (L:38.3 nm, W: 19.5 nm, AR: 2 nm); GNR/rGO 1 min (L: 32.2 nm, W: 16.3 nm, AR: 2.03 nm); GNR/rGO 3 min (L: 24.3 nm, W: 10.8 nm, AR: 2.36 nm).	N.A.	600-700 nm	N.A.	808 nm, 0.5 W, 10 min	ΔT GNR/rGO 30 s: 13.5°C; ΔT GNR/rGO 1 min: 14.8°C; ΔT GNR/rGO 3 min: 17.4°C;	N.A.	N.A.	The G/GO nanohybrids present a higher temperature variation than GO (3.9°C), GNR (6.8°C), and rGO alone (12.2°C).	[176]
	NS	Nanostructure comprised of ≈80 nm GNS absorbed on rGO layers	Chitosan and FA	≈750 nm	DOX and protopor-phyrin IX	808 nm, 1 $W.cm^{-2}$, 1 min	≈40°C	*In vitro/In vivo*	MDA-MB-231 cells/DLA tumor-bearing mice	The PTT effect mediated by the G/GO nanohybrids reduced the tumor growth, which combined with the PDT and chemotherapy action mediated the decrease of DLA tumors' volume after 8 days.	[177]
	NR	Gold core (L: 31, W: 8.0) silica shell NPs coated with GO (thickness 0.9–1.4 nm)	PEG	788 nm	DOX	808 nm,2 $W.cm^{-2}$, 60 min	ΔT≈25°C	N.A.	N.A.	The GNRs/SiO_2/GO-PEGs had the highest temperature increment (23.5°C), comparing with GNRs/SiO_2 (21°C) and GO-PEG (≈5°C) under NIR laser irradiation (2 $W.cm^{-2}$).	[178]
	NCL	50 nm GNCL coated with 5 nm GO quantum dots	FA	Broad absorbance from 600 to 800 nm	DOX	808 nm, 1.5 $W.cm^{-2}$, 10 min	ΔT≈40°C	*In vitro/In vivo*	HeLa and A549 cells/HeLa tumor-bearing mice	The PTT mediated by the G/GO nanohybrid induced a 40°C increase in the tumors' temperature reducing tumor growth. The combination with the Dox action provoked the elimination of HeLa tumors with one mouse was relapsing after 18 days.	[179]
	NR	GNR with 50 × 10 nm absorbed on rGO layers	PVP and hydroxyapatite	871 nm	5-fluorouracil	808 nm, 1 $W.cm^{-2}$, 10 min	66.1°C	*In vitro*	HeLa cells	The PTT and chemotherapy mediated by NPs led to a tumor cell death of 72.2 %, whereas the single PTT or chemotherapy only induced 51.9% and 55.8% of cell death, respectively.	[180]
	NR	GO wrapped GNR	N.A.	Broad absorbance from 700 to 900 nm	DOX	808 nm, 0.5 $W.cm^{-2}$, 10 min	≈70°C	*In vitro/In vivo*	Hela cells/HeLa tumor bearing mice	The PTT and chemotherapy mediated by G/GO nanohybrids reduced the HeLa cells viability to 5%, whereas HeLa cells treated in the absence of laser irradiation had a viability of 15%. In vivo, the chemo-PTT treatment induced the decrease of the volume of HeLa tumors.	[181]
	NSP	60 nm NPs comprised of gold cores coated with GO (2-3 nm)	PEG	Peak at 550 and broad absorbance from 600 to 1000 nm	zinc phthalo-cyanine	808 nm, 0.67 $W.cm^{-2}$, 20 min	In 12 min ≈35°C	*In vitro*	HeLa cells	The PTT effect of G/GO nanohybrids decreased the HeLa cells viability to 29.3%, which combined with the zinc phthalocyanine action further reduced cell viability to 6.8%.	[182]

(*continued on next page*)

Table 2 (*continued*)

Nanohybrid	Gold Shape	Size	Surface Modification	LSPR peak	Loading	Photothermal Effect		Type of Study	Test Model	Main Results	Ref.
						Laser Parameters	Temperature				
	NSP	≈60 nm thickness Nanostructure comprised of 37.1 or 47.1 nm GNSP es coated with α-synuclein protein (≈8.5 nm) adsorbed on GO nanosheets	α-synuclein protein	Peak at ≈600 m and broad absorbance to 900 nm	N.A.	808 nm, 1.0 W.cm^{-2}, 5 min	ΔT≈30°C	*In vitro/In vivo*	MSCs cells/MSC tumor-bearing mice	The PTT effect mediated by the G/GO nanohybrids suppressed the MSC tumor growth for 21 days.	[183]
	NS	GO sheets (lateral dimension of ≈0.5 μm and thickness of 1 nm) coated with GNS	N.A.	802 nm	N.A.	808 nm, 0.75 W.cm^{-2}, 2 min	54.4°C	*In vitro*	SKBR-3 cells	SKBR-3 cells treated with 10 μg/mL of GO-GNS under laser irradiation had a viability of 19 % and ≈0%, at 24 and 48h respectively. The individual treatment with GO or GNS alone only reduced the viability of SKBR-3 cells to 80%.	[184]
	NR	Nanostructure with 173 nm diameter comprised of GO coated with GNR (L: 40 nm W:13 nm A.R.:3.07)	N.A.	774 nm	N.A.	808 nm, 300 mW, 5 min	56.4°C	*In vitro*	HeLa cells	GO/GNR hybrids presented a higher photothermal efficiency (72.59%) comparing with individual GO nanosheets (18%) and GNR (35%). The PTT effect mediated by the GO/GNR mediated the decrease in the viability of HeLa cells to 4.17 %, whereas the GO nanosheets and GNR groups only reached the 34.92% and 19.24%, respectively.	[185]
G/IO	NSH	611.7 nm GO nanostructure functionalized with IO/gold core-shell NPs	PEG	Peak at ≈550 nm and broad absorbance to 800 nm	DOX	808 nm, 2 W.cm^{-2}, 5 min	ΔT≈25°C	*In vitro*	HeLa cells	The PTT effect of the nanohybrids induced the decrease in the viability of HeLa cells to ≈15%, which was further reduced to ≈3% with the combined action of Dox.	[186]
	NSP	200 nm nanostructure composed of Black phosphorus sheets (BPs) enriched with 2 nm GNSP and 6 nm Fe_3O_4 NPs	N.A.	Peak at 650 nm and broad absorbance to 900 nm	N.A.	808 nm, 0.5 W.cm^{-2}, 5 min	≈50°C	*In vitro/In vivo*	HeLa and L929 cells/U14 tumor-bearing mice	The PTT mediated by BPs@Au@Fe_3O_4 induced the increase of the temperature of the tumor to values close to 60°C, which induced a decrease in the growth of U14 tumors.	[187]
	NSH	100 nm iron oxide NCL coated with a GNSH	PEG and poly (acrylic acid)	≈900 nm	N.A.	808 nm, 0.5 W.cm^{-2}, 10 min	≈55°C	*In vivo*	4T1 tumor-bearing mice	The G/IO nanohybrids induced an increase in the tumor temperature up to ≈55°C, which combined with the magnetic targeting resulted in the ablation of cancer cells at the primary tumor site and lung metastases improving the mice survival up to 60 days.	[118]

(*continued on next page*)

Table 2 (*continued*)

Nanohybrid	Gold Shape	Size	Surface Modification	LSPR peak	Loading	Photothermal Effect		Type of Study	Test Model	Main Results	Ref.
						Laser Parameters	Temperature				
	NSH	20 nm iron oxide cores coated with a GNSH (3 nm)	FA	Peak at 606 nm and broad absorbance to 800 nm	N.A.	808 nm, 6 $W.cm^{-2}$, 10 min	43.9°C, 45.9°C, and 48.5°C for gold concentrations of 20, 30 and 40 μg, respectively.	*In vitro*	Human nasopharyngeal (KB) cells	The PTT effect mediated by the G/IO nanohybrid provoked the reduction of the viability of KB cells to 44.3%.	[188]
	NF	12.2 nm gold /2.1 nm ultrasmall IO nanocomplexes.	G5 poly(amidoamine) (PAMAM) dendrimers	680–730 nm	N.A.	808 nm, 1.2 $W.cm^{-2}$, 5 min	45°C	*In vitro/In vivo*	4T1 cells/4T1 tumor-bearing mice	The G/IO nanohybrids induced an increase in the tumor temperature up to ≈57°C reducing the growth of 4T1 tumors. Further, the PTT and radiotherapy combination resulted in the eradication of the 4T1 tumors after 4 days without recurrence for 40 days.	[189]
	NSH	≈100 nm hollow GSP (wall thickness of 4.27 nm) coated with 6.27 nm Fe_3O_4 NPs	FA	830 nm	N.A.	808 nm, 4.12 $W.cm^{-2}$, 5 min	63.4°C	*In vitro*	HeLa cells	The PTT effect mediated by the G/IO nanohybrids provoked the death of the HeLa cells in the irradiated area.	[117]
	NCL	Mesoporous IO/NCL coated with 10 nm GNP	PEG	704 nm	PTX and DOX	808 nm, 2.5 $W.cm^{-2}$, 5 min	≈55°C	*In vitro/In vivo*	MCF-7 and 293A cells/4T1 tumor bearing mice	The PTT effect mediated by the G/IO nanohybrids induced a temperature increase to 49.3°C suppressing the growth of 4T1 tumors growth. The combination with the exposition to a magnetic field and Dox significantly decreased the 4T1 tumors volume during 16 days.	[190]
	NSP	120 nm Janus NPs composed of 50 nm GNSP and carbon-encapsulated Fe_3O_4 NPs	Polyacrylic acid, PEG, and FA	Broad absorbance from 600 to 1000 nm	DOX	808 nm, 1 $W.cm^{-2}$, 5 min	42°C	*In vitro*	HeLa cells	The PTT effect mediated by the G/IO nanohybrid provoked the reduction of HeLa cells viability to ≈50%, which was improved when combined with the Dox action, HeLa cells viability inferior to 10%.	[191]
	NSP	Silica coated gold (30 nm) and iron oxide (20 nm) NPs aggregates	N.A.	530-550 nm	N.A.	785 nm, 4.9 $W.cm^{-2}$, 4 min	71.8°C	*In vitro*	MDA-MB-231 cells	The G/IO nanohybrids mediated the complete elimination of MDA-MB-231 cells upon NIR irradiation.	[**192**]
	NSH	185 nm nanocomplexes comprised of a GNSH coated with a silica layer doped with IO NPs (10 nm)	Streotavidin and Biotinylated anti-HER2	822 nm	ICG	808 nm, 3.72 $W.cm^{-2}$, 10 min	N.D.	*In vitro*	SKBR3 and MDA-MB-231 cells	The PTT effect mediated by the G/IO nanohybrids provoked the death of the cancer cells in the irradiated area.	[193]

(*continued on next page*)

Table 2 (*continued*)

Nanohybrid	Gold Shape	Size	Surface Modification	LSPR peak	Loading	Photothermal Effect		Type of Study	Test Model	Main Results	Ref.
						Laser Parameters	Temperature				
G/PDA	NS	114 nm PDA coated GNS (90 nm)	PEG	806 nm	N.A.	808 nm, 2.0 W.cm^{-2}, 10 min	≈55°C	*In vitro*	HeLa cells	The HeLa cells' viability decreased from 53.57% to 19.66, 13.97, 10.43, and 10.02% with the increase of the irradiation time from 1 to up to 5 min, respectively.	[194]
	NS	150 nm PDA coated GNS (55 nm)	PEG	860 nm	DOX	808 nm, 10 W.cm^{-2}, 5 min	≈50°C	*In vitro/In vivo*	CT26 cells/CT26 tumor-bearing mice	The PTT effect mediated by the G-PDA nanohybrids induced a ≈13°C increase in the tumor's temperature, leading to a decrease in the tumor volume and achieving complete eradication in 75% of the animals without recurrence for 50 days.	[119]
	NSH	296 nm IO and gold cores (25-40 nm) coated with PDA (4 nm)	Fe_3O_4, FA	Broad absorbance from 400 nm to 1000 nm	DOX	808 nm, 0.75 W.cm^{-2}, 5 min	≈70°C	*In vitro*	4T1 cells	The combined chemo-PTT mediated by Fe_3O_4/Au/PDA/FA/DOX nanohybrids decreased the viability of 4T1 cells to 18%, whereas the treatment with free DOX only presented a reduction in the cell viability to 82%.	[195]
	NS	GNS (50 nm) nanostructure coated with PDA	PDA, PEI, FA	≈800	N.A.	808 nm, 0.33 W.cm^{-2}, 10 min	ΔT≈20°C	*In vitro/In vivo*	MCF-7 cells/MCF-7 tumor bearing mice	The tumor mice injected with APP-ICG were almost eradicated after NIR irradiation, whereas no significant alterations were observed in the tumors treated with APP or ICG.	[196]
G/PPy	NR	PPy (16.17 nm) functionalized GNR (L: 57.98 nm W: 13.9 D53nm, A.R:4) enriched with iron oxide NPs	PVP and FA	798 nm	DOX	808 nm, 2 W.cm^{-2}, 10 min	58.3°C	*In vitro/In vivo*	HepG2 and SMMC-7721 cells / HepG2 tumor-bearing mice	The PTT effect mediated by the nanohybrids decreased the growth of HepG2 tumors (relative tumor volume of 6 at day 13), which was further improved with the simultaneous Dox action (relative tumor volume of ≈3 at day 13).	[197]
	NSP	≈100 nm PPy coated GNP (≈6 nm)	Aptamer S2.2	810 nm	N.A.	808 nm, 0.5 W.cm^{-2}	≈55°C	*In vitro/In vivo*	MCF-7 cells/ MCF-7 tumor-bearing mice	The heat generated by the G-PPy nanohybrids induced the temperature increase of MCF-7 tumors to ≈50°C, leading to a significant decrease in the tumor volume (10% of the control group).	[198]
	NSP	82.1 nm PPy nanostructure coated with GNP (2 nm)	PEI and PEG	Broad absorbance from 400 nm to 800 nm	N.A.	808 nm, 1.5 W.cm^{-2}, 10 min	≈55°C	*In vitro*	4T1 and L929 cells	The PPT effect of the nanohybrids induced the decrease of 4T1 cells' viability to 25%, whereas the PPy nanostructures alone only achieved a reduction in the cell viability to 35%.	[120]
	NR	Nanostructure with 100 nm comprised of GNR (L: 75 nm, W: 25 nm) coated with PPy (20 nm) and silica (15 nm)	N.A.	≈800 nm	DOX	808 nm, 3 W.cm^{-2}, 10 min	ΔT≈17°C	*In vivo/In vitro*	CT26 cells/CT26 tumor bearing mice	The G-PPy nanohybrids mediated the increase of the temperature in CT26 tumors to above 50°C, which resulted in the almost complete tumor elimination after 15 days.	[199]

(*continued on next page*)

Table 2 (*continued*)

Nanohybrid	Gold Shape	Size	Surface Modification	LSPR peak	Loading	Photothermal Effect		Type of Study	Test Model	Main Results	Ref.
						Laser Parameters	Temperature				
G/Cu	NR	Core–shell and dumbbell-like G/Cu nanostructures (L:84.2 nm/ W: 36.6 nm or L: 61.4 nm/ W: 20.6 nm), comprised of GNR (L: 75.9 nm/ W: 24.8 nm or L:75.9 nm / W: 14.6 nm) coated with Cu sulfide (5-12 nm).	PEG	803 or 809 nm	N.A.	808 nm, 0.9 W.cm^{-2}, 10 min	ΔT core-shell=2.1°C; ΔT dumbell-like=31.2°C	*In vitro*	HeLa cells	Core-shell and dumbbell-like G/Cu nanohybrids present higher photothermal efficiency (η=62% and 56%, respectively) than pure GNR. (η=39%). The PTT effect mediated by the gold-copper nanohybrids induced the death of ≈80% of the HeLa cells.	[121]
	NSP	GNP: (27 nm) coated with a $Cu_{2-x}S$ shell with 13.5 nm thickness	N.A.	800-1000 NM	N.A.	808 nm, 0.75 W.cm^{-2}, 10 min	≈60°C	*In vitro/In vivo*	4T1 cells/4T1 tumor-bearing mice	The G-CU NSPs mediated the increase of the temperature in 4T1 tumors to 60°C, which resulted in the reduction of the tumors volume for 21 days.	[200]
G/Mo	NB	GNB (L:110 nm, W: 36 nm) coated with Mo disulfide (1.5-2 nm)	PEG	837 nm	N.D.	808 nm, 2 W.cm^{-2}, 10 min	≈60°C	*In vitro*	HeLa cells	The PTT mediated by the G/Mo nanohybrids reduced the HeLa cells viability to 21.6%, whereas in the group treated with GNB the HeLa cells viability only decreased to 46.2%.	[122]
	NR	Nanosctrure with ≈103 nm comprised of MoS2 coated with GNR (L:50 nm, width:14 nm, A.R.: 3.5)	PEG	788 nm	ICG	808 nm, 0.2 W.cm-2, 5 min	57°C	*In vitro/In vivo*	HeLa cells/HeLa tumor-bearing mice	The PTT mediated by the G/Mo nanohybrids stalled the growth of HeLa tumors for 14 days, whereas the combined action with ICG mediated the almost complete tumor elimination after 14 days.	[201]

Abbreviations: NSH-Nanoshell; NCL-Nanocluster; NR-Nanorod; NC-Nanocage; NS-Nanostar; NF-Nanoflower; NB-Nanobipyramid; GNSH-Gold nanoshell; GNCL-Gold nanocluster; GNR-Gold nanorod; GNC-Gold nanocage; GNS-Gold Nanostar; GNF-Gold nanoflower; GNB-Gold nanobipyramid; NPs-nanoparticles; G/NPs-Gold nanoparticles; G/S-Gold/Silica nanohybrid; G/GO-Gold/Graphene Oxide nanohybrid; G/IO-Gold/Iron Oxide nanohybrid; G/PPY-Gold/Polypyrrole nanohybrid; G/PDA-Gold/Polydopamine nanohybrid; G/Cu-Gold/Copper nanohybrid and G/Mo-Gold/Molybdenum nanohybrid.

Please cite this article as: A.S.C. Gonçalves, C.F. Rodrigues and A.F. Moreira et al., Strategies to improve the photothermal capacity of gold-based nanomedicines, Acta Biomaterialia, https://doi.org/10.1016/j.actbio.2020.09.008

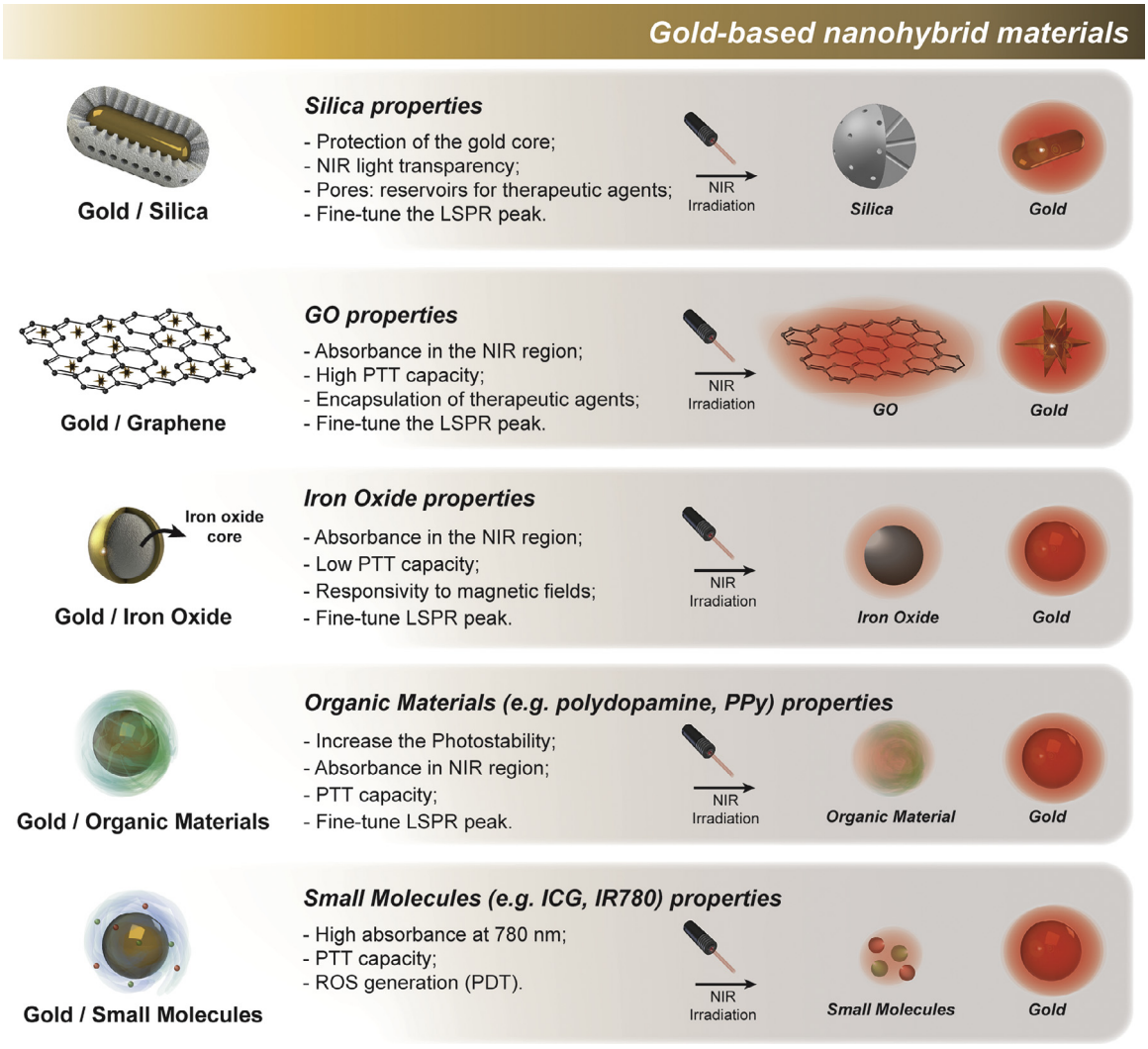

Fig. 3. Representation of the main gold-based nanohybrid materials and their contribution to improving the PTT capacity of gold nanomaterials.

of the silica shell thickness, *e.g.* from 775 to 802 nm with a 20 nm shell thickness, as well as a gradual increase in the LSPR maxima.

Otherwise, the silica shell also protects the gold nanomaterials from photodegradation phenomena. The gold nanostructures exposition to high energetic radiations and high temperatures has been associated with the reshaping of the nanoparticles and loss of the NIR absorption capacity. Nevertheless, Chen and colleagues observed that the coating of gold nanorods with a silica shell enhances the thermal stability of the nanoparticles [107]. The authors observed that the gold nanorods irradiation with 300 laser pulses of 7 ns duration at fluences superior to 4 mJ.cm^{-2} resulted in alterations in the longitudinal LSPR peak, 10% amplitude decrease in 800 nm region upon irradiation at 8 mJ.cm^{-2} and a strong increase of the absorption in the 600–650 nm range at higher fluences. These changes on the gold nanorods absorption spectra were consistent with the reshaping of the nanoparticles, namely the rounding of gold nanorods. However, the absorption spectra of silica-coated gold nanorods with a shell thickness of 20 nm remained constant, with the authors observing small changes, a 10% decrease in the 800 nm region, only when the silica-coated gold nanorods were irradiated at 20 mJ.cm^{-2}.

3.2.2. Gold-graphene nanohybrids

Graphene oxide (GO) a single-atom-thick layer of sp^2 hybridized carbon atoms and can be composed of different oxygen-containing groups (*e.g.*, hydroxyl, and epoxy groups) in the edges and base of its aromatic structure [108]. The GO, particularly the reduced GO, present the capacity to absorb in the NIR region, which enables their application in photothermal therapy [109]. Therefore, the combination of gold nanoparticles with graphene materials can improve the NIR absorption of nanomaterials, and consequently their photothermal and bioimaging potential (*e.g* fluoresce imaging, PAI, Raman Imaging). Xu and co-workers produced nano GO-modified gold nanorods functionalized with HA to mediate the delivery of doxorubicin (DOX) and the PTT of liver cancer [110]. For that purpose, the authors produced carboxylated nanosized GO through the modified Hummer's method and exfoliation processes. Then, gold nanorods with a 3.8 aspect ratio (3.1±8.2 and 13.8±3.2 nm) were modified with the nanosized GO via electrostatic interactions. The resulting gold-graphene nanohybrids were further functionalized with HA exploring the carbodiimide coupling chemistry between the carboxyl groups on GO and amine groups of HA. The authors reported that the GO-modified gold nanorods functionalized with HA despite presenting the GO characteristic absorption peak at 239 nm also displayed a significant enhancement in the intensity of the absorption band at the 760-800 nm region. This improvement in the nanomaterials absorption capacity resulted in an enhanced photothermal effect with the gold-graphene nanohybrids inducing an increase in the solution temperature to ≈65°C upon NIR laser irradiation (808 nm, 4

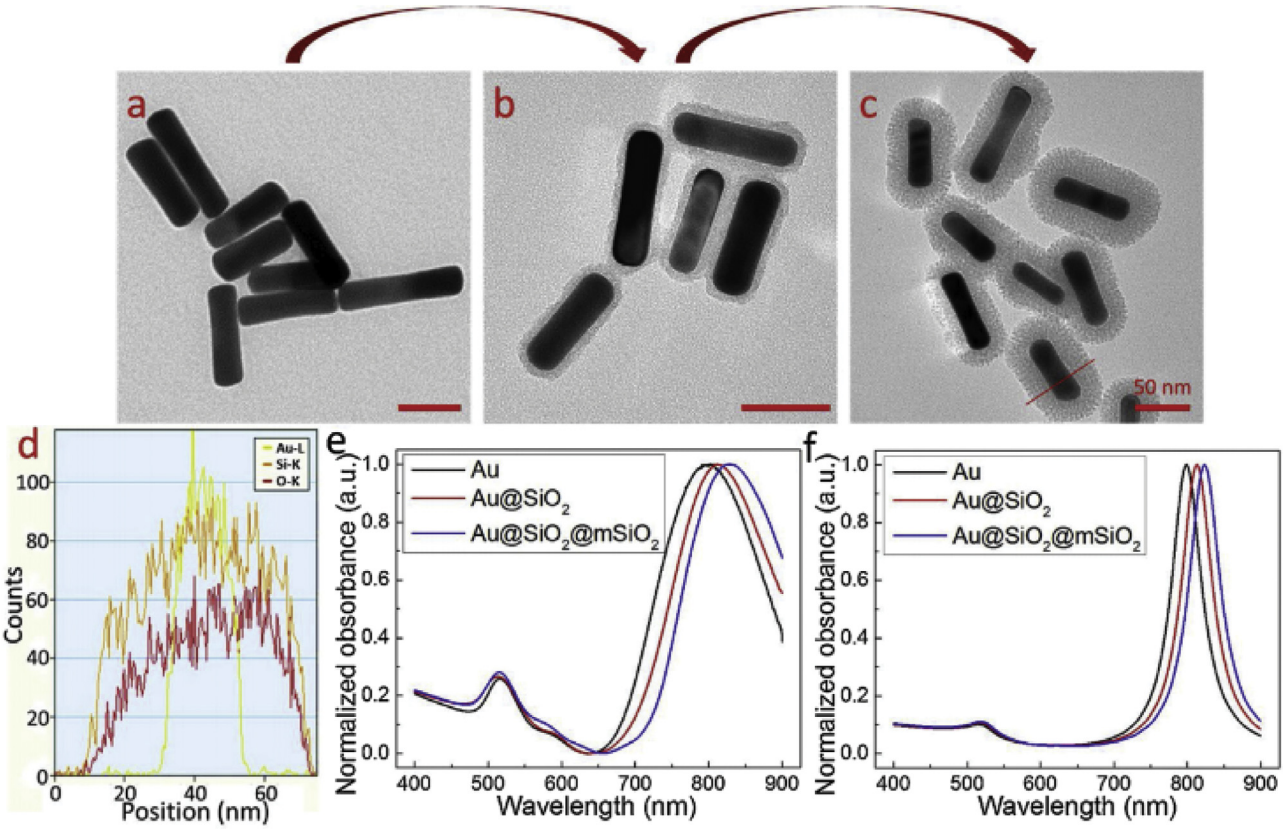

Fig. 4. Physicochemical characterization of gold nanorods, Au@SiO_2, and Au@SiO_2@mSiO_2 nanoparticles. TEM images of gold nanorods (a), Au@SiO_2 (b), and Au@SiO_2@mSiO_2 (c); EDX analysis (d); Nanoparticles UV-vis absorbance spectra and respective LSPR peak changes with silica coating (e); Corresponding extinction spectra calculated by FDTD (f). Reprinted from Journal of Photochemistry and Photobiology A: Chemistry, Vol 375, Zhang, B., Wei, L., and Chu, Z., Development of indocyanine green loaded Au@Silica core shell nanoparticles for plasmonic enhanced light triggered therapy, Pages No.244-251, Copyright (2019), with permission from Elsevier.

W.cm^{-2}, for 3 min), whereas the bare gold nanorods only reached the ≈59°C [110]. Additionally, the authors observed that the photothermal treatment mediated by the HA -functionalized gold-graphene nanohybrids (808 nm, 1 W.cm^{-2}, for 5 min) induced the death of 22% of the Huh-7 cancer cells, which increased when combined with the simultaneous delivery of DOX inducing the death of 82% of the cells. Similarly, Turcheniuk *et al.* also modified gold nanorods with GO nanosheets to improve the PTT of glioblastoma [111]. The gold-graphene nanohybrids were produced by exploring electrostatic interactions between the positively charged gold nanorods (aspect ratio 3.8) and carboxylated nanosized GO and then modified via carbodiimide chemistry with an amine-modified PEG. The authors observed that the GO nanosheets attachment in the gold nanorods led to a red-shift in the longitudinal LSPR peak from 807 to 814 nm as well as an increase in the peak maximum absorbance. Moreover, the authors reported that the irradiation (808 nm, 0.5 W.cm^{-2}, for 10 min) of PEGylated gold-graphene nanohybrids resulted in a temperature increase to 60°C, whereas the gold nanorods only reached the ≈50°C. Additionally, the *in vivo* studies also revealed that the tail vein administration of Tat-targeted PEGylated gold-graphene nanohybrids could be explored to mediate the increase in the temperature of U87MG tumors to 52.5°C after NIR laser irradiation (808 nm, 0.7 W.cm^{-2}, for 10 min). Such resulted in the size reduction of the tumors from 500 mm^3 to ≈250 mm^3, contrasting with the 1750 mm^3 observed in the control group. Wu and colleagues combined gold nanostars with GO for mediating the delivery of Chlorin e6 and the PTT of breast cancer [112]. In this approach, the GO nanosheets were used as supports for the gold nucleation and growth of the gold nanostars. Then, the gold-graphene nanohybrids were functionalized with a thiol-terminated PEG by exploring the gold-thiol affinity. The resulting nanostructures presented an increased absorbance in the NIR region of the spectra, broad absorption peak at 600 to 900 nm region. The enhanced NIR absorption rendered to the gold-graphene nanohybrids a superior photothermal potential prompting the temperature increase up to 75°C upon laser irradiation (660 nm, 2 W.cm^{-2}, for 8 min), whereas the gold nanorods and the GO nanosheets only reached the ≈65°C and ≈47°C, respectively (Fig. 5). Similar data were observed in the *in vivo* studies with the intratumoral administration of PEGylated gold-graphene nanohybrids mediating the temperature increase of EMT6 tumors to 60°C upon laser irradiation (660 nm, 3 W.cm^{-2}, for 10 min), which stalled the tumor growth and when combined with the simultaneous action of Chlorin e6 promoted the tumor eradication.

3.2.3. Gold-iron oxide nanohybrids

Iron oxide nanomaterials due to its plasmonic properties can also mediate a photothermal effect in response to NIR laser irradiation. These nanomaterials can be found in different chemical compositions, such as maghemite (Fe_2O_3), magnetite (Fe_3O_4), or non-stoichiometric combinations of Fe and O [113–115]. Nevertheless, when compared to gold nanomaterials, the iron oxide nanomaterials demand higher energies to induce the excitation of free electrons, which is associated with the higher free electron density [116]. However, the production of gold-iron oxide nanohybrids can be explored both to improve the PTT capacity of the nanomaterials and imprint a responsivity to magnetic fields that can enhance the tumor accumulation. Bai *et al* produced hollow gold nanospheres with iron oxide nanoparticles immobilized on its surface for mediating both the imaging and PTT of cervical cancer [117]. For that

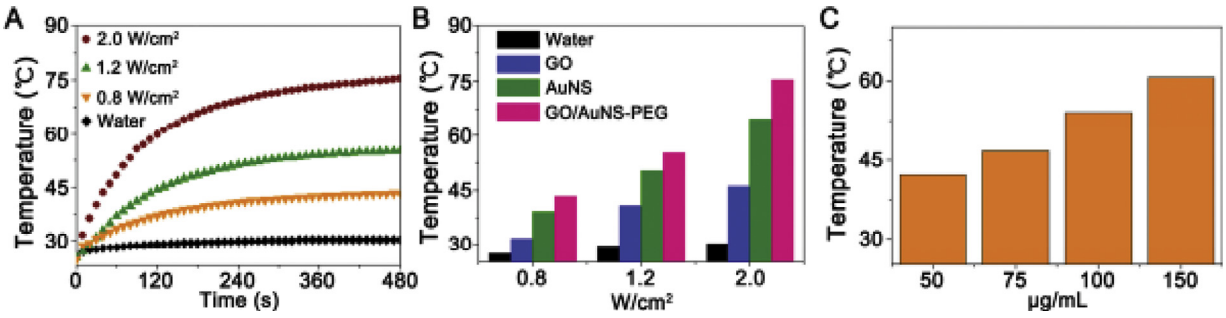

Fig. 5. Characterization of the GO/AuNS-PEG/Ce6 nanoparticles photothermal capacity. Temperature variation curves of GO/AuNS-PEG/Ce6 under the exposure to the 660 nm laser with different power densities, during 8 min (A); Maximum temperature reached by AuNS, GO, and GO/AuNS-PEG/Ce6 under the exposure to the 660 nm laser with different power densities (B); Maximum temperature registered for GO/AuNS-PEG/Ce6 nanoparticles at different concentrations under 660 nm laser radiation at 2.0 W.cm−2 for 8 min (C). Reprinted from Acta Biomaterialia, Vol 53, Wu, C., Li, D., Wang, L., Guan, X., Tian, Y., Yang, H., Li, S., and Liu, Y., Single wavelength light-mediated, synergistic bimodal cancer photoablation and amplified photothermal performance by graphene/gold nanostar/photosensitizer theranostics, Pages No.631-642, Copyright (2017), with permission from Elsevier.

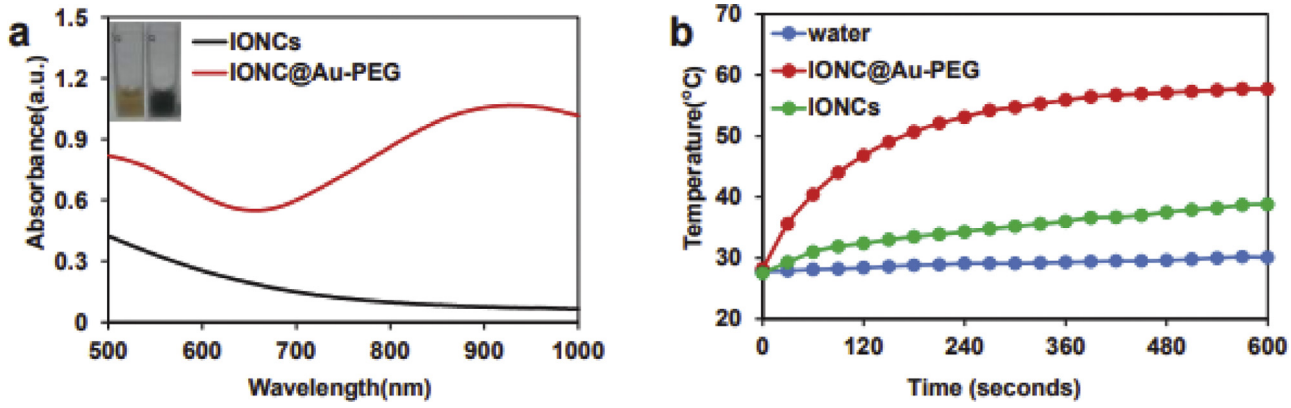

Fig. 6. Optical and photothermal characterization of PEGylated gold-iron oxide nanohybrids (IONC@Au-PEG). IONC@Au-PEG and IONCs UV-vis absorbance spectra (a); Temperature variation curves of IONCs, and IONC@Au-PEG nanoparticles under exposure to the 808 nm laser, 0.5 W.cm^{-2} for 10 min. Reprinted from Small, Vol 11, Liang, C., Song, X., Chen, Q., Liu, T., Song, G., Peng, R., and Liu, Z., Magnetic Field-Enhanced Photothermal Ablation of Tumor Sentinel Lymph Nodes to Inhibit Cancer Metastasis, Pages No.4856-4863, Copyright (2015), with permission from John Wiley & Sons.

purpose, dimercaptosuccinic acid-modified iron oxide nanoparticles were attached to the surface of the hollow gold nanospheres exploring the gold thiol-affinity. Additionally, this gold-iron oxide nanohybrid was functionalized with polyvinylpyrrolidone and folic acid (FA) to confer stability and targeting capacity, respectively. The authors observed that the introduction of iron oxide nanoparticles results in a red-shift in the hollow gold nanospheres LSPR peak, from 800 to 830 nm. Further, these gold-iron oxide nanohybrids were able to induce a temperature increase up to 63.4°C, whereas a gold nanorod (AR: 3.5) control group only reached 56.3°C. Liang and co-workers developed a PEGylated iron oxide-core gold shell nanohybrids for the PTT treatment of breast cancer [118]. For that purpose, poly(acrylic acid)-coated iron oxide nanoparticles were stabilized with poly(allylamine hydrochloride) and then mixed with small gold nanoseeds. Subsequently, the seeds were grown to a gold nanoshell by promoting the reduction of gold salt ($HAuCl_4$) and modified with lipoic-acid-terminated PEG via gold-thiol linkages. The authors observed that the gold-iron oxide nanohybrids presented a significant enhancement of the absorbance in the NIR region of the spectra, 0.88 vs 0.1 of iron oxide nanoparticles. Accordingly, the nanohybrid materials induced a superior temperature increase upon irradiation with NIR laser (808 nm, 0.5 W.cm^{-2}, for 10 min), 55°C and 39°C maximum temperature for the gold-iron oxide nanohybrids and iron oxide nanoparticles respectively (Fig. 6). Moreover, the authors also reported that the intratumoral injection of gold-iron oxide nanohybrids could mediate the temperature increase of breast tumors up to 52°C upon NIR laser irradiation (808 nm, 0.5 W.cm^{-2}, for 10 min) improving the mice survival.

3.2.4. Other gold-based nanohybrids

The development of more efficient photothermal agents can also be achieved by combining the gold nanostructures with organic materials. Nam and colleagues coated gold nanostars with PDA to mediate the DOX delivery and the PTT of colon carcinoma [119]. The authors observed that the gold nanostars functionalization with PDA induced a red-shift in the absorption spectra in a concentration-dependent manner. The absorption peak for gold-PDA hybrids shifted from ≈780 nm to 815, 840, and 860 nm for dopamine concentrations of 0.1, 0.2, and 0.3 mg.mL^{-1}, respectively. The authors also reported that the inclusion of PDA increases the photostability of the gold nanostars since no significant alterations in the relative absorbance at 808 nm were observed in the nanohybrid materials after irradiation with a NIR laser (808 nm, 10 W.cm^{-2}, for 30 min), whereas the gold nanostars presented a ≈70% reduction of the relative absorbance. Further, the gold nanohybrid materials mediated a temperature increase superior to 80°C after NIR laser irradiation (808 nm, 10 W.cm^{-2}, for 30 min) contrasting with 40°C obtained for the gold nanostars. The authors also demonstrated that the intratumoral injection of gold nanohybrid materials followed by NIR laser irradiation (808 nm, 1 W.cm^{-2}, for 5 min) could induce a 13°C increase in the temperature of CT26 tumors followed by tumor regression, with complete tumor eradication in 40% of the animals. Hu *et al* produced a PEGylated polypyr-

role (PPy)-gold nanohybrid to improve PPT of breast tumors [120]. For that purpose, PEI-PPy nanoparticles were produced using $FeCl_3$ as the oxidant to initiate the pyrrole monomer polymerization process. Then, these nanoparticles were PEGylated via carbodiimide chemistry (NH_2 groups of PEI and COOH terminated mPEG) and small gold spheres were grown in the interior of the PPy nanoparticles by promoting the *in situ* reduction of $HAuCl_4$. The authors revealed that the inclusion of the gold spheres enhanced the light-to-heat conversion efficiency from 35.3% to 37.1%. Accordingly, the PEGylated PPy-gold nanohybrids mediated a temperature increase to 55.6°C upon NIR laser irradiation (808 nm, 1.5 $W.cm^{-2}$, for 10 min), even after 5 cycles of irradiation, which contrasts with the 45.4°C obtained for the PPy nanoparticles. Further, the authors reported an enhancement of the 4T1 cancer cells PTT, the 4T1 cancer cells treated with the PPy-gold nanohybrids or PPy nanoparticles presented cell viability of 25.2% and 34.9%, respectively, after NIR irradiation.

Otherwise, the introduction of other metals in the gold nanomaterials can also result in an enhanced photothermal capacity. Leng *et al* reported a red-shift in the longitudinal LSPR peak of gold nanorods (aspect ratio 4.2) from 770 to 803 nm as well as an increase in the light-to-heat efficiency from 39% to 56% after the gold nanorods coating with a layer of copper sulfide [121]. Further, the authors also demonstrated that the gold-copper nanohybrids present increased photothermal stability, mediating the temperature increase up to 60°C even after four irradiation cycles (808 nm, 0.9 $W.cm^{-2}$, for 10 min) whereas the gold nanorods exhibited a 20% decrease in the temperature elevation (from 52.5°C to 47°C) after the irradiation cycles. Similar results were reported by Kumar and co-workers after the coating of gold bipyramids with molybdenum disulfide via electrostatic interactions [122]. The gold-molybdenum nanohybrids presented a red-shift in the longitudinal LSPR from 791 to 837 nm as well as an increase in the absorption maxima. Such improved the photothermal capacity of the gold bipyramids, registering a temperature increase up to 60.3°C, 50.6°C, and 55.6°C for the gold-molybdenum nanohybrids, molybdenum disulfide, and gold bipyramids, respectively, upon NIR laser irradiation (808 nm, 2 $W.cm^{-2}$, for 10 min). The authors also observed that the coating of gold bipyramids with molybdenum disulfide improved the PTT against HeLa cells. The NIR laser irradiation (808 nm, 2 $W.cm^{-2}$, for 3 cycles of 10 min) resulted in the decrease of HeLa cells' viability to 46.2% and 21.6% for the cells treated with gold bipyramids and gold-molybdenum nanohybrids, respectively.

3.3. Incorporation of small molecules with photothermal capacity

Among the different strategies explored to improve the cancer PTT mediated by the gold nanomaterials, the encapsulation of NIR responsive small molecules have been displaying promising results (Table 3). In this regard, indocyanine green (ICG) and heptamethine cyanines (*e.g.* IR780) are the most explored molecules to enhance the optical properties of gold nanostructures, and consequently its photothermal potential.

The ICG is a dye approved by the Food and Drug Administration for clinical fluorescence imaging, such as angiography [123]. Additionally, this molecule presents a high absorbance at 780 nm and a good light-to-heat conversion efficiency [124]. Further, ICG can also mediate the generation of ROS in response to NIR laser irradiation [125]. Higbee-Dempsey *et al* produced small gold nanoclusters consisting of 2 nm gold cores coated with dodecanethiol loaded with ICG to mediate the PTT and photoacoustic imaging of triple-negative breast cancer [126]. For that purpose, the authors explored the amphiphilic nature of ICG to drive the self-assembly of the hydrophobic 2 nm gold cores in spheroid nanostructures with ≈61 nm in diameter. The authors observed that the gold nanoclusters only present a slight red-shift in the LSPR absorption peak, whereas ICG loaded gold nanoclusters displayed a strong absorption in the 780 nm region, which is in agreement with the ICG absorption spectra. Additionally, the irradiation of the ICG-loaded gold nanoclusters with a NIR laser (808 nm, 1.2 $W.cm^{-2}$, for 10 min) was able to induce a temperature increase up to 70°C, whereas the free ICG solutions only reached the 45°C. Further, the authors noticed that the free ICG showed a rapid loss of its heating capacity with multiple laser irradiations (2-3 cycles), while the ICG-loaded gold clusters maintained its photothermal capacity. Such photothermal capacity was also confirmed in mice bearing 4T1 tumors after intravenous administration of ICG-loaded gold clusters induced the increase of tumors temperature up to 52.3°C after NIR laser irradiation (808 nm, 0.7 $W.cm^{-2}$ for 30 min) contrasting with the 45.6°C obtained in the free ICG treated group. Accordingly, the ICG-loaded gold clusters PTT induced the regression of the 4T1 tumors until day 11 with the complete remission of the primary tumor in two out of five mice. Otherwise, free ICG treatment only slowed tumor growth without any significant changes in mice survival. Chen and colleagues produced bovine serum albumin stabilized gold nanostars loaded with ICG to mediate the PTT of glioma [127]. The gold nanostars loading was achieved by promoting the ICG adsorption in the surface of the nanoparticles followed by the addition of bovine serum albumin. The produced gold nanostars presented an LSPR peak at 680 nm, which suffered a red-shift to 712 nm and also a pronounced absorption at 780 nm characteristic of ICG. The authors reported that the ICG-nanostars combination results in a more effective light-to-heat conversion efficiency and increased photostability, reaching the 63°C upon NIR laser irradiation (808 nm, 1 $W.cm^{-2}$ for 5 min). Otherwise, the free ICG and bovine serum albumin stabilized gold nanostars only reached 41°C and 59°C, respectively. Additionally, the authors also demonstrated that this photothermal capacity can be explored to mediate the photothermal ablation of U87 glioma cells, 85.1% and 94.2% of cell death for gold nanostars and ICG-loaded gold nanostar after NIR laser irradiation (808 nm, 1 $W.cm^{-2}$ for 5 min).

The heptamethine cyanines (*e.g.* IR780) in general present superior optical (*e.g.* higher molar extinction coefficient at 780 nm) and therapeutic capabilities, when compared to ICG [128]. Nevertheless, the application of these molecules in the clinic is hindered by its hydrophobic character, acute toxicity, and photodegradation, which can be surpassed by promoting the heptamethine cyanines encapsulation in nanoparticles such as gold nanomaterials [129]. Nagy-Simon *et al* prepared pluronic coated gold nanospheres loaded with IR780 for being applied in the colon carcinoma PTT [130]. The authors observed that apart from the characteristic LSPR peak of gold nanospheres at 522 nm, the IR780-pluronic coated gold nanospheres also presented a second absorption peak at 780 nm due to the IR780. Further, the IR780-pluronic coated gold nanospheres irradiation (785 nm, 170 mW for 6 min) induce a temperature increase of 9°C, whereas the free IR780 suffered photodegradation after 2.5 min of irradiation reaching a final temperature variation of ≈2°C. Similarly, Xia and co-workers developed IR780-loaded gold nanostars functionalized with bovine serum albumin and matrix metalloproteinases polypeptides (Ac-GPLGIAGQ) for the PTT and photodynamic therapy of lung cancer [131]. The IR780 loading was physically adsorbed onto the functionalized gold nanostars via hydrophobic interactions. The authors observed that the gold nanostars presented the LSPR peak in the 700-800 nm region and after the loading of IR780 the absorption in this region of the spectra increased being noticed the characteristic absorption peak at 780 nm (Fig. 7). Upon irradiation with a NIR laser (808 nm, 0.8 $W.cm^{-2}$, for 5 min), the IR780-loaded gold nanostars mediated the temperature increase to 63°C, whereas the gold nanostars alone only reached the 58.5°C. The authors confirmed the PTT potential on A549 tumor-bearing mice after the intravenous ad-

Please cite this article as: A.S.C. Gonçalves, C.F. Rodrigues and A.F. Moreira et al., Strategies to improve the photothermal capacity of gold-based nanomedicines, Acta Biomaterialia, https://doi.org/10.1016/j.actbio.2020.09.008

Table 3
Application of NIR responsive small molecules that have been explored to improve the photothermal capacity of gold-based nanomaterials (N.D. – non disclosed, N.A. – not applicable).

Small molecules	Gold Shape	Size	Surface Modification	LSPR peak (nm)	Photothermal Effect		Type of Study	Test Model	Main Results	Ref.
					Laser Parameters	Temperature				
ICG	NCL	mPEG-PLGA nanocapsules loaded with GNP and ICG	BSA, RGD peptides, and mPEG–PLGA, PVA, poly (acrylic acid)	700-850	808 nm, 1.0 W.cm^{-2}, 5 min	ΔT≈25°C	*In vitro*	U87-MG cells	The PTT effect mediated by the nanocapsules loaded with GNP and ICG induced the reduction of the viability of U87-MG cells to 35%.	[202]
	NCL	61.22 nm GNCL (GNP ≈2nm) coated with ICG	N.A.	803 nm	808 nm, 1.2 W, 7 min	≈60°C	*In vitro/In vivo*	4T1 cells/4T1 tumor-bearing mice	The ICG/GNCL mediated a ≈15°C increase in the temperature of 4T1 tumors, whereas the tumors treated with free ICG only presented a ΔT ≈ 5°C. Further, the ICG/GNCL treatment induced the reduction of the tumor volume until day 8 followed by the tumor re-growth until day 20.	[126]
	NCL	3.4 nm GNSP loaded with ICG molecules	Glutathione	≈700 and 800 nm	808 nm, 0.5 W.cm^{-2}, 5 min	ΔT≈20°C	*In vitro/In vivo*	MCF-7/MCF-7 tumor-bearing mice	The PTT effect mediated by the G/ICG nanostructures increased the temperature of the MCF-7 tumor to 55°C, whereas the free ICG only reached ≈40°C. Further, this combinatorial treatment resulted in the complete elimination of MCF-7 tumors in 14 days.	[203]
	NS	80 nm GNS (70 nm) with ICG adsorbed in the surface	BSA	712 and 780 nm	808 nm, 1.0 W.cm^{-2}, 0-6 min	63.9°C	*In vitro*	U87 cells	The PTT effect of GNS reduced the U87 cell viability to 15%, which combined with the ICG reached 5% of cell viability.	[127]
	NS	GNS (96 nm) loaded with ICG	$CaCO_3$	800-900 nm	808 nm, 1.0 W.cm^{-2}, 6 min	≈60°C	*In vitro/In vivo*	MGC803 cells/MGC80 tumor bearing mice	The PTT effect mediated by the G/ICG nanomaterials induced the increase of the MGC80 tumors' temperature to ≈43°C, which mediated the reduction of the tumor volume during 20 days.	[204]
	NCL	ICG loaded GNCL	BSA and HA	700 nm	808 nm, 1.5 W.cm^{-2}, 2 min	N.D.	*In vitro/In vivo*	4T1 cells/4T1 tumor-bearing mice	The PTT effect of the G/ICG nanostructures promoted a 15°C increase in the temperature of the 4T1 tumor, which induced the decrease of the tumor volume during 10 days followed by the tumor re-growth until day 12. Otherwise, the single treatment with free ICG or GNCL only slowed the growth of 4T1 tumors.	[205]
	NSH	151.1 nm hollow GNSH (125.3 nm) loaded with ICG	Gadolinium and BSA	Broad absorbance from 700 to 900 nm	808 nm, 1.5 W.cm^{-2}, 5 min	≈60°C	*In vitro/In vivo*	4T1 cells/4T1 tumor-bearing mice	The 4T1 tumors treated with G/ICG nanostructures registered a temperature increase up to ≈57°C, whereas the administration of free ICG or GNSH only reached ≈48°C. This photothermal improvement resulted in a decrease in the 4T1 tumors' volume during 21 days.	[206]
	NR	Nanosctrure with ≈ 103 nm comprised of MoS2 coated with GNR (L:50 nm, width:14 nm, A.R.: 3.5) and ICG	PEG	788 nm	808 nm, 0.2 W.cm-2, 5 min	57°C	*In vitro/In vivo*	HeLa cells/HeLa tumor-bearing mice	The GNR/MoS2/ICG nanohybrid led to higher tumor weight reduction followed by GNR/ MoS2, free ICG, GNR, and MoS2 alone.	[201]

(*continued on next page*)

Table 3 (*continued*)

Small molecules	Gold Shape	Size	Surface Modification	LSPR peak (nm)	Photothermal Effect		Type of Study	Test Model	Main Results	Ref.
					Laser Parameters	Temperature				
	NR	ICG loaded silica (shell: 17.34–32.43-nm) coated GNR (L: 47.23 nm, W: 13.56 nm, A.R: 3.50)	Mesoporous silica, tLyp-1 peptide and PEG	754 nm	785 nm, 3 $W.cm^{-2}$, 5 min	≈60°C	*In vitro*	MDA-MB-231 cells	The PTT effect mediated by the G/ICG nanostructures provoked the reduction of the viability of MDA-MB-231 cells to values inferior to 20%.	[201]
	NR	ICG loaded silica (shell: 21 nm) coated GNR (L: 57.3; W: 16.2; A.R: 3.47)	β-CD, RLA-Ada and (DMA CS(DMA)-PEG	813 nm	808 nm, 2 $W.cm^{-2}$, 5 min	≈60°C	*In vitro/In vivo*	MCF-7 cells/MCF-7 tumor bearing mice	The MCF-7 tumors treated with G/ICG nanostructures registered a temperature increase up to ≈45°C, whereas the administration of free ICG only reached ≈38°C. This photothermal improvement resulted in a decrease in the volume of MCF-7 tumors during 21 days, whereas the free ICG only slowed the tumor growth.	[207]
	NCL	31.97 nm ICG loaded GNCL (3.57 nm spheres)	BSA	760 nm	808 nm, 0.8 $W.cm^{-2}$, 4 min	≈60°C	*In vitro/In vivo*	4T1 cells/4T1 tumor-bearing mice	The PTT effect mediated by the G/ICG nanostructures increased the temperature of the 4T1 tumor to 53°C, whereas the free ICG only reached ≈46°C. Further, this combinatorial treatment resulted in the complete elimination of 4T1 tumors in 24 days without recurrence, whereas the free ICG only slowed the tumor growth.	[208]
IR780	NS	121.5 nm IR780-loaded GNS (80 nm)	BSA and metalloproteinases (MMP2) polypeptides	Broad absorbance from 600 to 1000 nm	808 nm, 0.8 $W.cm^{-2}$, 2 min	≈60°C	In vitro/In vivo	A549 cells/A549 tumor bearing mice	The A549 tumors treated with G/IR780 nanostructures registered a temperature increase up to ≈46°C, whereas the administration of free ICG only reached ≈41°C. This photothermal improvement resulted in a decrease in the A549 tumors' volume during 18 days, whereas the free ICG only slowed the tumor growth.	[131]
	NSP	30 nm GNSP loaded with IR780	Pluronic F127	522 and 780 nm	785 nm, 170 mW, 30 min	ΔT≈9°C	*In vitro*	C26 cells	The combinatorial treatment mediated by the G/IR780 nanostructures presented a higher number of C26 dead cells than the treatment with free ICG.	[130]
	NPR	IR780 loaded on GNP surface (57.5 nm)	Lyp-1 and PEG	600-700 nm	660 nm, 1 $W.cm^{-2}$, 5 min	≈50°C	In vitro/In vivo	MDA-MB-231 cells/MDA-MB-231 tumor bearing mice	The MDA-MB-231 tumors treated with gold-IR nanostructures registered a temperature increase up to ≈50°C mediating the decrease of the tumor volume with the complete tumor ablation in 2 of the 5 animals.	[209]
CyPT	NR	L: 48.5; W: 10.7 CyPT coated GNR	Glutathione	843 nm	808 nm; 1.5 $W.cm^{-2}$, 5 min	≈50°C	*In vitro/In vivo*	A549 cells/A549 tumor bearing mice	The PTT effect mediated by the G/CyPT nanostructures increased the temperature of the A549 tumor to 60°C promoting the complete tumor ablation in 16 days.	[210]

Abbreviations: NSH-Nanoshell; NCL-Nanocluster; NR-Nanorod; NC-Nanocage; NS-Nanostar; GNSH-Gold nanoshell; GNCL-Gold nanocluster; GNR-Gold nanorod; GNC-Gold nanocage; GNS-Gold Nanostar; NPs-nanoparticles; GNPs-Gold nanoparticles; G/ICG-Gold-ICG; G/IR780-Gold-IR780; and G/CyPT-Gold-Heptamethine cyanine dye.

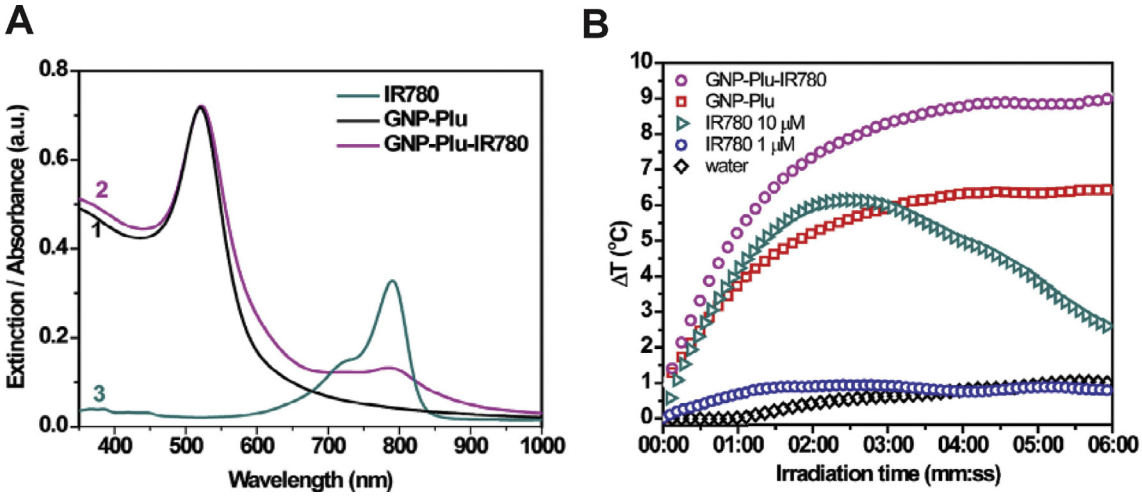

Fig. 7. Optical and photothermal characterization of GNP-Plu and GNP-Plu-IR780 nanoparticles. UV–Vis absorbance of GNP-Plu (1), GNP-Plu-IR780 (2), and IR780 (3) (A); Temperature variation curves of GNP-Plu-IR780, GNP-Plu, and free IR780 at different concentrations under the exposure of the 785 nm laser at 170 mW for 6 min (B). Adapted from Journal of Colloid and Interface Science, Vol 517, Nagy-Simon, T., Potara, M., Craciun, A., Licarete, E., Astilean, S., IR780-dye loaded gold nanoparticles as new near infrared activatable nanotheranostic agents for simultaneous photodynamic and photothermal therapy and intracellular tracking by surface enhanced resonant Raman scattering imaging, Pages No.239-250, Copyright (2018), with permission from Elsevier.

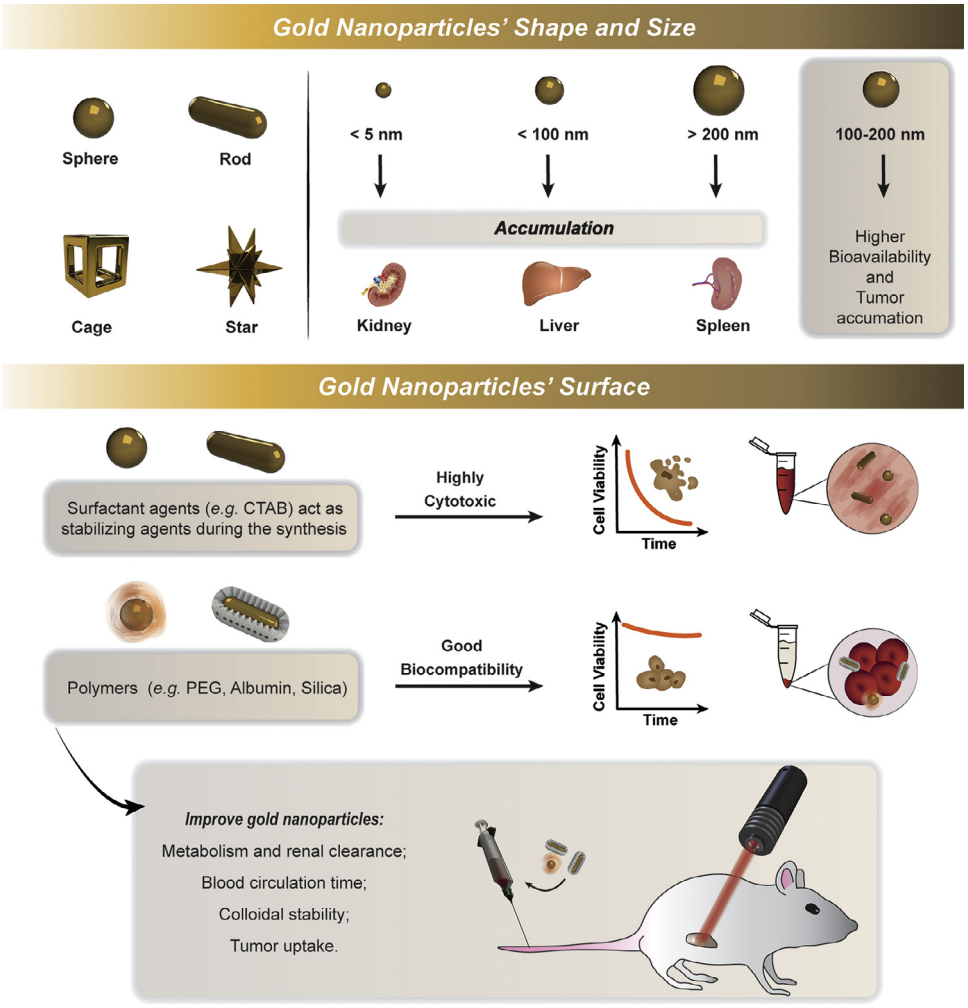

Fig. 8. Representation of the main factors that affect the biocompatibility and safety of gold nanoparticles.

Table 4
Overview of the gold nanoparticles and gold nanohybrids' biocompatibility (N.D. – non disclosed, N.A. – not applicable).

Nanomaterial	Gold Shape	Surface Modification	Biodistribution	Elimination Time	Circulation Time	Maximum Dose Administered	Ref.
Gold	NSP	Polysarcosine	PEGylated and polysarcosine GNPs were mainly accumulated in the liver (≈30% ID), whereas the polysarcosine GNPs presented superior retention in the kidneys. No significant damage was detected in major organs.	The amount of polysarcosine NPs in the kidney gradually decreased along the time, which indicates that these NPs were cleared through the urine.	10% of injected PEGylated GNPs and 20% of the injected polysarcosine GNPs remained in blood circulation after 24 h.	200 μg	[143]
		Cysteine-functionalized alginate-derived polymers	N.D.	Most of the NPs were eliminated after 11 days.	≈ one week	200 μL with 1 mg	[144]
	NSL	Chitosan and anti-EGFR antibody	Predominant accumulation of NPs in the tumor tissue. The amount of Au element in the tumor was over 6.28% ID/g 6h after the injection of NPs, which was superior to that found in other organs or blood.	After 24h, the amount of the NPs decreased in most of the organs, which suggests they were effectively eliminated.	After 24h, a residual NPs amount was present (≈1% ID/g).	175 μg/mL	[141]
		Betulinic acid (BA) liposomes	No significant damage and inflammatory reactions were detected in the major organs.	N.D.	N.D.	200 μL, containing 1.4 mg/kg BA and 94.9 μg/mL Au	[211]
		Macrophage cell membranes	Predominant accumulation in liver, spleen, and tumor after 48 hours. Cell membrane coated NS presented lower liver and spleen accumulation than bare NSs. Moreover, the Au content in the tumor was 7.48% ID/g after NS coating, and bare GNS only presented 1.61% ID/g. No significant damage was detected in the major organs.	After 48h, only 30% of membrane coated NSs were found in the blood, whereas the bare NSs were almost eliminated from the blood after 24h.	During the 48h, the coated NSs exhibited a significant increase in blood retention time, compared with bare GNS.	150 μL, 3 mg/mL	[212]
		DOTA, biofunctional PEG2K and PEG5k	High accumulation in the liver and spleen. The PEGylation enhanced NPs tumor uptake from 0.15 to 0.77% ID/g.	PEGylation increased renal clearance (25.8 to 33.7% ID/organ).	PEGylation increased the blood circulation half-life from 0.54 to 12.76 h.	N.D.	[146]
		PEGylated SN-38-micelles	No damages were detected in the major organs.	N.D.	N.D.	75 ug of gold per mouse	[152]
	NCL	Hybrid albumin	The liver, kidney, heart, lung, and spleen did not reveal significant damages.	N.D.	N.D.	200 μL at 10 mg/mL	[72]
		Captoril	No significant damages and inflammatory reactions were detected in the major organs.	N.D.	N.D.	100 mL at 2.5 mg/mL	[64]
		BSA or GSH	The BSA-Au25 NCLs were mainly accumulated in the spleen, and the GSH-Au25 presented low concentration in all organs. After 24h both formulations induced immune responses and affected the kidney function. After 28 days, the alterations observed in the GSH-Au25 NCLs were restored, whereas inflammatory reactions and damages in the liver and kidney were still observed in BSA-Au25 NCLs.	After 24h, 36% of GSH-Au25 and 1% of BSA-Au25 NCLs were excreted by the urine, respectively. After 28 days 94% of Au in the GSH-Au25 and 5% BSA-Au25 NCLs can be metabolized by renal clearance, respectively.	N.D.	7.55 mg/kg	[142]
	NR	PEG and Rabies virus glycoprotein	NPs are mainly accumulated in brain tissues with some significant fractions present in the kidney and liver. No significant damages were detected in the major organs.	N.D.	N.D.	200 μL at 2.5×10^{-3} M	[213]

(*continued on next page*)

Table 4 (*continued*)

Nanomaterial	Gold Shape	Surface Modification	Biodistribution	Elimination Time	Circulation Time	Maximum Dose Administered	Ref.
		Pluronic F 68 and chitosan	NPs are predominantly accumulated in the liver and tumor. Particularly, chitosan modified GNRs present higher tumor accumulation (20%) than PEGylated GNRs (7%).	N.D.	Up to 72 hours	100 μg	[214]
		BSA	At 24h after injection, Au concentrations of the small BSA NRs 4.54, 2.57, and 2.14 μg/g accumulated in the liver, spleen, and kidney, respectively. In the case of larger NRs, 3.66, 2.65, and 1.89 μg/g are accumulated in the liver, kidney, and lung, respectively. After 30 days the Au concentration of small NPs in these organs has a huge decrease, whereas Au of larger NPs is still present in higher concentrations. Moreover, CTAB coated NRs present lower cell biocompatibility compared with BSA coated NRs.	Small BSA GNRs present a better clearance and lower Au concentration in all organs at day 30, than larger BSA GNRs. More than 99% of the small BSA NRs can be eliminated after 30 days.	30 days	5 mg [Au]/kg	[215]
		PEG	At 24h after injection, 8.6% ID/g of the NPs accumulated in the tumor, 25.1% ID/g in the spleen, and 13.9% ID/g in the liver. No significant damage and inflammatory responses were detected in the major organs.	N.D.	PEGylated NPs present a blood circulation half-life of 9.2±0.6 h, whereas uncoated NPs only present 1.8±0.3 h.	150 μL at 2 mg/mL	[145]
	NC	PEI, FA, and PEG	Higher NPs accumulation in the tumor tissue, followed by the liver and spleen. No significant damage and inflammatory responses were detected in the major organs.	N.D.	N.D.	8.5 mg/kg	[163]
		HA, PEG, and A54 peptide	No significant damages and inflammatory responses were detected in the major organs.	N.D.	N.D.	32.6 mg/kg	[216]
		Manganese dioxide and PEG	After 3h, the Au and Mn levels increased in tumor and major organs. However, after 21 days the values in major organs were vestigial. No obvious damages or inflammatory responses were detected.	21 days	The first (t1/2(α)) and second (t1/2(β)) phases of circulation half-lives were 0.91 h and 19.07 h, respectively.	2 mg/Kg	[217]
		DOTA and PEG	55 nm GNCs presented a superior accumulation in the liver and spleen (60% ID/g in both organs at 1h post-injection) than the 30 nm GNCs. The 30 nm GNCs presented an enhanced in vivo pharmacokinetics.	N.D.	The blood retention of the 30 nm GNCs was 6 times superior to that of 55 nm GNCs at 1 h post-injection.	2.38 fmol in 100 μL	[218]
		H22 cancer cells membrane	Nanoformulations had a prominent accumulation in the liver, spleen, and lung, which reached the higher values for the uncoated GNCs. The modified GNCs presented a superior tumor accumulation, about 2 times superior to uncoated NCs. Moreover, the inclusion of cell membranes reduced the inflammatory response induced by GNCs.	Elimination half-life (t1/2β) of modified NCs was about 1.8-fold superior to that recorded for uncoated GNCs.	N.D.	10 mg/Kg	[219]

(*continued on next page*)

Table 4 (*continued*)

Nanomaterial	Gold Shape	Surface Modification	Biodistribution	Elimination Time	Circulation Time	Maximum Dose Administered	Ref.
		Acylsulfonamide	Predominant accumulation of the NPs in the spleen and liver (15% and 20%, respectively) and ≈10% in the tumor tissue. However, comparing with PVP GNSs, the acylsulfonamide coated GNSs presented lower accumulation in major organs and higher tumor accumulation. No significant damages and inflammatory responses were detected.	N.D.	Circulation half-life of acylsulfonamide GNSs was > 4-fold longer than PVP NCLs.	100 μL at 2.5 mg/mL	[220]
	NS	N.A.	After 48h NPs injection, 30 nm NSs present higher tumor uptake than 60 nm NSs, 2.11%, and 0.88% respectively. NSs with 60 nm presented higher accumulation in the liver (≈19%) and spleen. No significant damages and inflammatory reactions were detected in the major organs.	N.D.	30 nm and 60 nm GNSs had a half-life of 33 and 27 h, respectively.	200 μg	[221]
		Erythrocyte membranes	NPs accumulated quickly and in large amounts in the liver.	At 72h NPs were not completely metabolized, being the kidney the main via for its removal.	up to 72 h	200 μL at 2 mg/mL	[222]
		Aptamer AS1411	Predominant accumulation in the liver (50% ID/g) followed by spleen (21%ID/g) at 24 h. Accumulation of aptamer NPs was 5 times higher in breast cancer tumors than fibrosarcoma tumors. Moreover, the accumulation in de tumor increased along the time (2% ID/g and 9.7% ID/g for 24 and 72h, respectively).	N.D.	For at least 2 days	4.8 mg/Kg	[223]
G/S	NS	PEG	High uptake from liver, spleen, and lung. The Au uptake in the tumor was 39 µg/g, being significantly higher than in the control group.	N.D.	N.D.	50 μL at 32 mM	[224]
	NR	β-cyclodextrin, and RLA peptide	No significant damages were detected in the major organs.	N.D.	N.D.	20 mg/Kg	[207]
	NR	β-cyclodextrin, lactobionic acid, and PEG	At 24h after injection, 50% and 30% of NPs were accumulated in tumor and liver, respectively. A few amounts were present in the kidney, spleen, and heart. No significant damage and inflammatory responses were detected in the major organs.	N.D.	N.D.	1.15 mg/kg	[225]
	NS	PEG	After 0.5 h NPs accumulated in the tumor. After 24h, ≈20%, ≈15%, and ≈2.5% of the NPs accumulated in the spleen, liver, and in the tumor, respectively. No significant damage and inflammatory responses were detected in the major organs.	N.D.	N.D.	100 mL at 4 mg/mL	[226]
G/GO	NSP	Chitosan, protoporphyrin IX and FA	Specific targeting and high fluorescence in the tumor tissues. Heart and brain presented minimal accumulation, while the other organs such as the liver and kidney presented a reduction in NPs' accumulation over time.	Urine is the main excretion route for the G/GO NPs.	SERS spectral analysis demonstrated a reduction of the amount of NPs in the blood over time.	200 μg/mL	[177]

(*continued on next page*)

Table 4 (*continued*)

Nanomaterial	Gold Shape	Surface Modification	Biodistribution	Elimination Time	Circulation Time	Maximum Dose Administered	Ref.
	NR	PEG, Tat protein vector, and Cy7	After 1h, the NPs were mainly accumulated in the liver, spleen, and kidney. After 20h, the amount of NPs in major organs decreased and increases in the tumor tissues.	After 20h, the amount of NPs in the major organs decreased to almost undetectable values. Moreover, the results demonstrated that NPs were cleared from the body through the intestine and bladder.	N.D.	150 μL of 1 mg/mL	[111]
	NSP	α-synuclein protein, tumor-tropic mesenchymal stem cell (MSC)	After 3 days, NPs had a predominant accumulation in liver and spleen. The MSC-AuNP/GO sheet 1 $\times$ formulation presented the highest Au accumulation (41.1 μg Au/g) in the tumor tissue, being 3.6 and 4.5-fold higher than the MSC-AuNP/GO sheet 0.25 $\times$ and MSC-AuNP 1 $\times$, respectively. No damage was detected in major organs.	N.D.	N.D.	716.5 μg of AuNPs per mouse in the MSC-AuNP/GO sheet formulation, and 212.6 μg in remain NPs formulations.	[183]
G/IO	NSP	Black phosphorus sheets	Predominant accumulation in spleen, liver, and lung. No obvious damages or inflammatory responses were detected in major organs.	The biodistribution of Au in major organs reduced over time (10 min to 10 days)	N.D.	100μl at 1 mg /mL	[187]
	NF	G5 poly(amidoamine) (PAMAM) dendrimers	NPs accumulated preferentially in the liver, spleen, and tumor. After 1h, the Au concentration in the liver, spleen, and the tumor was 230.0 µg g^{-1}, 209.2 µg g^{-1}, and 38.6 µg g^{-1}, respectively.	Au concentration in major organs decreased over time, being almost cleared out after 96h.	N.D.	200 μl at 0.04 mM [Au]	[189]
G/Cu	NSP and NR	N.A.	High accumulation in liver, spleen, and kidney with a decrease over time. High levels of creatinine were observed on day 1 however, decreased to normal levels in day 7. No damages or inflammatory reactions were observed in the main organs.	Almost cleared after 60 days.	N.D.	200 μL at 2 mg/mL	[200]
G/PDA	NSP	N.A.	NPs accumulated predominantly in the liver (≈40% ID, mainly in Kupffer cells) spleen (≈13% ID, mainly in macrophages), and these values remain identical in day 1 and 42. No notable histological damages were detected in major organs.	NPs clearance from the blood was fast. However, 6 weeks after injection no significant alterations in the biodistribution of NPs were observed, which demonstrated that the NPs were difficult to eliminate.	NPs were rapidly eliminated from the blood, only ≈15% of injected NPs remained in the blood at 5 min after injection. The NPs' half decay time was (t1/2) ≈4.9 ±1.1 h.	20 mg/L	[227]
	NSP	Silica and perfluorohexane	Predominant accumulation in the lung, liver, and spleen. After 1h, the lung and tumor had the highest Au uptake, 1000 ug/g and ≈<50ug/g, respectively. No significant morphological changes, inflammatory reactions, and necrosis were detected.	After injection, NPs were gradually metabolized from the tumor and main organs.	N.D.	8 mg/mL	[228]
	NB	N.A.	NPs accumulate predominantly in the liver (≈23 % ID/g), spleen (≈17 % ID/g), and the tumor (≈5 % ID/g). No significant damages were detected in the major organs.	N.D.	N.D.	100μL at 200 μg/mL	[229]
G/PPy	NSP	Aptamer S2.2	No significant damage and inflammatory reactions were detected in the major organs.	N.D.	N.D.	1 mg/mL	[198]

Abbreviations: NSH-Nanoshell; NCL-Nanocluster; NR-Nanorod; NC-Nanocage; NS-Nanostar; NF-Nanoflower; NB-Nanobipyramid; GNSH-Gold nanoshell; GNCL-Gold nanocluster; GNR-Gold nanorod; GNC-Gold nanocage; GNS-Gold Nanostar; NPs-nanoparticles; G/NPs-Gold nanoparticles; G/S-Gold/Silica nanohybrid; G/GO-Gold/Graphene Oxide nanohybrid; G/IO-Gold/Iron Oxide nanohybrid; G/PPY-Gold/Polypyrrole nanohybrid; G/PDA-Gold/Polydopamine nanohybrid and G/Cu-Gold/Copper nanohybrid.

ministration of functionalized with bovine serum albumin and Ac-GPLGIAGQ, observing the increase in the tumor tissue temperature to 46°C after NIR laser irradiation (808 nm, 0.8 W.cm^{-2}, for 5 min), which resulted in the reduction of the tumor volume during 18 days.

4. Biocompatibility of gold-based nanomaterials

The wide application of gold-based nanomaterials in biomedical applications raises some human safety concerns, which highlights the necessity to better understand their interaction with the human body. In this regard, several studies still are being performed to evaluate the biodistribution and circulation of gold nanoparticles in the bloodstream, their pharmacokinetics and elimination from the organism, as well as any possible toxicity, *i.e.* adverse side effects to the organism as a whole or at the cellular and genomic level (Table 4). It is worth to notice that several parameters affect the interaction of gold nanomaterials with the human body, such as size, shape, charge, and surface chemistry (reviewed in detail by [132-135] (Fig. 8). In a typical synthesis of gold nanorods and other gold-based nanomaterials, the highly cytotoxic CTAB molecules are used as a stabilizing agent impacting its applicability in humans [136]. Therefore, the biocompatibility of these gold nanomaterials is ensured by replacing the CTAB molecules with non-toxic materials such as PEG [137], chitosan [138], albumin [139], silica [140]. Manivasagan and colleagues reported that the silica-core gold shells functionalized with chitosan and lipoic acid where biocompatible at concentrations up to 250 μg.mL^{-1} (i.e. cell viabilities superior to 95%), whereas a notorious decrease in the viability of MDA-MB-231 cells was observed at concentrations superior to 150 μg.mL^{-1} [141]. Zhang et al evaluated the toxicity responses of mice subjected to the intraperitoneal injection of Albumin or GSH coated gold nanoclusters at a concentration up to 7.55 mg.kg^{-1} [142]. The obtained results revealed that after 24 hours no significant statistical differences were observed in the bodyweight of the mice as well as no pathological lesions in major organs were detected. Nevertheless, the authors demonstrated that after 24 hours the high dose of gold nanoclusters induces acute immune responses (*i.e.* thymus index values increased from 2.3 to 4.2 in the treated groups), increases the blood levels of white blood cells and creatine as well as affects the kidney functions. Interestingly, these toxicity responses were almost completely reverted in the GSH coated gold nanoclusters after 28 days, which was attributed to the faster metabolism and renal clearance of this nanomaterial. Otherwise, the surface passivation of the gold nanomaterials can also enhance its colloidal stability and increase the blood circulation time [143,144]. Xu and coworkers observed that the PEGylation of gold-core silica shell nanorods increased the blood circulation half-life from 1.8 to 9.2 hours [145]. Similarly, Xie et al reported that the PEGylation of gold nanoshells also increased the blood circulation half-life from 0.54 to 12.76 hours [146]. Further, the authors also observed that increasing the blood circulation half-life resulted in an enhanced tumor uptake from 0.15 to 0.77 %ID/g.

5. Conclusion

Gold nanomaterials exhibit desirable physicochemical, electronic, and optical properties for potential applications in the clinic such as in cancer diagnosis and/or treatment. In particular, the capacity of gold-based nanomaterials to mediate the cancer hyperthermia in response to irradiation with a NIR light has demonstrated promising results even in clinical trials (*e.g.* Aurolase®, ClinicalTrials.gov Identifier: NCT01679470 and NCT00848042). However, until now the clinical translation of gold-based photothermal agents has not been accomplished. Such can be in part justified by the limitations of the NIR radiation penetration in the human body, which restrains the application of the photothermal agents to more superficial tumors such as melanoma, oral cancer, and breast cancer. Further, some gold-based nanomaterials present sub-optimal light-to-heat conversion efficiencies that decrease its therapeutic efficiency. Therefore, the optimization of the photothermal effect is paramount to enhance the antitumoral efficacy of the nanomaterials. Therefore, several strategies have been explored to maximize the photothermal effect mediated by the gold-based nanomaterials, which vary from modifications of the laser light parameters that can affect the excitation of the nanomaterials to the optimization of the size, structure, and organization. The determination of the optimal laser wavelength and power density as well as the number of irradiations and duration are essential for the successful activation of the gold nanomaterials and consequent heat generation. Further, in the future, the development/validation of NIR laser devices such as fiber optic coupled NIR lasers will facilitate the application of these light-responsive nanomaterials in deep-seated tumors.

Otherwise, the gold nanostructures size, morphology, and structure organization can be optimized to fine-tune the LSPR peak to the NIR region and increase its absorption maxima. Further, the gold-based nanoparticles can also be combined with different materials (*e.g.* silica, graphene, and PDA) that can enhance the gold optical properties and photostability or even act simultaneously as an additional photothermal agent, which ultimately increases the amount of heat generated by the gold nanohybrids. Similarly, the gold nanoparticles can be loaded with small photothermal molecules increasing the effectiveness of the cancer PTT.

Finally, considering the pharmacokinetic aspects (absorption, distribution, metabolism, and excretion) of the nanoparticles, in general, only ≈0.7% of the administered dose reaches the tumor tissue, the combination of the gold nanomaterials PTT optimization with surface modifications that improve the circulation time, target-specific accumulation, and clearance from the body will be crucial to minimize the dosage necessary to ablate the tumor tissue and prevent unwanted side effects.

Declaration of Competing Interest

The authors declare no financial or commercial conflict of interest.

Acknowledgments

This work was supported by FEDER funds through the POCI – COMPETE 2020 – Operational Programme Competitiveness and Internationalisation in Axis I – Strengthening research, technological development, and innovation (Project POCI-01 0145-FEDER-007491) and National Funds by FCT – Foundation for Science and Technology (Project UID/Multi/00709/2013). The funding from CENTRO-01-0145-FEDER-028989 and POCI-01-0145-FEDER-031462 are also acknowledged. Carolina F. Rodrigues acknowledge for her Ph.D. fellowship from FCT (SFRH/BD/144680/2019). The funders had no role in the decision to publish or in the preparation of the manuscript.

References

[1] E. Mei, S. Li, J. Song, R. Xing, Z. Li, X. Yan, Self-assembling Collagen/Alginate hybrid hydrogels for combinatorial photothermal and immuno tumor therapy, Colloids Surf., A 577 (2019) 570–575.
[2] G.S. Terentyuk, G.N. Maslyakova, L.V. Suleymanova, N.G. Khlebtsov, B.N. Khlebtsov, G.G. Akchurin, I.L. Maksimova, V.V. Tuchin, Laser-induced tissue hyperthermia mediated by gold nanoparticles: toward cancer phototherapy, J. Biomed. Opt. 14 (2) (2009) 021016.
[3] M.R.K. Ali, Y. Wu, Y. Tang, H. Xiao, K. Chen, T. Han, N. Fang, R. Wu, M.A. El-Sayed, Targeting cancer cell integrins using gold nanorods in photothermal therapy inhibits migration through affecting cytoskeletal proteins, Proc. Natl. Acad. Sci. U. S. A. 114 (28) (2017) E5655–E5663.

[4] N. Cihoric, A. Tsikkinis, G. van Rhoon, H. Crezee, D.M. Aebersold, S. Bodis, M. Beck, J. Nadobny, V. Budach, P. Wust, Hyperthermia-related clinical trials on cancer treatment within the ClinicalTrials. gov registry, Int. J. Hyperther. 31 (6) (2015) 609–614.
[5] W. Fan, B. Yung, P. Huang, X. Chen, Nanotechnology for multimodal synergistic cancer therapy, Chem. Rev. 117 (22) (2017) 13566–13638.
[6] X. Huang, P.K. Jain, I.H. El-Sayed, M.A. El-Sayed, Gold nanoparticles: interesting optical properties and recent applications in cancer diagnostics and therapy, Nanomedicine (Lond) 2 (5) (2007) 681–693.
[7] H. Deng, Y. Zhong, M. Du, Q. Liu, Z. Fan, F. Dai, X. Zhang, Theranostic self--assembly structure of gold nanoparticles for NIR photothermal therapy and X-Ray computed tomography imaging, Theranostics 4 (9) (2014) 904.
[8] F. Zhou, X. Da, Z. Ou, B. Wu, D.E. Resasco, W.R. Chen, Cancer photothermal therapy in the near-infrared region by using single-walled carbon nanotubes, J. Biomed. Opt. 14 (2) (2009) 021009.
[9] D. de Melo-Diogo, E.C. Costa, C.G. Alves, R. Lima-Sousa, P. Ferreira, R.O. Louro, I.J. Correia, POxylated graphene oxide nanomaterials for combination chemo-phototherapy of breast cancer cells, Eur. J. Pharm. Biopharm. 131 (2018) 162–169.
[10] J. Zhou, Z. Lu, X. Zhu, X. Wang, Y. Liao, Z. Ma, F. Li, NIR photothermal therapy using polyaniline nanoparticles, Biomaterials 34 (37) (2013) 9584–9592.
[11] T.A. Jacinto, C.F. Rodrigues, A.F. Moreira, S.P. Miguel, E.C. Costa, P. Ferreira, I.J. Correia, Hyaluronic acid and Vitamin E polyethylene glycol succinate functionalized gold-core silica shell nanorods for cancer targeted photothermal therapy, Colloids Surf. B: Biointerfaces (2020) 110778.
[12] C.G. Alves, D. de Melo-Diogo, R. Lima-Sousa, E.C. Costa, I.J. Correia, Hyaluronic acid functionalized nanoparticles loaded with IR780 and DOX for cancer chemo-photothermal therapy, Eur. J. Pharm. Biopharm. 137 (2019) 86–94.
[13] N. An, H. Lin, F. Qu, Synthesis of a GNRs@ mSiO2-ICG-DOX@ Se-Se-FA nanocomposite for controlled chemo-/Photothermal/Photodynamic therapy, Eur. J. Inorg. Chem. 2018 (39) (2018) 4375–4384.
[14] M.-C. Daniel, D. Astruc, Gold nanoparticles: assembly, supramolecular chemistry, quantum-size-related properties, and applications toward biology, catalysis, and nanotechnology, Chem. Rev. 104 (1) (2004) 293–346.
[15] X. Yang, M. Yang, B. Pang, M. Vara, Y. Xia, Gold nanomaterials at work in biomedicine, Chem. Rev. 115 (19) (2015) 10410–10488.
[16] Z. Bao, X. Liu, Y. Liu, H. Liu, K. Zhao, Near-infrared light-responsive inorganic nanomaterials for photothermal therapy, Asian J. Pharm. Sci. 11 (3) (2016) 349–364.
[17] P.J. Debouttière, S. Roux, F. Vocanson, C. Billotey, O. Beuf, A. Favre-Réguillon, Y. Lin, S. Pellet-Rostaing, R. Lamartine, P. Perriat, Design of gold nanoparticles for magnetic resonance imaging, Adv. Funct. Mater. 16 (18) (2006) 2330–2339.
[18] Q.-Y. Cai, S.H. Kim, K.S. Choi, S.Y. Kim, S.J. Byun, K.W. Kim, S.H. Park, S.K. Juhng, K.-H. Yoon, Colloidal gold nanoparticles as a blood-pool contrast agent for X-ray computed tomography in mice, Invest. Radiol. 42 (12) (2007) 797–806.
[19] S. Narayanan, B.N. Sathy, U. Mony, M. Koyakutty, S.V. Nair, D. Menon, Biocompatible magnetite/gold nanohybrid contrast agents via green chemistry for MRI and CT bioimaging, ACS Appl. Mater. Interfaces 4 (1) (2012) 251–260.
[20] S. Jain, D. Hirst, J. O'sullivan, Gold nanoparticles as novel agents for cancer therapy, Br. J. Radiol. 85 (1010) (2012) 101–113.
[21] W. Li, X. Chen, Gold nanoparticles for photoacoustic imaging, Nanomedicine 10 (2) (2015) 299–320.
[22] H. Norouzi, K. Khoshgard, F. Akbarzadeh, In vitro outlook of gold nanoparticles in photo-thermal therapy: a literature review, Lasers Med. Sci. 33 (4) (2018) 917–926.
[23] Q. Lei, J.-J. Hu, L. Rong, H. Cheng, Y.-X. Sun, X.-Z. Zhang, Gold nanocluster decorated polypeptide/DNA complexes for NIR light and redox dual-responsive gene transfection, Molecules 21 (8) (2016) 1103.
[24] J.C. Love, L.A. Estroff, J.K. Kriebel, R.G. Nuzzo, G.M. Whitesides, Self-assembled monolayers of thiolates on metals as a form of nanotechnology, Chem. Rev. 105 (4) (2005) 1103–1170.
[25] J. Liu, Q. Peng, Protein-gold nanoparticle interactions and their possible impact on biomedical applications, Acta Biomater. 55 (2017) 13–27.
[26] S. Wilhelm, A.J. Tavares, Q. Dai, S. Ohta, J. Audet, H.F. Dvorak, W.C. Chan, Analysis of nanoparticle delivery to tumours, Nat. Rev. Mater. 1 (5) (2016) 16014.
[27] X. Huang, P.K. Jain, I.H. El-Sayed, M.A. El-Sayed, Gold nanoparticles: interesting optical properties and recent applications in cancer diagnostics and therapy, (2007).
[28] Y. Matsumoto, J.W. Nichols, K. Toh, T. Nomoto, H. Cabral, Y. Miura, R.J. Christie, N. Yamada, T. Ogura, M.R. Kano, Vascular bursts enhance permeability of tumour blood vessels and improve nanoparticle delivery, Nature Nanotechnol. 11 (6) (2016) 533.
[29] H. Maeda, H. Nakamura, J. Fang, The EPR effect for macromolecular drug delivery to solid tumors: improvement of tumor uptake, lowering of systemic toxicity, and distinct tumor imaging in vivo, Adv. Drug Deliv. Rev. 65 (1) (2013) 71–79.
[30] D. de Melo-Diogo, C. Pais-Silva, D.R. Dias, A.F. Moreira, I.J. Correia, Strategies to improve cancer photothermal therapy mediated by nanomaterials, Adv. Healthc. Mater. 6 (10) (2017) 1700073.
[31] K.N. Andrade, A.M.P. Pérez, G.G.C. Arízaga, Passive and active targeting strategies in hybrid layered double hydroxides nanoparticles for tumor bioimaging and therapy, Appl. Clay Sci. 181 (2019) 105214.
[32] B.-J.L. Van Hong, Nguyen, Protein corona: a new approach for nanomedicine design, Int. J. Nanomed. 12 (2017) 3137.
[33] S. Shen, S. Wang, R. Zheng, X. Zhu, X. Jiang, D. Fu, W. Yang, Magnetic nanoparticle clusters for photothermal therapy with near-infrared irradiation, Biomaterials 39 (2015) 67–74.
[34] C. Chen, S. Wang, L. Li, P. Wang, C. Chen, Z. Sun, T. Song, Bacterial magnetic nanoparticles for photothermal therapy of cancer under the guidance of MRI, Biomaterials 104 (2016) 352–360.
[35] S. Liang, C. Li, C. Zhang, Y. Chen, L. Xu, C. Bao, X. Wang, CD44v6 monoclonal antibody-conjugated gold nanostars for targeted photoacoustic imaging and plasmonic photothermal therapy of gastric cancer stem-like cells, Theranostics 5 (9) (2015) 970.
[36] H. Chen, L. Shao, T. Ming, Z. Sun, C. Zhao, B. Yang, J. Wang, Understanding the photothermal conversion efficiency of gold nanocrystals, Small 6 (20) (2010) 2272–2280.
[37] F. Yan, W. Duan, Y. Li, H. Wu, Y. Zhou, M. Pan, H. Liu, X. Liu, H. Zheng, NIR-laser-controlled drug release from DOX/IR-780-loaded temperature-sensitive-liposomes for chemo-photothermal synergistic tumor therapy, Theranostics 6 (13) (2016) 2337.
[38] M. Chu, Y. Shao, J. Peng, X. Dai, H. Li, Q. Wu, D. Shi, Near-infrared laser light mediated cancer therapy by photothermal effect of Fe3O4 magnetic nanoparticles, Biomaterials 34 (16) (2013) 4078–4088.
[39] K. Yang, H. Xu, L. Cheng, C. Sun, J. Wang, Z. Liu, In vitro and in vivo near-infrared photothermal therapy of cancer using polypyrrole organic nanoparticles, Adv. Mater. 24 (41) (2012) 5586–5592.
[40] P. Liang, Q. Tang, Y. Cai, G. Liu, W. Si, J. Shao, W. Huang, Q. Zhang, X. Dong, Self-quenched ferrocenyl diketopyrrolopyrrole organic nanoparticles with amplifying photothermal effect for cancer therapy, Chem. Sci. 8 (11) (2017) 7457–7463.
[41] X. Zhu, W. Feng, J. Chang, Y.-W. Tan, J. Li, M. Chen, Y. Sun, F. Li, Temperature-feedback upconversion nanocomposite for accurate photothermal therapy at facile temperature, Nat. Commun. 7 (2016) 10437.
[42] B. Zhang, H. Wang, S. Shen, X. She, W. Shi, J. Chen, Q. Zhang, Y. Hu, Z. Pang, X. Jiang, Fibrin-targeting peptide CREKA-conjugated multi-walled carbon nanotubes for self-amplified photothermal therapy of tumor, Biomaterials 79 (2016) 46–55.
[43] Z. Zhou, B. Kong, C. Yu, X. Shi, M. Wang, W. Liu, Y. Sun, Y. Zhang, H. Yang, S. Yang, Tungsten oxide nanorods: an efficient nanoplatform for tumor CT imaging and photothermal therapy, Sci. Rep. 4 (2014) 3653.
[44] C.F. Rodrigues, C.A. Reis, A.F. Moreira, P. Ferreira, I.J. Correia, Optimization of gold core-mesoporous silica shell functionalization with TPGS and PEI for cancer therapy, Micropor. Mesopor. Mat. 285 (2019) 1–12.
[45] D. Jaque, L.M. Maestro, B. Del Rosal, P. Haro-Gonzalez, A. Benayas, J. Plaza, E.M. Rodriguez, J.G. Sole, Nanoparticles for photothermal therapies, Nanoscale 6 (16) (2014) 9494–9530.
[46] V. Amendola, R. Pilot, M. Frasconi, O.M. Maragò, M.A. Iatì, Surface plasmon resonance in gold nanoparticles: a review, J. Phys.: Condensed Matter 29 (20) (2017) 203002.
[47] A.F. Moreira, C.F. Rodrigues, C.A. Reis, E.C. Costa, I.J. Correia, Gold-core silica shell nanoparticles application in imaging and therapy: a review, Micropor. Mesopor. Mat. 270 (2018) 168–179.
[48] P. Huang, J. Lin, W. Li, P. Rong, Z. Wang, S. Wang, X. Wang, X. Sun, M. Aronova, G. Niu, Biodegradable gold nanovesicles with an ultrastrong plasmonic coupling effect for photoacoustic imaging and photothermal therapy, Angew. Chem. 125 (52) (2013) 14208–14214.
[49] J. Lin, S. Wang, P. Huang, Z. Wang, S. Chen, G. Niu, W. Li, J. He, D. Cui, G. Lu, Photosensitizer-loaded gold vesicles with strong plasmonic coupling effect for imaging-guided photothermal/photodynamic therapy, ACS Nano 7 (6) (2013) 5320–5329.
[50] J. Song, P. Huang, X. Chen, Preparation of plasmonic vesicles from amphiphilic gold nanocrystals grafted with polymer brushes, Nat. Protoc. 11 (11) (2016) 2287–2299.
[51] P. Huang, O. Pandoli, X. Wang, Z. Wang, Z. Li, C. Zhang, F. Chen, J. Lin, D. Cui, X. Chen, Chiral guanosine 5′-monophosphate-capped gold nanoflowers: Controllable synthesis, characterization, surface-enhanced Raman scattering activity, cellular imaging and photothermal therapy, Nano Res. 5 (9) (2012) 630–639.
[52] P. Huang, P. Rong, J. Lin, W. Li, X. Yan, M.G. Zhang, L. Nie, G. Niu, J. Lu, W. Wang, Triphase interface synthesis of plasmonic gold bellflowers as near-infrared light mediated acoustic and thermal theranostics, J. Am. Chem. Soc. 136 (23) (2014) 8307–8313.
[53] J. Lin, M.G. Zhang, Y. Tang, B. Wen, H. Hu, J. Song, Y. Liu, P. Huang, X. Chen, Temporal-spatially transformed synthesis and formation mechanism of gold bellflowers, Nanoscale 8 (14) (2016) 7430–7434.
[54] C. Li, E. Mei, C. Chen, Y. Li, B. Nugasur, L. Hou, X. Ding, M. Hu, Y. Zhang, Z. Su, Gold-nanobipyramid-based nanotheranostics for dual-modality imaging-guided phototherapy, ACS Appl. Mater. Interfaces 12 (11) (2020) 12541–12548.
[55] M. Moros, A. Lewinska, F. Merola, P. Ferraro, M. Wnuk, A. Tino, C. Tortiglione, Gold nanorods and nanoprisms mediate different photothermal cell death mechanisms in vitro and in vivo, ACS Appl. Mater. Interfaces 12 (12) (2020) 13718–13730.
[56] G. Alfranca, Á. Artiga, G. Stepien, M. Moros, S.G. Mitchell, J.M. de la Fuente, Gold nanoprism–nanorod face off: comparing the heating efficiency, cellular internalization and thermoablation capacity, Nanomedicine 11 (22) (2016) 2903–2916.
[57] A. Ambrosone, P.d. Pino, V. Marchesano, W.J. Parak, J.M. de la Fuente,

Please cite this article as: A.S.C. Gonçalves, C.F. Rodrigues and A.F. Moreira et al., Strategies to improve the photothermal capacity of gold-based nanomedicines, Acta Biomaterialia, https://doi.org/10.1016/j.actbio.2020.09.008

C. Tortiglione, Gold nanoprisms for photothermal cell ablation in vivo, Nanomedicine 9 (13) (2014) 1913–1922.
[58] B. Liu, W. Cao, G. Qiao, S. Yao, S. Pan, L. Wang, C. Yue, L. Ma, Y. Liu, D. Cui, Effects of gold nanoprism-assisted human PD-L1 siRNA on both gene down-regulation and photothermal therapy on lung cancer, Acta Biomater. 99 (2019) 307–319.
[59] W. Zhang, X. Ding, H. Cheng, C. Yin, J. Yan, Z. Mou, W. Wang, D. Cui, C. Fan, D. Sun, Dual-targeted gold nanoprism for recognition of early apoptosis, dual-model imaging and precise cancer photothermal therapy, Theranostics 9 (19) (2019) 5610.
[60] C. Bao, J. Conde, F. Pan, C. Li, C. Zhang, F. Tian, S. Liang, M. Jesus, D. Cui, Gold nanoprisms as a hybrid in vivo cancer theranostic platform for in situ photoacoustic imaging, angiography, and localized hyperthermia, Nano Res. 9 (4) (2016) 1043–1056.
[61] C.D. De Souza, B.R. Nogueira, M.E.C. Rostelato, Review of the methodologies used in the synthesis gold nanoparticles by chemical reduction, J. Alloy. Compd. 798 (2019) 714–740.
[62] C.A. Reis, C.F. Rodrigues, A.F. Moreira, T.A. Jacinto, P. Ferreira, I.J. Correia, Development of gold-core silica shell nanospheres coated with poly-2-ethyl-oxazoline and beta-cyclodextrin aimed for cancer therapy, Mater. Sci. Eng. C Mater. Biol. Appl. 98 (2019) 960–968.
[63] X. Huang, W. Qian, I.H. El-Sayed, M.A. El-Sayed, The potential use of the enhanced nonlinear properties of gold nanospheres in photothermal cancer therapy, Lasers in Surg. Med.: Off. J. Am. Soc. Laser Med. Surg. 39 (9) (2007) 747–753.
[64] P. Liu, W. Yang, L. Shi, H. Zhang, Y. Xu, P. Wang, G. Zhang, W.R. Chen, B. Zhang, X. Wang, Concurrent photothermal therapy and photodynamic therapy for cutaneous squamous cell carcinoma by gold nanoclusters under a single NIR laser irradiation, J. Mater. Chem. B 7 (44) (2019) 6924–6933.
[65] J.C.Y. Kah, R.C.Y. Wan, K.Y. Wong, S. Mhaisalkar, C.J.R. Sheppard, M. Olivo, Combinatorial treatment of photothermal therapy using gold nanoshells with conventional photodynamic therapy to improve treatment efficacy: an in vitro study, Lasers Surg. Med.: Off. J. Am. Soc. Laser Med. Surg. 40 (8) (2008) 584–589.
[66] P.K. Jain, M.A. El-Sayed, Universal scaling of plasmon coupling in metal nanostructures: extension from particle pairs to nanoshells, Nano Lett. 7 (9) (2007) 2854–2858.
[67] B.M. Reinhard, M. Siu, H. Agarwal, A.P. Alivisatos, J. Liphardt, Calibration of dynamic molecular rulers based on plasmon coupling between gold nanoparticles, Nano Lett. 5 (11) (2005) 2246–2252.
[68] R. Tannenbaum, M. Zubris, E.P. Goldberg, S. Reich, N. Dan, Polymer-directed nanocluster synthesis: control of particle size and morphology, Macromolecules 38 (10) (2005) 4254–4259.
[69] A.L. West, M.H. Griep, D.P. Cole, S.P. Karna, DNase 1 retains endodeoxyribonuclease activity following gold nanocluster synthesis, Anal. Chem. 86 (15) (2014) 7377–7382.
[70] X. Qu, Y. Li, L. Li, Y. Wang, J. Liang, J. Liang, Fluorescent gold nanoclusters: synthesis and recent biological application, J, Nanomater 2015 (2015).
[71] V. Chegel, O. Rachkov, A. Lopatynskyi, S. Ishihara, I. Yanchuk, Y. Nemoto, J.P. Hill, K. Ariga, Gold nanoparticles aggregation: drastic effect of cooperative functionalities in a single molecular conjugate, J. Phys. Chem. C 116 (4) (2012) 2683–2690.
[72] S. Park, H. Kim, S.C. Lim, K. Lim, E.S. Lee, K.T. Oh, H.-G. Choi, Y.S. Youn, Gold nanocluster-loaded hybrid albumin nanoparticles with fluorescence-based optical visualization and photothermal conversion for tumor detection/ablation, J. Controlled Release 304 (2019) 7–18.
[73] C. Iodice, A. Cervadoro, A. Palange, J. Key, S. Aryal, M.R. Ramirez, C. Mattu, G. Ciardelli, B.E. O'Neill, P. Decuzzi, Enhancing photothermal cancer therapy by clustering gold nanoparticles into spherical polymeric nanoconstructs, Opt. Lasers Eng. 76 (2016) 74–81.
[74] H. Li, P. Wang, Y. Deng, M. Zeng, Y. Tang, W.-H. Zhu, Y. Cheng, Combination of active targeting, enzyme-triggered release and fluorescent dye into gold nanoclusters for endomicroscopy-guided photothermal/photodynamic therapy to pancreatic ductal adenocarcinoma, Biomaterials 139 (2017) 30–38.
[75] C. Loo, A. Lin, L. Hirsch, M.-H. Lee, J. Barton, N. Halas, J. West, R. Drezek, Nanoshell-enabled photonics-based imaging and therapy of cancer, Technol. Cancer Res. T. 3 (1) (2004) 33–40.
[76] Y. Gao, Y. Li, Y. Wang, Y. Chen, J. Gu, W. Zhao, J. Ding, J. Shi, Controlled synthesis of multilayered gold nanoshells for enhanced photothermal therapy and SERS detection, Small 11 (1) (2015) 77–83.
[77] L. Luo, Y. Bian, Y. Liu, X. Zhang, M. Wang, S. Xing, L. Li, D. Gao, Combined near infrared photothermal therapy and chemotherapy using gold nanoshells coated liposomes to enhance antitumor effect, Small 12 (30) (2016) 4103–4112.
[78] A.R. Rastinehad, H. Anastos, E. Wajswol, J.S. Winoker, J.P. Sfakianos, S.K. Doppalapudi, M.R. Carrick, C.J. Knauer, B. Taouli, S.C. Lewis, Gold nanoshell-localized photothermal ablation of prostate tumors in a clinical pilot device study, Proc. Natl. Acad. Sci. 116 (37) (2019) 18590–18596.
[79] Y. Liu, M. Xu, Q. Chen, G. Guan, W. Hu, X. Zhao, M. Qiao, H. Hu, Y. Liang, H. Zhu, Gold nanorods/mesoporous silica-based nanocomposite as theranostic agents for targeting near-infrared imaging and photothermal therapy induced with laser, Int. J. Nanomed. 10 (2015) 4747.
[80] J. Pérez-Juste, L.M. Liz-Marzán, S. Carnie, D.Y. Chan, P. Mulvaney, Electric–field-directed growth of gold nanorods in aqueous surfactant solutions, Adv. Funct. Mater. 14 (6) (2004) 571–579.
[81] D.K. Smith, B.A. Korgel, The importance of the CTAB surfactant on the colloidal seed-mediated synthesis of gold nanorods, Langmuir 24 (3) (2008) 644–649.
[82] P. Huang, L. Bao, C. Zhang, J. Lin, T. Luo, D. Yang, M. He, Z. Li, G. Gao, B. Gao, Folic acid-conjugated silica-modified gold nanorods for X-ray/CT imaging-guided dual-mode radiation and photo-thermal therapy, Biomaterials 32 (36) (2011) 9796–9809.
[83] M.A. Mackey, M.R. Ali, L.A. Austin, R.D. Near, M.A. El-Sayed, The most effective gold nanorod size for plasmonic photothermal therapy: theory and in vitro experiments, J. Phys. Chem. B 118 (5) (2014) 1319–1326.
[84] S. Wang, W. Xi, F. Cai, X. Zhao, Z. Xu, J. Qian, S. He, Three-photon luminescence of gold nanorods and its applications for high contrast tissue and deep in vivo brain imaging, Theranostics 5 (3) (2015) 251.
[85] L.M. Maestro, E. Camarillo, J.A. Sánchez-Gil, R. Rodríguez-Oliveros, J. Ramiro-Bargueño, A. Caamaño, F. Jaque, J.G. Solé, D. Jaque, Gold nanorods for optimized photothermal therapy: the influence of irradiating in the first and second biological windows, RSC Adv. 4 (96) (2014) 54122–54129.
[86] W. Xu, J. Qian, G. Hou, Y. Wang, J. Wang, T. Sun, L. Ji, A. Suo, Y. Yao, A dual-targeted hyaluronic acid-gold nanorod platform with triple-stimuli responsiveness for photodynamic/photothermal therapy of breast cancer, Acta Biomater. 83 (2019) 400–413.
[87] X. Xia, Y. Xia, Gold nanocages as multifunctional materials for nanomedicine, Front. Phys. 9 (3) (2014) 378–384.
[88] S.E. Skrabalak, J. Chen, Y. Sun, X. Lu, L. Au, C.M. Cobley, Y. Xia, Gold nanocages: synthesis, properties, and applications, Acc. Chem. Res. 41 (12) (2008) 1587–1595.
[89] C.M. Cobley, L. Au, J. Chen, Y. Xia, Targeting gold nanocages to cancer cells for photothermal destruction and drug delivery, Expert. Opin. Drug. Deliv. 7 (5) (2010) 577–587.
[90] E. Panfilova, A. Shirokov, B. Khlebtsov, L. Matora, N. Khlebtsov, Multiplexed dot immunoassay using Ag nanocubes, Au/Ag alloy nanoparticles, and Au/Ag nanocages, Nano Res. 5 (2) (2012) 124–134.
[91] J. Yang, D. Shen, L. Zhou, W. Li, X. Li, C. Yao, R. Wang, A.M. El-Toni, F. Zhang, D. Zhao, Spatially confined fabrication of core–shell gold nanocages@ mesoporous silica for near-infrared controlled photothermal drug release, Chem. Mater. 25 (15) (2013) 3030–3037.
[92] H. Cheng, D. Huo, C. Zhu, S. Shen, W. Wang, H. Li, Z. Zhu, Y. Xia, Combination cancer treatment through photothermally controlled release of selenous acid from gold nanocages, Biomaterials 178 (2018) 517–526.
[93] H. Yuan, C.G. Khoury, H. Hwang, C.M. Wilson, G.A. Grant, T. Vo-Dinh, Gold nanostars: surfactant-free synthesis, 3D modelling, and two-photon photoluminescence imaging, Nanotechnology 23 (7) (2012) 075102.
[94] A. Guerrero-Martínez, S. Barbosa, I. Pastoriza-Santos, L.M. Liz-Marzán, Nanostars shine bright for you: colloidal synthesis, properties and applications of branched metallic nanoparticles, Curr. Opin. Colloid Interface Sci. 16 (2) (2011) 118–127.
[95] C.G. Khoury, T. Vo-Dinh, Gold nanostars for surface-enhanced Raman scattering: synthesis, characterization and optimization, J. Phys. Chem. C 112 (48) (2008) 18849–18859.
[96] A. Espinosa, A.K. Silva, A. Sánchez-Iglesias, M. Grzelczak, C. Péchoux, K. Desboeufs, L.M. Liz-Marzán, C. Wilhelm, Cancer cell internalization of gold nanostars impacts their photothermal efficiency in vitro and in vivo: toward a plasmonic thermal fingerprint in tumoral environment, Adv. Healthc. Mater. 5 (9) (2016) 1040–1048.
[97] D. Li, Y. Zhang, S. Wen, Y. Song, Y. Tang, X. Zhu, M. Shen, S. Mignani, J.-P. Majoral, Q. Zhao, Construction of polydopamine-coated gold nanostars for CT imaging and enhanced photothermal therapy of tumors: an innovative theranostic strategy, J. Mater. Chem. B 4 (23) (2016) 4216–4226.
[98] S. Wang, P. Huang, L. Nie, R. Xing, D. Liu, Z. Wang, J. Lin, S. Chen, G. Niu, G. Lu, Single continuous wave laser induced photodynamic/plasmonic photothermal therapy using photosensitizer-functionalized gold nanostars, Adv. Mater. 25 (22) (2013) 3055–3061.
[99] S. Nouri, E. Mohammadi, B. Mehravi, F. Majidi, K. Ashtari, A. Neshasteh-Riz, S. Einali, NIR triggered glycosylated gold nanoshell as a photothermal agent on melanoma cancer cells, Artif. Cells, Nanomed., Biotechnol. 47 (1) (2019) 2316–2324.
[100] L.L. Tan, L. Shang, Smart delivery systems based on Poly (glycidyl methacrylate) s-Coated Organic/Inorganic Core–Shell Nanohybrids, Macromol. Rapid. Commun. 40 (17) (2019) 1800879.
[101] J.-T. Song, X.-Q. Yang, X.-S. Zhang, D.-M. Yan, Z.-Y. Wang, Y.-D. Zhao, Facile synthesis of gold nanospheres modified by positively charged mesoporous silica, loaded with near-infrared fluorescent dye, for in vivo X-ray computed tomography and fluorescence dual mode imaging, ACS Appl. Mater. Interfaces 7 (31) (2015) 17287–17297.
[102] T. Salminen, M. Honkanen, T. Niemi, Coating of gold nanoparticles made by pulsed laser ablation in liquids with silica shells by simultaneous chemical synthesis, Phys. Chem. Chem. Phys. 15 (9) (2013) 3047–3051.
[103] A.F. Moreira, C.F. Rodrigues, C.A. Reis, E.C. Costa, P. Ferreira, I.J. Correia, Development of poly-2-ethyl-2-oxazoline coated gold-core silica shell nanorods for cancer chemo-photothermal therapy, Nanomedicine 13 (20) (2018) 2611–2627.
[104] C. Fernández-López, C. Mateo-Mateo, R.A. Alvarez-Puebla, J. Pérez-Juste, I. Pastoriza-Santos, L.M. Liz-Marzán, Highly controlled silica coating of PEG–capped metal nanoparticles and preparation of SERS-encoded particles, Langmuir 25 (24) (2009) 13894–13899.
[105] B. Zhang, L. Wei, Z. Chu, Development of indocyanine green loaded Au@ Sil-

ica core shell nanoparticles for plasmonic enhanced light triggered therapy, J. Photochem. Photobiol. A 375 (2019) 244–251.
[106] B.N. Khlebtsov, V.A. Khanadeev, E.V. Panfilova, O.A. Inozemtseva, A.M. Burov, N.G. Khlebtsov, A simple Mie-type model for silica-coated gold nanocages, J. Quant. Spectrosc. Radiat. Transf. 121 (2013) 23–29.
[107] Y.-S. Chen, W. Frey, S. Kim, K. Homan, P. Kruizinga, K. Sokolov, S. Emelianov, Enhanced thermal stability of silica-coated gold nanorods for photoacoustic imaging and image-guided therapy, Opt. Express 18 (9) (2010) 8867–8878.
[108] N. Fernandes, C.F. Rodrigues, A.F. Moreira, I.J. Correia, Overview of the application of inorganic nanomaterials in cancer photothermal therapy, Biomater. Sci. (2020).
[109] D. de Melo-Diogo, R. Lima-Sousa, C.G. Alves, I.J. Correia, Graphene family nanomaterials for application in cancer combination photothermal therapy, Biomater. Sci. 7 (9) (2019) 3534–3551.
[110] C. Xu, D. Yang, L. Mei, Q. Li, H. Zhu, T. Wang, Targeting chemophotothermal therapy of hepatoma by gold nanorods/graphene oxide core/shell nanocomposites, ACS Appl. Mater. Interfaces 5 (24) (2013) 12911–12920.
[111] K. Turcheniuk, T. Dumych, R. Bilyy, V. Turcheniuk, J. Bouckaert, V. Vovk, V. Chopyak, V. Zaitsev, P. Mariot, N. Prevarskaya, Plasmonic photothermal cancer therapy with gold nanorods/reduced graphene oxide core/shell nanocomposites, RSC Adv. 6 (2) (2016) 1600–1610.
[112] C. Wu, D. Li, L. Wang, X. Guan, Y. Tian, H. Yang, S. Li, Y. Liu, Single wavelength light-mediated, synergistic bimodal cancer photoablation and amplified photothermal performance by graphene/gold nanostar/photosensitizer theranostics, Acta Biomater. 53 (2017) 631–642.
[113] N. Guskos, J. Typek, M. Maryniak, Z. Roslaniec, D. Petridis, E. Senderek, FMR study of γ–Fe2O3 magnetic nanoparticles embedded in a poly (ether–ester) multiblock copolymers (PEN–block–PTMO) and (PTT–block–PTMO), Rev. Adv. Mater. Sci. 14 (2007) 157–162.
[114] B. Liu, C. Li, G. Chen, B. Liu, X. Deng, Y. Wei, J. Xia, B. Xing, P.a. Ma, J. Lin, Synthesis and optimization of MoS2@ Fe3O4-ICG/Pt (IV) nanoflowers for MR/IR/PA bioimaging and combined PTT/PDT/chemotherapy triggered by 808 nm laser, Adv. Sci. 4 (8) (2017) 1600540.
[115] T. Zhang, Y. Li, W. Hong, Z. Chen, P. Peng, S. Yuan, J. Qu, M. Xiao, L. Xu, Glucose oxidase and polydopamine functionalized iron oxide nanoparticles: combination of the photothermal effect and reactive oxygen species generation for dual-modality selective cancer therapy, J. Mater. Chem. B 7 (13) (2019) 2190–2200.
[116] J. Estelrich, M.A. Busquets, Iron oxide nanoparticles in photothermal therapy, Molecules 23 (7) (2018) 1567.
[117] L.-Y. Bai, X.-Q. Yang, J. An, L. Zhang, K. Zhao, M.-Y. Qin, B.-Y. Fang, C. Li, Y. Xuan, X.-S. Zhang, Multifunctional magnetic-hollow gold nanospheres for bimodal cancer cell imaging and photothermal therapy, Nanotechnology 26 (31) (2015) 315701.
[118] C. Liang, X. Song, Q. Chen, T. Liu, G. Song, R. Peng, Z. Liu, Magnetic field--enhanced photothermal ablation of tumor sentinel lymph nodes to inhibit cancer metastasis, Small 11 (37) (2015) 4856–4863.
[119] J. Nam, S. Son, L.J. Ochyl, R. Kuai, A. Schwendeman, J.J. Moon, Chemo-photothermal therapy combination elicits anti-tumor immunity against advanced metastatic cancer, Nat. Commun. 9 (1) (2018) 1–13.
[120] J. Hu, J. Wang, W. Tang, W. Yang, Y. Liu, R. Li, H. Liu, PEGylated polypyrrole—gold nanocomplex as enhanced photothermal agents against tumor cells, J. Mater. Sci. 55 (13) (2020) 5587–5599.
[121] C. Leng, X. Zhang, F. Xu, Y. Yuan, H. Pei, Z. Sun, L. Li, Z. Bao, Engineering gold nanorod–copper sulfide heterostructures with enhanced photothermal conversion efficiency and photostability, Small 14 (12) (2018) 1703077.
[122] S.K. Maji, S. Yu, K. Chung, M. Sekkarapatti Ramasamy, J.W. Lim, J. Wang, H. Lee, D.H. Kim, Synergistic nanozymetic activity of hybrid gold bipyramid–molybdenum disulfide core@ shell nanostructures for two-photon imaging and anticancer therapy, ACS Appl. Mater. Interfaces 10 (49) (2018) 42068–42076.
[123] J.S. Treger, M.F. Priest, R. Iezzi, F. Bezanilla, Real-time imaging of electrical signals with an infrared FDA-approved dye, Biophys. J. 107 (6) (2014) L09–L12.
[124] I. Ocsoy, N. Isiklan, S. Cansiz, N. Özdemir, W. Tan, ICG-Conjugated magnetic graphene oxide for dual photothermal and photodynamic therapy, RSC Adv. 6 (36) (2016) 30285–30292.
[125] T.I. Kim, K.H. Jeong, M.K. Shin, Verrucous epidermal nevus (VEN) successfully treated with indocyanine green (ICG) photodynamic therapy (PDT), JAAD case reports 1 (5) (2015) 312.
[126] E. Higbee-Dempsey, A. Amirshaghaghi, M.J. Case, J. Miller, T.M. Busch, A. Tsourkas, Indocyanine green–coated gold nanoclusters for photoacoustic imaging and photothermal therapy, Adv. Ther. 2 (9) (2019) 1900088.
[127] J. Chen, Z. Sheng, P. Li, M. Wu, N. Zhang, X.-F. Yu, Y. Wang, D. Hu, H. Zheng, G.P. Wang, Indocyanine green-loaded gold nanostars for sensitive SERS imaging and subcellular monitoring of photothermal therapy, Nanoscale 9 (33) (2017) 11888–11901.
[128] M.M. Leitão, D. de Melo-Diogo, C.G. Alves, R. Lima-Sousa, I.J. Correia, Prototypic heptamethine cyanine incorporating nanomaterials for cancer phototheragnostic, Adv. Healthc. Mater. 9 (6) (2020) 1901665.
[129] C.G. Alves, R. Lima-Sousa, D. de Melo-Diogo, R.O. Louro, I.J. Correia, IR780 based nanomaterials for cancer imaging and photothermal, photodynamic and combinatorial therapies, Int J Pharm 542 (1-2) (2018) 164–175.
[130] T. Nagy-Simon, M. Potara, A.-M. Craciun, E. Licarete, S. Astilean, IR780-dye loaded gold nanoparticles as new near infrared activatable nanotheranostic agents for simultaneous photodynamic and photothermal therapy and intracellular tracking by surface enhanced resonant Raman scattering imaging, J. Colloid Interface Sci. 517 (2018) 239–250.
[131] F. Xia, J. Niu, Y. Hong, C. Li, W. Cao, L. Wang, W. Hou, Y. Liu, D. Cui, Matrix metallopeptidase 2 targeted delivery of gold nanostars decorated with IR-780 iodide for dual-modal imaging and enhanced photothermal/photodynamic therapy, Acta Biomater. 89 (2019) 289–299.
[132] N. Khlebtsov, L. Dykman, Biodistribution and toxicity of engineered gold nanoparticles: a review of in vitro and in vivo studies, Chem. Soc. Rev. 40 (3) (2011) 1647–1671.
[133] R. Arvizo, R. Bhattacharya, P. Mukherjee, Gold nanoparticles: opportunities and challenges in nanomedicine, Expert. Opin. Drug. Deliv. 7 (6) (2010) 753–763.
[134] Y.-P. Jia, B.-Y. Ma, X.-W. Wei, Z.-Y. Qian, The in vitro and in vivo toxicity of gold nanoparticles, Chin. Chem. Lett. 28 (4) (2017) 691–702.
[135] I. Fratoddi, I. Venditti, C. Cametti, M.V. Russo, How toxic are gold nanoparticles? The state-of-the-art, Nano Res. 8 (6) (2015) 1771–1799.
[136] W. Cheng, S. Dong, E. Wang, Synthesis and self-assembly of cetyltrimethylammonium bromide-capped gold nanoparticles, Langmuir 19 (22) (2003) 9434–9439.
[137] T. Niidome, M. Yamagata, Y. Okamoto, Y. Akiyama, H. Takahashi, T. Kawano, Y. Katayama, Y. Niidome, PEG-modified gold nanorods with a stealth character for in vivo applications, J. Control. Release 114 (3) (2006) 343–347.
[138] D.S. Salem, M.A. Sliem, M. El-Sesy, S.A. Shouman, Y. Badr, Improved chemo-photothermal therapy of hepatocellular carcinoma using chitosan–coated gold nanoparticles, J. Photochem. Photobiol. B, Biol. 182 (2018) 92–99.
[139] K. Bolaños, M.J. Kogan, E. Araya, Capping gold nanoparticles with albumin to improve their biomedical properties, Int. J. Nanomed. 14 (2019) 6387.
[140] B. Cheng, H. He, T. Huang, S.S. Berr, J. He, D. Fan, J. Zhang, P. Xu, Gold nanosphere gated mesoporous silica nanoparticle responsive to near-infrared light and redox potential as a theranostic platform for cancer therapy, J. Biomed. Nanotechnol. 12 (3) (2016) 435–449.
[141] P. Manivasagan, S.W. Jun, G. Hoang, S. Mondal, H. Kim, V.H.M. Doan, J. Kim, C.-S. Kim, J. Oh, Anti-EGFR antibody conjugated thiol chitosan-layered gold nanoshells for dual-modal imaging-guided cancer combination therapy, J. Control. Release 311 (2019) 26–42.
[142] X.-D. Zhang, D. Wu, X. Shen, P.-X. Liu, F.-Y. Fan, S.-J. Fan, In vivo renal clearance, biodistribution, toxicity of gold nanoclusters, Biomaterials 33 (18) (2012) 4628–4638.
[143] Y. Chen, Z. Xu, D. Zhu, X. Tao, Y. Gao, H. Zhu, Z. Mao, J. Ling, Gold nanoparticles coated with polysarcosine brushes to enhance their colloidal stability and circulation time in vivo, J. Colloid Interface Sci. 483 (2016) 201–210.
[144] A. Kodiyan, E.A. Silva, J. Kim, M. Aizenberg, D.J. Mooney, Surface modification with alginate-derived polymers for stable, protein-repellent, long-circulating gold nanoparticles, ACS nano 6 (6) (2012) 4796–4805.
[145] C. Xu, F. Chen, H.F. Valdovinos, D. Jiang, S. Goel, B. Yu, H. Sun, T.E. Barnhart, J.J. Moon, W. Cai, Bacteria-like mesoporous silica-coated gold nanorods for positron emission tomography and photoacoustic imaging-guided chemo-photothermal combined therapy, Biomaterials 165 (2018) 56–65.
[146] H. Xie, Z.J. Wang, A. Bao, B. Goins, W.T. Phillips, In vivo PET imaging and biodistribution of radiolabeled gold nanoshells in rats with tumor xenografts, Int. J. Pharm. 395 (1-2) (2010) 324–330.
[147] P. Zhao, S. Liu, L. Wang, G. Liu, Y. Cheng, M. Lin, K. Sui, H. Zhang, Alginate mediated functional aggregation of gold nanoclusters for systemic photothermal therapy and efficient renal clearance, Carbohydr. Polym. (2020) 116344.
[148] H.S. Han, K.Y. Choi, H. Lee, M. Lee, J.Y. An, S. Shin, S. Kwon, D.S. Lee, J.H. Park, Gold-nanoclustered hyaluronan nano-assemblies for photothermally maneuvered photodynamic tumor ablation, ACS Nano 10 (12) (2016) 10858–10868.
[149] S. Zhu, X. Wang, L. Liu, L. Li, Gold nanocluster grafted conjugated polymer nanoparticles for cancer cell imaging and photothermal killing, Colloids Surf., A (2020) 124764.
[150] Z. Wang, S. Li, M. Zhang, Y. Ma, Y. Liu, W. Gao, J. Zhang, Y. Gu, Laser-triggered small interfering rna releasing gold nanoshells against heat shock protein for sensitized photothermal therapy, Adv. Sci 4 (2) (2017) 1600327.
[151] M.H.A. Wahid, N.D. Samsuri, W.M. Mukhtar, A.R. Abdul Rashid, K. Ahmad Dasuki, A.A.R.H. Awangku Yussuf, Synthesis methods of gold nanoparticles for Localized Surface Plasmon Resonance (LSPR) sensor applications, EPJ Web Conf. 162 (2017) 01002.
[152] S.Y. Lee, C.L. Peng, M.J. Shieh, Combined chemo-photothermotherapy using gold nanoshells on drug-loaded micellar templates for colorectal cancer treatment, Part. Part. Syst. Char. 35 (12) (2018) 1800334.
[153] L. Wang, Y. Yuan, S. Lin, J. Huang, J. Dai, Q. Jiang, D. Cheng, X. Shuai, Photothermo-chemotherapy of cancer employing drug leakage-free gold nanoshells, Biomaterials 78 (2016) 40–49.
[154] X. Liu, N. Huang, H. Li, H. Wang, Q. Jin, J. Ji, Multidentate polyethylene glycol modified gold nanorods for in vivo near-infrared photothermal cancer therapy, ACS Appl. Mater. Interfaces 6 (8) (2014) 5657–5668.
[155] X. Wang, S. Gao, Z. Qin, R. Tian, G. Wang, X. Zhang, L. Zhu, X. Chen, Evans blue derivative-functionalized gold nanorods for photothermal therapy-enhanced tumor chemotherapy, ACS Appl. Mater. Interfaces 10 (17) (2018) 15140–15149.
[156] H. Zhu, Y. Chen, F.-J. Yan, J. Chen, X.-F. Tao, J. Ling, B. Yang, Q.-J. He, Z.-W. Mao, Polysarcosine brush stabilized gold nanorods for in vivo near-infrared photothermal tumor therapy, Acta Biomater 50 (2017) 534–545.
[157] J. Song, X. Yang, O. Jacobson, P. Huang, X. Sun, L. Lin, X. Yan, G. Niu, Q. Ma, X. Chen, Ultrasmall gold nanorod vesicles with enhanced tumor accumula-

Please cite this article as: A.S.C. Gonçalves, C.F. Rodrigues and A.F. Moreira et al., Strategies to improve the photothermal capacity of gold-based nanomedicines, Acta Biomaterialia, https://doi.org/10.1016/j.actbio.2020.09.008

tion and fast excretion from the body for cancer therapy, Adv. Mater. 27 (33) (2015) 4910–4917.
[158] X. Liu, Y. Wan, T. Jiang, Y. Zhang, P. Huang, L. Tang, Plasmon-activated nanozymes with enhanced catalytic activity by near-infrared light irradiation, Chem. Commun. 56 (12) (2020) 1784–1787.
[159] Z. Li, P. Huang, X. Zhang, J. Lin, S. Yang, B. Liu, F. Gao, P. Xi, Q. Ren, D. Cui, RGD-conjugated dendrimer-modified gold nanorods for in vivo tumor targeting and photothermal therapy, Mol. Pharm. 7 (1) (2010) 94–104.
[160] Z. Wang, Z. Chen, Z. Liu, P. Shi, K. Dong, E. Ju, J. Ren, X. Qu, A multi-stimuli responsive gold nanocage–hyaluronic platform for targeted photothermal and chemotherapy, Biomaterials 35 (36) (2014) 9678–9688.
[161] Y. Feng, Y. Cheng, Y. Chang, H. Jian, R. Zheng, X. Wu, K. Xu, L. Wang, X. Ma, X. Li, Time-staggered delivery of erlotinib and doxorubicin by gold nanocages with two smart polymers for reprogrammable release and synergistic with photothermal therapy, Biomaterials 217 (2019) 119327.
[162] X. Xu, Y. Chong, X. Liu, H. Fu, C. Yu, J. Huang, Z. Zhang, Multifunctional nanotheranostic gold nanocages for photoacoustic imaging guided radio/photodynamic/photothermal synergistic therapy, Acta Biomater. 84 (2019) 328–338.
[163] S. Huang, S. Duan, J. Wang, S. Bao, X. Qiu, C. Li, Y. Liu, L. Yan, Z. Zhang, Y. Hu, Folic-acid-mediated functionalized gold nanocages for targeted delivery of Anti-miR-181b in combination of gene therapy and photothermal therapy against hepatocellular carcinoma, Adv. Funct. Mater. 26 (15) (2016) 2532–2544.
[164] H. Sun, J. Su, Q. Meng, Q. Yin, L. Chen, W. Gu, Z. Zhang, H. Yu, P. Zhang, S. Wang, Cancer cell membrane-coated gold nanocages with hyperthermia-triggered drug release and homotypic target inhibit growth and metastasis of breast cancer, Adv. Funct. Mater. 27 (3) (2017) 1604300.
[165] D.-M. Zhu, W. Xie, Y.-S. Xiao, M. Suo, M.-H. Zan, Q.-Q. Liao, X.-J. Hu, L.-B. Chen, B. Chen, W.-T. Wu, Erythrocyte membrane-coated gold nanocages for targeted photothermal and chemical cancer therapy, Nanotechnology 29 (8) (2018) 084002.
[166] Y. Tian, S. Luo, H. Yan, Z. Teng, Y. Pan, L. Zeng, J. Wu, Y. Li, Y. Liu, S. Wang, Gold nanostars functionalized with amine-terminated PEG for X-ray/CT imaging and photothermal therapy, J. Mater. Chem. B 3 (21) (2015) 4330–4337.
[167] J. Li, R. Cai, N. Kawazoe, G. Chen, Facile preparation of albumin-stabilized gold nanostars for the targeted photothermal ablation of cancer cells, J. Mater. Chem. B 3 (28) (2015) 5806–5814.
[168] P. Xu, P. Ning, J. Wang, Y. Qin, F. Liang, Y. Cheng, Precise control of apoptosis via gold nanostars for dose dependent photothermal therapy of melanoma, J. Mater. Chem. B 7 (44) (2019) 6934–6944.
[169] S. Shen, H. Tang, X. Zhang, J. Ren, Z. Pang, D. Wang, H. Gao, Y. Qian, X. Jiang, W. Yang, Targeting mesoporous silica-encapsulated gold nanorods for chemo-photothermal therapy with near-infrared radiation, Biomaterials 34 (12) (2013) 3150–3158.
[170] A.S. Monem, N. Elbialy, N. Mohamed, Mesoporous silica coated gold nanorods loaded doxorubicin for combined chemo–photothermal therapy, Int. J. Pharm. 470 (1-2) (2014) 1–7.
[171] J. Liu, C. Detrembleur, M.C. De Pauw-Gillet, S. Mornet, C. Jérôme, E. Duguet, Gold nanorods coated with mesoporous silica shell as drug delivery system for remote near infrared light-activated release and potential phototherapy, Small 11 (19) (2015) 2323–2332.
[172] S. Gao, L. Zhang, G. Wang, K. Yang, M. Chen, R. Tian, Q. Ma, L. Zhu, Hybrid graphene/Au activatable theranostic agent for multimodalities imaging guided enhanced photothermal therapy, Biomaterials 79 (2016) 36–45.
[173] L.-S. Lin, X. Yang, G. Niu, J. Song, H.-H. Yang, X. Chen, Dual-enhanced photothermal conversion properties of reduced graphene oxide-coated gold superparticles for light-triggered acoustic and thermal theranostics, Nanoscale 8 (4) (2016) 2116–2122.
[174] B. Sun, J. Wu, S. Cui, H. Zhu, W. An, Q. Fu, C. Shao, A. Yao, B. Chen, D. Shi, In situ synthesis of graphene oxide/gold nanorods theranostic hybrids for efficient tumor computed tomography imaging and photothermal therapy, Nano Res 10 (1) (2017) 37–48.
[175] F. Wang, Q. Sun, B. Feng, Z. Xu, J. Zhang, J. Xu, L. Lu, H. Yu, M. Wang, Y. Li, Polydopamine-functionalized graphene oxide loaded with gold nanostars and doxorubicin for combined photothermal and chemotherapy of metastatic breast cancer, Adv. Healthc. Mater. 5 (17) (2016) 2227–2236.
[176] Y. Yu, L. Yan, J. Si, Y. Xu, X. Hou, Femtosecond laser assisted synthesis of gold nanorod and graphene hybrids and its photothermal property in the near-infrared region, J. Phys. Chem. Solids 132 (2019) 116–120.
[177] K. Jibin, J.S. Prasad, G. Saranya, S.J. Shenoy, K.K. Maiti, R.S. Jayasree, Optically controlled hybrid metamaterial of plasmonic spiky gold inbuilt graphene sheets for bimodal imaging guided multimodal therapy, Biomater. Sci. (2020).
[178] Z. Qi, J. Shi, Z. Zhang, Y. Cao, J. Li, S. Cao, PEGylated graphene oxide-capped gold nanorods/silica nanoparticles as multifunctional drug delivery platform with enhanced near-infrared responsiveness, Mater. Sci. Eng. C 104 (2019) 109889.
[179] Y. Xuan, R.-Y. Zhang, D.-H. Zhao, X.-S. Zhang, J. An, K. Cheng, X.-L. Hou, X.-L. Song, Y.-D. Zhao, X.-Q. Yang, Ultrafast synthesis of gold nanosphere cluster coated by graphene quantum dot for active targeting PA/CT imaging and near-infrared laser/pH-triggered chemo-photothermal synergistic tumor therapy, Chem. Eng. J. 369 (2019) 87–99.
[180] Y. Yang, Y. Wang, M. Zhu, Y. Chen, Y. Xiao, Y. Shen, A. Xie, RGO/AuNR/HA-5FU nanocomposite with multi-stage release behavior and efficient antitumor activity for synergistic therapy, Biomater. Sci. 5 (5) (2017) 990–1000.
[181] L. Deng, Q. Li, Y. Yang, H. Omar, N. Tang, J. Zhang, Z. Nie, N.M. Khashab, Two-Step" Raman imaging technique to guide chemo-photothermal cancer therapy, Chem.–A Eur. J. 21 (48) (2015) 17274–17281.
[182] Y.K. Kim, H.K. Na, S. Kim, H. Jang, S.J. Chang, D.H. Min, One-pot synthesis of multifunctional Au@ graphene oxide nanocolloid core@ shell nanoparticles for raman bioimaging, photothermal, and photodynamic therapy, Small 11 (21) (2015) 2527–2535.
[183] S. Kang, J. Lee, S. Ryu, Y. Kwon, K.-H. Kim, D.H. Jeong, S.R. Paik, B.-S. Kim, Gold nanoparticle/graphene oxide hybrid sheets attached on mesenchymal stem cells for effective photothermal cancer therapy, Chem. Mater. 29 (8) (2017) 3461–3476.
[184] S.Z. Nergiz, N. Gandra, S. Tadepalli, S. Singamaneni, Multifunctional hybrid nanopatches of graphene oxide and gold nanostars for ultraefficient photothermal cancer therapy, ACS Appl. Mater. Interfaces 6 (18) (2014) 16395–16402.
[185] M.R. Younis, R.B. An, Y.-C. Yin, S. Wang, D. Ye, X.-H. Xia, Plasmonic nanohybrid with high photothermal conversion efficiency for simultaneously effective antibacterial/anticancer photothermal Therapy, ACS Appl. Bio Mater. 2 (9) (2019) 3942–3953.
[186] H. Chen, F. Liu, Z. Lei, L. Ma, Z. Wang, Fe 2 O 3@ Au core@ shell nanoparticle–graphene nanocomposites as theranostic agents for bioimaging and chemo-photothermal synergistic therapy, RSC Adv. 5 (103) (2015) 84980–84987.
[187] D. Yang, G. Yang, P. Yang, R. Lv, S. Gai, C. Li, F. He, J. Lin, Assembly of Au plasmonic photothermal agent and iron oxide nanoparticles on ultrathin black phosphorus for targeted photothermal and photodynamic cancer therapy, Adv. Funct. Mater. 27 (18) (2017) 1700371.
[188] M. Mirrahimi, V. Hosseini, S.K. Kamrava, N. Attaran, J. Beik, S. Kooranifar, H. Ghaznavi, A. Shakeri-Zadeh, Selective heat generation in cancer cells using a combination of 808 nm laser irradiation and the folate-conjugated Fe2O3@ Au nanocomplex, Artif. Cells, Nanomed., Biotechnol. 46 (sup1) (2018) 241–253.
[189] S. Lu, X. Li, J. Zhang, C. Peng, M. Shen, X. Shi, Dendrimer-stabilized gold nanoflowers embedded with ultrasmall iron oxide nanoparticles for multimode imaging–guided combination therapy of tumors, Adv. Sci. 5 (12) (2018) 1801612.
[190] J. Peng, T. Qi, J. Liao, B. Chu, Q. Yang, Y. Qu, W. Li, H. Li, F. Luo, Z. Qian, Mesoporous magnetic gold "nanoclusters" as theranostic carrier for chemo-photothermal co-therapy of breast cancer, Theranostics 4 (7) (2014) 678.
[191] Q. Zhang, L. Zhang, S. Li, X. Chen, M. Zhang, T. Wang, L. Li, C. Wang, Designed synthesis of Au/Fe3O4@ C Janus nanoparticles for dual-modal imaging and actively targeted chemo-photothermal synergistic therapy of cancer cells, Chem.–A Eur. J. 23 (68) (2017) 17242–17248.
[192] G.A. Sotiriou, F. Starsich, A. Dasargyri, M.C. Wurnig, F. Krumeich, A. Boss, J.C. Leroux, S.E. Pratsinis, Photothermal killing of cancer cells by the controlled plasmonic coupling of silica-coated Au/Fe2O3 nanoaggregates, Adv. Funct. Mater. 24 (19) (2014) 2818–2827.
[193] R. Bardhan, W. Chen, C. Perez-Torres, M. Bartels, R.M. Huschka, L.L. Zhao, E. Morosan, R.G. Pautler, A. Joshi, N.J. Halas, Nanoshells with targeted simultaneous enhancement of magnetic and optical imaging and photothermal therapeutic response, Adv. Funct. Mater. 19 (24) (2009) 3901–3909.
[194] Y. Li, X. Wang, D. Yang, P. Hu, L. Gao, D. Chen, Y. Qiao, Y. Wu, X. Jiang, G. Li, Polydopamine-coated gold nanostars for near-infrared cancer photothermal therapy by multiple pathways, J. Mater. Sci. 54 (18) (2019) 12036–12048.
[195] H. Li, Z. Jin, S. Cho, M.J. Jeon, J.-O. Park, S. Park, Folate-receptor-targeted NIR-sensitive polydopamine nanoparticles for chemo-photothermal cancer therapy, Nanotechnology 28 (42) (2017) 425101.
[196] B. Du, X. Gu, W. Zhao, Z. Liu, D. Li, E. Wang, J. Wang, Hybrid of gold nanostar and indocyanine green for targeted imaging-guided diagnosis and phototherapy using low-density laser irradiation, J. Mater. Chem. B 4 (35) (2016) 5842–5849.
[197] W. Cao, X. Wang, L. Song, P. Wang, X. Hou, H. Zhang, X. Tian, X. Liu, Y. Zhang, Folic acid-conjugated gold nanorod@ polypyrrole@ Fe 3 O 4 nanocomposites for targeted MR/CT/PA multimodal imaging and chemo-photothermal therapy, RSC Adv. 9 (33) (2019) 18874–18887.
[198] X. Luo, X. Liu, Y. Pei, Y. Ling, P. Wu, C. Cai, Leakage-free polypyrrole–Au nanostructures for combined Raman detection and photothermal cancer therapy, J. Mater. Chem. B 5 (39) (2017) 7949–7962.
[199] J. Wang, J. Han, C. Zhu, N. Han, J. Xi, L. Fan, R. Guo, Gold nanorods/polypyrrole/m-SiO2 core/shell hybrids as drug nanocarriers for efficient chemo-photothermal therapy, Langmuir 34 (48) (2018) 14661–14669.
[200] H. Zhu, Y. Wang, C. Chen, M. Ma, J. Zeng, S. Li, Y. Xia, M. Gao, Monodisperse dual plasmonic Au@ Cu2–x E (E= S, Se) Core@ shell supraparticles: aqueous fabrication, multimodal imaging, and tumor therapy at in vivo level, ACS nano 11 (8) (2017) 8273–8281.
[201] M.R. Younis, C. Wang, R. An, S. Wang, M.A. Younis, Z.-Q. Li, Y. Wang, A. Ihsan, D. Ye, X.-H. Xia, Low power single laser activated synergistic cancer phototherapy using photosensitizer functionalized dual plasmonic photothermal nanoagents, ACS nano 13 (2) (2019) 2544–2557.
[202] W. Gu, Q. Zhang, T. Zhang, Y. Li, J. Xiang, R. Peng, J. Liu, Hybrid polymeric nano-capsules loaded with gold nanoclusters and indocyanine green for dual-modal imaging and photothermal therapy, J. Mater. Chem. B 4 (5) (2016) 910–919.
[203] X. Jiang, B. Du, Y. Huang, M. Yu, J. Zheng, Cancer photothermal therapy with ICG-conjugated gold nanoclusters, Bioconjugate Chem. 31 (5) (2020) 1522–1528.
[204] Y. Liu, X. Zhi, M. Yang, J. Zhang, L. Lin, X. Zhao, W. Hou, C. Zhang, Q. Zhang,

Please cite this article as: A.S.C. Gonçalves, C.F. Rodrigues and A.F. Moreira et al., Strategies to improve the photothermal capacity of gold-based nanomedicines, Acta Biomaterialia, https://doi.org/10.1016/j.actbio.2020.09.008

F. Pan, Tumor-triggered drug release from calcium carbonate-encapsulated gold nanostars for near-infrared photodynamic/photothermal combination antitumor therapy, Theranostics 7 (6) (2017) 1650.
[205] R. Liu, C. Hu, Y. Yang, J. Zhang, H. Gao, Theranostic nanoparticles with tumor-specific enzyme-triggered size reduction and drug release to perform photothermal therapy for breast cancer treatment, Acta Pharm. Sin. B 9 (2) (2019) 410–420.
[206] Q. You, Q. Sun, M. Yu, J. Wang, S. Wang, L. Liu, Y. Cheng, Y. Wang, Y. Song, F. Tan, BSA–bioinspired gadolinium hybrid-functionalized hollow gold nanoshells for NIRF/PA/CT/MR quadmodal diagnostic imaging-guided photothermal/photodynamic cancer therapy, ACS Appl. Mater. Interfaces 9 (46) (2017) 40017–40030.
[207] J. Liu, H. Liang, M. Li, Z. Luo, J. Zhang, X. Guo, K. Cai, Tumor acidity activating multifunctional nanoplatform for NIR-mediated multiple enhanced photodynamic and photothermal tumor therapy, Biomaterials 157 (2018) 107–124.
[208] H. Cui, D. Hu, J. Zhang, G. Gao, Z. Chen, W. Li, P. Gong, Z. Sheng, L. Cai, Gold nanoclusters–indocyanine green nanoprobes for synchronous cancer imaging, treatment, and real-time monitoring based on fluorescence resonance energy transfer, ACS Appl. Mater. Interfaces 9 (30) (2017) 25114–25127.
[209] X. Huang, Y. Yin, M. Wu, W. Zan, Q. Yang, LyP-1 peptide-functionalized gold nanoprisms for SERRS imaging and tumor growth suppressing by PTT induced-hyperthermia, Chin. Chem. Lett. 30 (6) (2019) 1335–1340.
[210] Y. Huang, Q. Liu, Y. Wang, N. He, R. Zhao, J. Choo, L. Chen, Gold nanorods functionalized by a glutathione response near-infrared fluorescent probe as a promising nanoplatform for fluorescence imaging guided precision therapy, Nanoscale 11 (25) (2019) 12220–12229.
[211] Y. Liu, X. Zhang, L. Luo, L. Li, R.Y. Zhu, A. Li, Y. He, W. Cao, K. Niu, H. Liu, Gold–nanobranched-shell based drug vehicles with ultrahigh photothermal efficiency for chemo-photothermal therapy, Nanomed.-Nanotechnol. 18 (2019) 303–314.
[212] M. Xuan, J. Shao, L. Dai, J. Li, Q. He, Macrophage cell membrane camouflaged Au nanoshells for in vivo prolonged circulation life and enhanced cancer photothermal therapy, ACS Appl. Mater. Interfaces 8 (15) (2016) 9610–9618.
[213] C. Lee, H.S. Hwang, S. Lee, B. Kim, J.O. Kim, K.T. Oh, E.S. Lee, H.G. Choi, Y.S. Youn, Rabies virus-inspired silica-coated gold nanorods as a photothermal therapeutic platform for treating brain tumors, Adv. Mater. 29 (13) (2017) 1605563.
[214] W.I. Choi, J.-Y. Kim, C. Kang, C.C. Byeon, Y.H. Kim, G. Tae, Tumor regression in vivo by photothermal therapy based on gold-nanorod-loaded, functional nanocarriers, ACS nano 5 (3) (2011) 1995–2003.
[215] Z. Li, S. Tang, B. Wang, Y. Li, H. Huang, H. Wang, P. Li, C. Li, P.K. Chu, X.-F. Yu, Metabolizable small gold nanorods: size-dependent cytotoxicity, cell uptake and in vivo biodistribution, ACS Biomater. Sci. Eng. 2 (5) (2016) 789–797.
[216] S. Huang, C. Li, W. Wang, H. Li, Z. Sun, C. Song, B. Li, S. Duan, Y. Hu, A54 peptide-mediated functionalized gold nanocages for targeted delivery of DOX as a combinational photothermal-chemotherapy for liver cancer, Int. J. Nanomed. 12 (2017) 5163.
[217] R. Liang, L. Liu, H. He, Z. Chen, Z. Han, Z. Luo, Z. Wu, M. Zheng, Y. Ma, L. Cai, Oxygen-boosted immunogenic photodynamic therapy with gold nanocages@manganese dioxide to inhibit tumor growth and metastases, Biomaterials 177 (2018) 149–160.
[218] Y. Wang, Y. Liu, H. Luehmann, X. Xia, P. Brown, C. Jarreau, M. Welch, Y. Xia, Evaluating the pharmacokinetics and in vivo cancer targeting capability of Au nanocages by positron emission tomography imaging, ACS nano 6 (7) (2012) 5880–5888.
[219] Q. Xu, J. Wan, N. Bie, X. Song, X. Yang, T. Yong, Y. Zhao, X. Yang, L. Gan, A biomimetic gold nanocages-based nanoplatform for efficient tumor ablation and reduced inflammation, Theranostics 8 (19) (2018) 5362.
[220] J.-G. Piao, F. Gao, Y. Li, L. Yu, D. Liu, Z.-B. Tan, Y. Xiong, L. Yang, Y.-Z. You, pH-sensitive zwitterionic coating of gold nanocages improves tumor targeting and photothermal treatment efficacy, Nano Res 11 (6) (2018) 3193–3204.
[221] Y. Liu, J.R. Ashton, E.J. Moding, H. Yuan, J.K. Register, A.M. Fales, J. Choi, M.J. Whitley, X. Zhao, Y. Qi, A plasmonic gold nanostar theranostic probe for in vivo tumor imaging and photothermal therapy, Theranostics 5 (9) (2015) 946.
[222] X. Huang, W. Shang, H. Deng, Y. Zhou, F. Cao, C. Fang, P. Lai, J. Tian, Clothing spiny nanoprobes against the mononuclear phagocyte system clearance in vivo: Photoacoustic diagnosis and photothermal treatment of early stage liver cancer with erythrocyte membrane-camouflaged gold nanostars, Appl. Mater. Today 18 (2020) 100484.
[223] D.H.M. Dam, K.S. Culver, I. Kandela, R.C. Lee, K. Chandra, H. Lee, C. Mantis, A. Ugolkov, A.P. Mazar, T.W. Odom, Biodistribution and in vivo toxicity of aptamer-loaded gold nanostars, Nanomed.-Nanotechnol. 11 (3) (2015) 671–679.
[224] X. Li, L. Xing, K. Zheng, P. Wei, L. Du, M. Shen, X. Shi, Formation of gold nanostar-coated hollow mesoporous silica for tumor multimodality imaging and photothermal therapy, ACS Appl. Mater. Interfaces 9 (7) (2017) 5817–5827.
[225] G.F. Luo, W.H. Chen, Q. Lei, W.X. Qiu, Y.X. Liu, Y.J. Cheng, X.Z. Zhang, A triple–collaborative strategy for high-performance tumor therapy by multifunctional mesoporous silica-coated gold nanorods, Adv. Funct. Mater. 26 (24) (2016) 4339–4350.
[226] Y. Gao, Y. Li, J. Chen, S. Zhu, X. Liu, L. Zhou, P. Shi, D. Niu, J. Gu, J. Shi, Multifunctional gold nanostar-based nanocomposite: synthesis and application for noninvasive MR-SERS imaging-guided photothermal ablation, Biomaterials 60 (2015) 31–41.
[227] X. Liu, J. Cao, H. Li, J. Li, Q. Jin, K. Ren, J. Ji, Mussel-inspired polydopamine, a biocompatible and ultrastable coating for nanoparticles in vivo, ACS nano 7 (10) (2013) 9384–9395.
[228] C. Cai, X. Li, Y. Wang, M. Liu, X. Shi, J. Xia, M. Shen, Polydopamine-coated gold core/hollow mesoporous silica shell particles as a nanoplatform for multimode imaging and photothermal therapy of tumors, Chem. Eng. J. 362 (2019) 842–850.
[229] Y. Liu, Z. Li, Z. Yin, H. Zhang, Y. Gao, G. Huo, A. Wu, L. Zeng, Amplified photoacoustic signal and enhanced photothermal conversion of polydopamine-coated gold nanobipyramids for phototheranostics and synergistic chemotherapy, ACS Appl. Mater. Interfaces 12 (13) (2020) 14866–14875.

Please cite this article as: A.S.C. Gonçalves, C.F. Rodrigues and A.F. Moreira et al., Strategies to improve the photothermal capacity of gold-based nanomedicines, Acta Biomaterialia, https://doi.org/10.1016/j.actbio.2020.09.008